DISCLAIMER

CASL-U-2017-1424-000

Development of Transient MPACT-CTF Capability for RIA with DNB

Brendan Kochunas

Tom Downar
Yuxuan Liu
Qicang Shen
Zack Dodson
Andrew Gerlach
Dan Jabaay

University of Michigan

Aaron Wysocki

Oak Ridge National Lab

Vefa Kucukboyaci

Westinghouse Electric Corp.

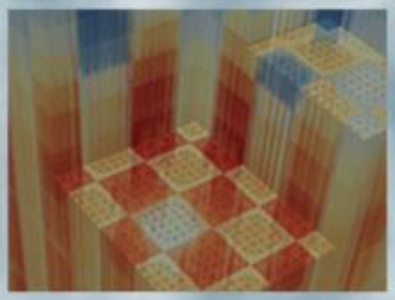

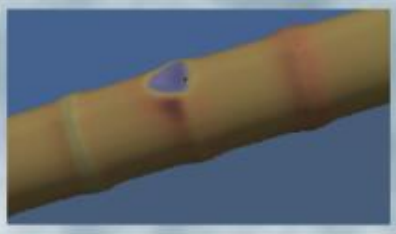

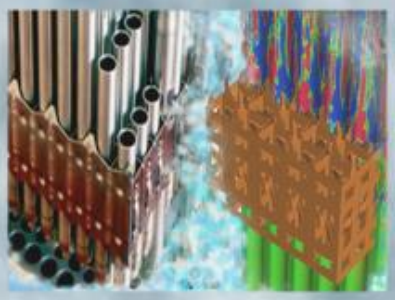

September 29, 2017

REVISION LOG

Revision	Date	Affected Pages	Revision Description
0	9/29/2017	All	Initial Release

Document pages that are:

Export Controlled _____

IP/Proprietary/NDA Controlled_____

Sensitive Controlled_____

Requested Distribution:

To:

Copy:

EXECUTIVE SUMMARY

The objective of this milestone was to continue the development, implementation, verification, and validation of the methods in VERA-CS necessary to solve the whole-core time-dependent neutron transport equations with pin-resolved detail for a practical PWR applications. This capability is necessary to provide the time dependent pin resolved neutron flux for analysis of the Reactivity Insertion Accident (RIA) as specified in the CASL RIA Challenge Problem Implementation Plan, CASL-I-2013-0060-000 [65]. The FY17 work reported here continued the FY16 work reported in CASL-U-2016-1188-000 which was primarily focused on MPACT and performed the methods, and Validation and Verification (V&V) efforts necessary to demonstrate the transient capability in VERA-CS in order to facilitate the L1 RIA milestone in FY18. This report describes the activities performed in FY17 in the three general areas of: User Support, Methods Improvements, and in V&V and Demonstration. In the area of User Support various user requested features were added to the code such as detailed reactivity edits and improvements to the VERA input. In the area of Methods Improvements, the features added included user controlled variable time stepping, a one-group CMFD Acceleration, and a Delayed Energy Deposition model; as well as improvements to the overall code robustness for the transient solution. In the area of V&V, the full suite of C5G7 Transient benchmarks was completed and significant progress was made on the solution of SPERT with VERA-CS. In the area of practical demonstration, a full core AP1000 demonstration problem was performed with VERA-CS. The work performed in FY17 enhanced the capability of performing VERA-CS transients for practical large-scale light water reactor problems with an acceptable computational burden and provided an important step in the completion of the CASL Reactivity Insertion Accident (RIA) Challenge Problem.

CONTENTS

FIGURES

TABLES

ACRONYMS

AMA	Advanced Modeling Applications
ATWS-ED	Anticipated Transient without Scram – Emergency Depressurization
BDM	boron deposition model
BWR	boiling water reactor
CASL	Consortium for Advanced Simulation of Light Water Reactors
CHF	Critical Heat Flux
CILC	CRUD-induced localized corrosion
CIPS	CRUD-induced power shift
CFD	computational fluid dynamics
CP	Challenge Problem
CRUD	corrosion-related unidentified deposits or Chalk River unidentified deposits
CTF	COBRA-TF subchannel thermal-hydraulics code
CZP	Cold Zero Power
DA	data assimilation
DBA	design basis accident
DNB	departure from nucleate boiling
DOE	US Department of Energy
DOE NE	US Department of Energy Office of Nuclear Energy
DOE NR	US Department of Energy Office of Naval Reactors
DTK	Data Transfer Kit
DVE	Digital Video Enterprises
EIH	Energy Innovation Hub
ELT	Extended Leadership Team
EOI	expression of interest
EPRI	Electric Power Research Institute
FA	Focus Area
FAD	fuel assembly distortion
FMC	Fuel Materials and Chemistry
FOA	Funding Opportunity Announcement
FSI	fluid-structure interaction
GTRF	grid-to-rod-fretting
HFP	Hot Full Power
HPC	high-performance computing
HZP	Hot Zero Power
IC	Industry Council
INCITE	innovative and novel computational impact on theory and experiment
INL	Idaho National Laboratory
IP	intellectual property
iPWR	integral PWR
ISV	independent software vendor
LANL	Los Alamos National Laboratory
LOCA	loss of coolant accident
LWR	light water reactor
LWRS	Light Water Reactor Sustainability
M&S	modeling and simulation
MAMBA	MPO advanced model for boron analysis
M-CFD	multiphase computational fluid dynamics
MIT	Massachusetts Institute of Technology
MNM	Models and Numerical Methods
MOC	method of characteristics
MPACT	Michigan parallel characteristics transport code
MPO	Materials Performance and Optimization

NCSU	North Carolina State University
NEAMS	Nuclear Energy Advanced Modeling and Simulation
NE-KAMS	Nuclear Energy – Knowledge base for Advanced Modeling and Simulation
NPP	nuclear power plant
NRC	Nuclear Regulatory Commission
NRR	NRC Office of Nuclear Reactor Regulation
NSSS	nuclear steam supply system
OIG	Office of Inspector General
OLCF	Oak Ridge Leadership Computing Facility
OR	operational reactor
ORNL	Oak Ridge National Laboratory
PCI	pellet-cladding interaction
PCM	percent mille (10-5)
PCMI	pellet-cladding mechanical interaction
PHI	Physics Integration
PoR	plan of record
PWR	pressurized water reactor
QOI	quantity of interest
R&D	research and development
RD&D	research, development, and deployment
RES	NRC Office of Nuclear Regulatory Research
RIA	reactivity insertion accident
SA	sensitivity analysis
SBA	station blackout
S/G	steam generator
SLCS	Standby Liquid Control System
SLT	Senior Leadership Team
SMR	small modular reactor
SNL	Sandia National Laboratories
T/H	thermal-hydraulics
TDO	Technology Deployment and Outreach
TF	1012 floating point operations per second (“teraflop”)
THM	Thermal Hydraulics Methods
TLT	Technical Leadership Team
TVA	Tennessee Valley Authority
TWIGL	A computer code for solving neutron diffusion equations
UQ	uncertainty quantification
UM	University of Michigan
V&V	verification and validation
VERA	Virtual Environment for Reactor Applications
VMA	Validation and Modeling Applications
VOCC	Virtual Office, Community, and Computing
VPSC	Viscoplastic Self-Consistent model
VR	virtual reactor
VRI	Virtual Reactor Integration Focus Area
VUQ	Validation and Uncertainty Quantification
VVUQ	Verification, Validation and Uncertainty Quantification
WEC	Westinghouse Electric Company

1. INTRODUCTION

1.1 Background

The objective of this milestone was to continue the development, implementation, verification, and validation of the methods in VERA-CS necessary to solve the whole-core time-dependent neutron transport equations with pin-resolved detail for a practical PWR applications. This capability is necessary to provide the time dependent pin resolved neutron flux for analysis of the Reactivity Insertion Accident (RIA) as specified in the CASL RIA Challenge Problem Implementation Plan, CASL-I-2013-0060-000 [65]. The FY17 work reported here continued the FY16 work reported in CASL-U-2016-1188-000 which was primarily focused on MPACT and performed the methods, and Validation and Verification (V&V) efforts necessary to demonstrate the transient capability in VERA-CS in order to facilitate the L1 RIA milestone in FY18.

This report describes the activities performed in FY17 in the three general areas of: User Support, Methods Improvements, and in V&V and Demonstration. In the area of User Support various user requested features were added to the code such as detailed reactivity edits and improvements to the VERA input. In the area of Methods Improvements, the features added included user controlled variable time stepping, a one-group CMFD Acceleration, and a Delayed Energy Deposition model; as well as improvements to the overall code robustness for the transient solution. In the area of V&V, the full suite of C5G7 Transient benchmarks was completed and significant progress was made on the solution of SPERT with VERA-CS. In the area of practical demonstration, a full core AP1000 demonstration problem was performed with VERA-CS. The work performed in FY17 enhanced the capability of performing VERA-CS transients for practical large-scale light water reactor problems with an acceptable computational burden and provided an important step in the completion of the CASL Reactivity Insertion Accident (RIA) Challenge Problem.

1.2 Milestone Execution Plan and Completion Criteria

As outlined in the RIA milestone execution plan, the following specific subtasks were proposed for FY17:

1. **User Input and Output Improvements** - The transient VERAIN / VERAOUT should be further improved to minimize the user burden and facilitate the user analysis. For example, several repetitive cards are currently required in the input to move a control bank and some additional transient edits should be be added to VERAOUT.

2. **Adaptive Time Stepping Method** - Currently the time steps for each level of TML method are specified as user input. For example, a 5 ms time step for MOC, 1 ms for CMFD and 0.2 ms for EPKE were used for the Watts Bar Demonstration problems and are reasonable time step settings for LWR super-prompt transient simulations. However, the time steps in each level can vary by the nature of the transient, the initial conditions, and type of reactor (i.e. PWR or BWR). An automatic adaptive time stepping method will be investigated in FY17 which will take advantage of the three sets of solvers in the TML scheme to estimate the time steps.

3. **Improve CMFD Efficiency** - The TML method implemented in this work shifted much of the computational burden from the MOC to the CMFD calculation. This past year several improvements were made to the CMFD steady-state method, however, the transient method has some unique features which were addressed to take full advantage of these improvements.

4. **Control Rod Cusping Treatment** - A new cusping method is being implemented in MPACT and this subtask will be to integrate and test it within the MPACT transient algorithm, and then rerun the V&V and demonstration problems. (Note: The steady-state application of this work was completed as part of the PhD thesis work of A. Graham on the Sub-Plane method and included in a separate L4 milestone report. However, implementation of a control rod cusping treatment in MPACT for the transient solver was deferred until FY18 and is included as a RTM Milestone.)

5. **Testing of CTF for Transient** - The internal transient TH conduction solver implemented in MPACT was adequate for the preliminary validation of MPACT for superprompt critical transients. However, the internal TH in MPACT did not include transient convection and therefore was not adequate for longer transient. The validation and application of MPACT for the full range of transient conditions required the coupling of MPACT to CTF and its validation for transient conditions.

6. **Testing of Coupled MPACT/CTF Coupling Numerics** - MPACT is currently coupled to CTF and has been verified and validated for several steady-state problems. The coupling of MPACT to CTF for transient applications was investigated as part of a L3 milestone in PHI in FY17. This subtask was to continue the testing and perform any modifications for the V&V and Demonstration problems.

7. **Perform validation cases w/ VERA-CS Transient** - The current validation work performed on MPACT transient is preliminary since internal TH is adequate only for a limited range of transient conditions. After CTF transient capability was validated and coupled to MPACT in POR14, work ws begun on validating VERA-CS using an expanded range of SPERT III E-Core validation cases and a a wider range of Watts Bar transient conditions.

As also described in the RIA Milestone, the Completion Criteria for this milestone was:

1. Updated Version of MPACT

2. Milestone report

3. Presentation at a colocation meeting

2. USER SUPPORT ACTIVITIES

The majority of user support activities related to development supporting usability of input and output. Effort put forth to improve stability and robustness may also be considered a user support activity, although in this document, these efforts are documented under the methods improvements. Significant effort went into improving the output and edits for transient, and consequently not everything that could have been done for improving the input was accomplished. However, a detailed plan for improving the input was developed and will be executed in FY18.

For improving the output much of the most basic edits from steady state had to be implemented for the transient case. This included edits like power, time, and core state parameters. In addition to those edits for the kinetics parameters were also developed. The development of the output edits for transient calculations were needed in both MPACT and CTF. Lastly, for MPACT a new calculation capability for the component reactivity edits needed to be developed. This is documented in the next subsection. Section 2.2 describes the plan for improving the input.

2.1 Component Reactivity Edits

2.1.1 Introduction

When analyzing a RIA, the user requires reactivity edits to quantify the contribution of each physical process to the change in reactivity as a function of time. These physical phenomena, including changes in temperature or flux shape, exhibit separate effects on the reactivity of the system. For example, in a control rod ejection scenario, observing the contribution of the fuel temperature change on the reactivity can offer insight into how damage can be prevented or mitigated. Therefore, effort is currently underway to add component reactivity edits to MPACT in addition to the current total reactivity calculation.

MPACT takes advantage of exact perturbation theory to compute the reactivity during a transient solve. This is possible because the scalar flux is computed at each timestep of the transient using MOC. Thus, it is possible to compute the reactivity using the following equation, where ρ is the reactivity, ϕ_0^* is the initial adjoint flux (before the system is perturbed), $\boldsymbol{M}$ is the migration and leakage operator, $\boldsymbol{F}$ is the fission source operator, and ϕ is the scalar flux.

$$\rho = \frac{\langle \phi_0^* (\boldsymbol{M} - \boldsymbol{F}) \phi \rangle}{\langle \phi_0^* \boldsymbol{F} \phi \rangle}$$

These calculations are done on the CMFD mesh within MPACT, which is a much courser mesh compared to the transport mesh. Therefore, the is a homogenization step to update the CMFD mesh to changes to the transport mesh. For each timestep i of the transient solve, ρ_i is calculated after any perturbations for that step are applied to $\boldsymbol{M}_i$. This is the total reactivity relative to the state of the system before the first transient timestep. To compute the component reactivity values for each timestep, the perturbations must be isolated. By applying each perturbation type in sequence and calculating the reactivity after each application, the components can be separated from the total reactivity.

Currently, MPACT only provides an edit for total reactivity of the system. The task of adding component reactivity edits will add outputs for the following reactivity components:

- Flux shape (ρ_ϕ)

- Fuel temperature or Doppler (ρ_{ft})
- Moderator temperature (ρ_{mt})
- Moderator density (ρ_{md})
- Material change (ρ_{mat})
- Control rod movement (ρ_c)

These reactivity components constitute the majority of physical phenomena that occur in a PWR that have an appreciable effect of the reactivity of the system. Therefore, the sum of each of these components is expected to be the calculated total reactivity. The timescale of transients in MPACT are assumed to be on the order of milliseconds to seconds, so effects like burnup are not considered for this task.

When computing component reactivity values, there are two approaches that may be considered. The first is to apply the conditions of each component to the system for each calculation and reset to the initial state for each separate component. This would result in accurate reactivity values for each component relative to the initial state. In this case, the sum of the components may not equal the total reactivity because of possible interference of separate effects. The second approach is cumulative, where each separate component condition is applied in sequence and the component reactivity values are calculated after each application without resetting the system to the initial state for each component. This approach will result in the components summing to the total reactivity. The latter approach was chosen for better consistency and clarity in the results.

2.1.1 Design and Approach

To obtain component reactivity values for each timestep i, the following approach was used. This series of steps is taken for each timestep of a transient calculation. Before the transient solver is evoked, the initial state of the system, including fuel temperatures, moderator temperatures, moderator densities, and materials, are stored in a new feedback operation class called `FeedbackOpType_FixedTH`. These values are stored by contiguous XS region, which is a group of flat source regions with the same material and physical state values such as temperature and density. The memory and computational overhead from storing and later applying these values is proportional to the volume of the problem. All state operators are called from the `FeedbackOpType_FixedTH` class. A new routine called `calcComponentRx` in the transient fixed source solver performs the following steps, including the reactivity calculations.

1. If the system is experiencing a material change perturbation, save the current materials of the system. This operator is represented as $\mathrm{O}_{mat,i}$ and represents the change to $\boldsymbol{M}_i$ caused by the transition from the initial materials to the materials of the current timestep.

2. Reset $\boldsymbol{M}$ to its initial state by applying all initial conditions (represented by the $\mathrm{O}_{init,i}$ operator). $\boldsymbol{M}_i$ is overwritten with these new conditions (as is done for each component).

$$\boldsymbol{M}_i = \mathrm{O}_{init,i}(\boldsymbol{M}_i)$$

   This includes:
   a. Reset moderator and fuel temperatures and moderator density to initial values.
   b. If a material perturbation is done, reset to initial materials and number densities.
   c. If performing a control rod transient, move the control rods to their initial positions.
      i. Recalculate shielded fuel cross sections.

3. Compute the flux shape reactivity:

$$\rho_{\phi,i} = \frac{\langle \phi_0^*(\boldsymbol{M}_i - \boldsymbol{F}_i)\phi_i \rangle}{\langle \phi_0^* \boldsymbol{F}_i \phi_i \rangle}$$

This component evaluates the effect that the flux shape change has on the reactivity of the system relative to the initial state. For example, if the flux shape has changed such that the magnitude has increased in a region where an absorber was present in the initial state (such as a control rod), $\rho_{\phi,i}$ will be negative.

4. Apply the current state of the materials in the problem (represented as the $\mathrm{O}_{mat,i}$ operator). This step is only relevant for cases where the materials are perturbed.

$$\boldsymbol{M}_i = \mathrm{O}_{mat,i}(\boldsymbol{M}_i)$$

If the materials are perturbed, calculate $\rho_{mat,i}$:

$$\rho_{mat,i} = \frac{\langle \phi_0^*(\boldsymbol{M}_i - \boldsymbol{F}_i)\phi_i \rangle}{\langle \phi_0^* \boldsymbol{F}_i \phi_i \rangle} - \rho_{\phi,i}$$

5. Apply the current fuel temperatures (represented as the $\mathrm{O}_{ft,i}$ operator) and update $\boldsymbol{F}_i$ by recalculating shielded fuel cross sections.

$$\boldsymbol{M}_i = \mathrm{O}_{ft,i}(\boldsymbol{M}_i)$$

$$\rho_{ft,i} = \frac{\langle \phi_0^*(\boldsymbol{M}_i - \boldsymbol{F}_i)\phi_i \rangle}{\langle \phi_0^* \boldsymbol{F}_i \phi_i \rangle} - \left(\rho_{\phi,i} + \rho_{mat,i}\right)$$

6. Apply the current moderator temperatures (represented as the $\mathrm{O}_{mt,i}$ operator).

$$\boldsymbol{M}_i = \mathrm{O}_{mt,i}(\boldsymbol{M}_i)$$

$$\rho_{mt,i} = \frac{\langle \phi_0^*(\boldsymbol{M}_i - \boldsymbol{F}_i)\phi_i \rangle}{\langle \phi_0^* \boldsymbol{F}_i \phi_i \rangle} - \left(\rho_{\phi,i} + \rho_{mat,i} + \rho_{ft,i}\right)$$

7. Apply the current moderator densities (represented as the $\mathrm{O}_{md,i}$ operator).

$$\boldsymbol{M}_i = \mathrm{O}_{md,i}(\boldsymbol{M}_i)$$

$$\rho_{md,i} = \frac{\langle \phi_0^*(\boldsymbol{M}_i - \boldsymbol{F}_i)\phi_i \rangle}{\langle \phi_0^* \boldsymbol{F}_i \phi_i \rangle} - \left(\rho_{\phi,i} + \rho_{mat,i} + \rho_{ft,i} + \rho_{mt,i}\right)$$

8. Apply the current control rod positions (represented as the $\mathrm{O}_{c,i}$ operator) and update shielded fuel cross sections.

$$\boldsymbol{M}_i = \mathrm{O}_{c,i}(\boldsymbol{M}_i)$$

$$\rho_{c,i} = \frac{\langle \phi_0^*(\boldsymbol{M}_i - \boldsymbol{F}_i)\phi_i \rangle}{\langle \phi_0^* \boldsymbol{F}_i \phi_i \rangle} - \left(\rho_{\phi,i} + \rho_{mat,i} + \rho_{ft,i} + \rho_{mt,i} + \rho_{c,i}\right)$$

After all steps are completed, the system will be in its true state at timestep i, so no corrective measures are necessary before proceeding with the transient solve. The portion of this process that has the largest computational overhead is recalculating the shielded fuel cross sections. For large problems with many energy groups, this calculation (which is done multiple times for each timestep) can be extremely expensive. Thus, calculating component reactivity values has been made optional. To invoke this feature, the user will set the `rx_components` card in the VERA input to `true` (there is currently no option for the native MPACT input format). Component reactivity values will be printed to the HDF5 output file.

2.1.2 Example of Capability

An example of the capability of component reactivity edits is shown in Figure 1. The test problem is a small core of 9 7x7 assemblies with 3.1wt% UO_2. This problem is somewhat unrealistic, with a control bank ejection from 0 to 0.025 seconds and a rapid boron dilution in the moderator from 0.025 to 0.1 seconds (which is considered a material change). However, it showcases both the control rod and material change reactivity calculation capabilities in a single case. Additionally, changes in the flux shape and Doppler reactivity can be observed.

In this problem, the flux shape and control rod reactivity values are very large (~6$). The large positive reactivity from the control rod ejection is due to removal of absorber in the core, while the cause of the large negative flux shape reactivity is less obvious. Since all reactivity values are reported relative to the initial state of the system, and this problem includes a control rod ejection, the flux shape reactivity is negative because the magnitude of the neutron flux has increased in and around the control rod guide tubes. If this flux shape were in place for the initial state, the negative reactivity effect would be large (due to increased absorption), which is reflected in the figure. The effect of the rising fuel temperature can be seen in the figure as well, as the negative Doppler reactivity. Of course, the dilution of the boron in the moderator (material reactivity) is a positive reactivity effect in this case.

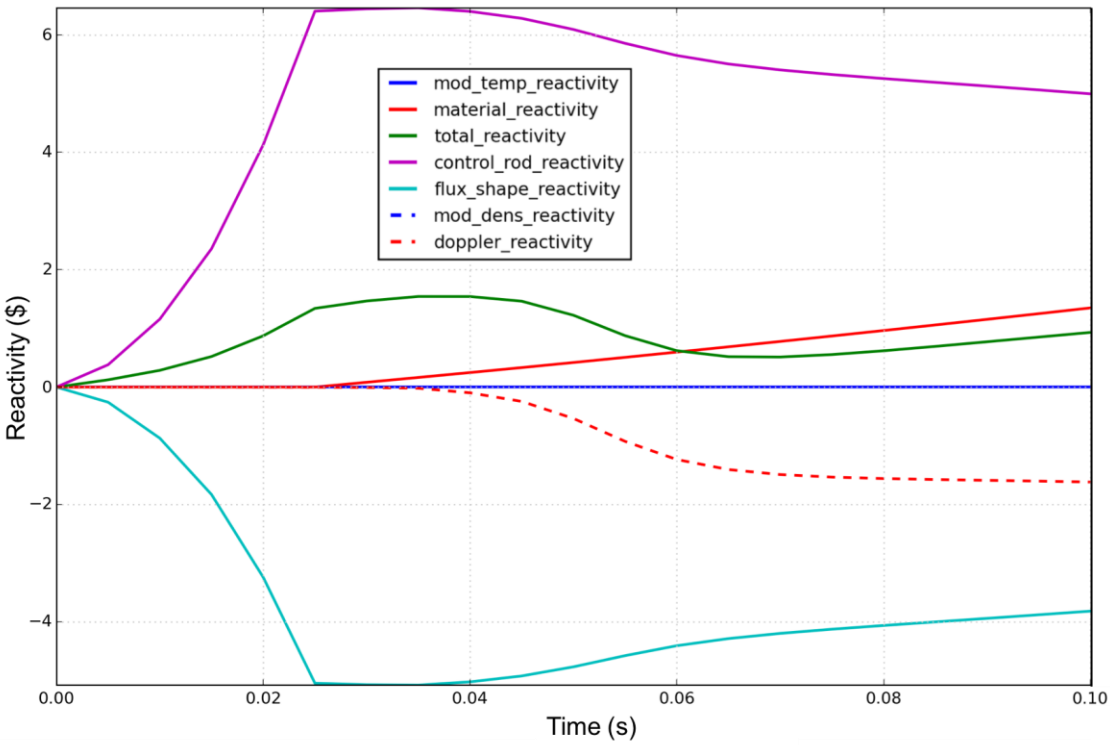

Figure 1.1 Total and component reactivity values for a control bank ejection (0-0.025 s) followed by boron dilution in the moderator (0.025-0.1 s) for a small core.

2.1.3 Future Work

While substantial progress has been made for this task, there is still work to be done. This is primarily composed of testing. Unit and regression tests will be implemented for this feature that will ensure that:

- Calculation of component reactivity values does not affect other output values
- The conditions applied for each component are consistent
- The sum of the component reactivity values is the total reactivity (within a tolerance)
- Component reactivity calculations can be done for different types of cases

Once these tests are completed, this feature will be added to the current version of MPACT. However, the substantial computational overhead for performing these calculations may limit the use of this feature. Work will be done to minimize this overhead, but the ability to reduce it may be limited due to the nature of the shielding calculation that must be performed.

2.2 Plan for Improved VERA Input for Transient

Since most of the user support effort focused on improving the output, only some progress was made on implementing a more usable input. To get the transient capability initially available through the VERA input, the input approach used for the standard input was quickly adapted to VERAIn. It was known during this process that this would be a prototype capability for the transient input. In working with the transient capability through the VERA input and getting this capability to AMA, several useful suggestions were provided by AMA about how the input could be improved.

The general suggestions given for improving the VERA input for transient were:

1. Allow for changing more of the core operating conditions through the transient (e.g. inlet temperature, flow rate, boron concentration etc.).
2. Simplify the input for the RIA so that the rod position does not need to be specified for each time step.

Some use cases for the proposed improved input are given by the following examples.

```
[STATE]
 power 100.0
 feedback on
 sym qtr
 transient_time 0.0
 rod_bank A 0
 B 0
 C 0
[STATE]
 transient_time 3.0 !Simulate to this time

[MPACT]
 transient_dt constant 0.005
```

Figure 2.1 - Example of VERA Input for Null Transient

```
[STATE]
 power 100.0
 feedback on
 sym qtr
 transient_time 0.0
 bank_pos A 0
 B 0
 C 0
[STATE]
 transient_time 0.08
 bank_pos C 200
[STATE]
 transient_time 3.0

...

[MPACT]
 transient_dt variable
 0.002 0.08
 0.004 3.0
```

Figure 2.2 - Example of VERA Input for RIA

```
[STATE]
 power 100.0
 feedback on
 sym qtr
 transient_time 0.0
 bank_pos A 200
 B 200
 C 0
[STATE]
 transient_time 0.02
[STATE]
 transient_time 0.08
 bank_pos C 200
[STATE]
 transient_time 0.1
[STATE]
 transient_time 1.5
[STATE]
 transient_time 1.58
 bank_pos A 0
 B 0
[STATE]
 transient_time 1.6
[STATE]
 transient_time 1.8
[STATE]
 transient_time 3.0

...

[MPACT]
 transient_dt adaptive
```

Figure 2.3 Example VERA Input for RIA followed by SCRAM

The idea behind this approach is that the `[STATE]` block is used to define specific states within the transient. This approach would require at least two new cards:

- `transient_dt` - defines a constant time step to be used until otherwise specified
  - Usage:

```
[MPACT]
 transient_dt    <method>    <value    1>    [<value    2>    ...]
```

  - As newer capabilities are implemented into MPACT for variable time stepping and adaptive time stepping control this option can change.
  - The time step discretization should not appear in the `[STATE]` block because this is code specific.
- `transient_time` - used to specify the state defines a point in time during the transient.
  - Usage:

```
[STATE]
 transient_time                                          <seconds>
```

- For transient simulations this card should be present in the first state block and have a value of 0 to indicate the initial steady-state condition.
- For transient simulations all state blocks in the input MUST have this entry.
  - The purpose of this is to simplify the complexity of the types of simulations that may be performed in a single input by VERA-CS (and consequently the code logic). Basically all inputs are either transient or steady-state.
- All values defined in the state block with `transient_time` are assumed to have those values at that exact point in time.
  - The values of `[STATE]` block variables preceding a given `[STATE]` (except the first state) are assumed to vary linearly between the states.
  - Values that do not change between states carryover.

At this point this is the proposed input for transients in the VERA input. Feedback from stakeholders in AMA is still required before proceeding with an implementation.

3. METHODS IMPROVEMENTS

3.1 User Controlled Variable Time-Stepping

The transient capability for MPACT has been expanded to include an option for variable time-stepping. This option allows for more refined time steps to resolve the rapidly evolving portions of the transient and larger time steps when the system is changing more slowly. Thus, the computational burden can be reduced without sacrificing accuracy. For practical use, this requires some *a priori* knowledge of the evolution of the simulated transient. This somewhat limits the realized speed-up feature until one has gained some experience with the simulation. However, the variable time-stepping capability is a first step towards an adaptive time-stepping strategy, and is useful for analysis that require perturbations to the initial conditions or some other parameter. This feature will automatically adjust the time step size based on the evolution of system parameters to optimize the balance between accuracy and computational speed.

The variable time-stepping feature was implemented by adding an entry on the perturbation card of the transient block. The time step size for each perturbation is now dictated by the third numerical entry on the perturbation card, after the perturbation end time and before the perturbation type. This entry is obligatory, even if using multiple perturbations with the same time step size. An example is provided below:

```
perturb 0.0 0.01 0.001 mvcr 1 1 1
0.01 0.1 0.0025 const 1 1 1
0.1 0.5 0.005 const 1 1 1
```

This transient would be driven by control rod movement from 0 to 10 ms with 1 ms timesteps (thereby requiring 10 additional state cards to dictate the control rod position at each interval under the current input format), and then run with 2.5 ms time steps from 10 ms to 100 ms and 5 ms time steps from 100 ms to 500 ms. Ostensbily, this transient would be rapidly evolving during the control rod movement, requiring fine time steps to resolve the solution, while larger time steps would be sufficient after the control rod movement has ceased, and even larger time steps would be sufficient for the tail end of the transient when the system is changing slowly.

To evaluate the time savings limits of the user controlled variable time stepping, the hypothetical SMR problem was studied. In this problem the transient was simulated to 0.5 s with the time step size changing once power goes asymptotic after the pulse. Prior to this point the time step was 5 ms, and various time steps of 10, 20, 50, and 100 ms were used in simulating the asymptotic region. From this study the relative time savings were observed to be:

Table 3.1 Potential Time Savings from Variable Time-Stepping

Time steps	Wall time (min)	Savings
5 ms / 5 ms	306	---
5 ms / 10 ms	257	16%
5 ms / 20 ms	223	27%
5 ms / 50 ms	199	35%
5 ms / 100 ms	189	38%

Variations in the power at the end of the transient were less than 3.5% which was always the limiting case.

3.2 1-group CMFD Acceleration

3.2.1 Introduction

Recently, an innovative Predictor-Corrector Quasi-static Method(PCQM) called Transient MultiLevel (TML), is developed and applied into the transient solver of MPACT. In the TML scheme, two levels of coupling are used between 3D-transport/3D-CMFD and 3D-CMFD/EPKE. For each level, the flux is solved by coarse predictor with coarse time step and then adjusted by corrector with multiple fine time step. The TML scheme makes it feasible to simulate RIA with reasonable time. For the assembly calculation for SPERT transient benchmark experiment, MPACT achieves the same order of accuracy with TML as the pure 3D-transport/3D-CMFD method, while reducing the total simulation time by a factor of 7. Nevertheless, it stills takes considerable time to run whole-core transient calculations. Even using simplified-TH solver for thermal feedback in MPACT, it takes around 2 hours to run SPERT Test 86 benchmark with 2880 cores, and 3 hours with about 4000 cores for Watts Bar HFP transient case on the Titan compute cluster at ORNL. One way to solve this problem is to improve the CMFD efficiency in MPACT, due to large percentage of the total calculation for CMFD part, as shown Figure 3.1.

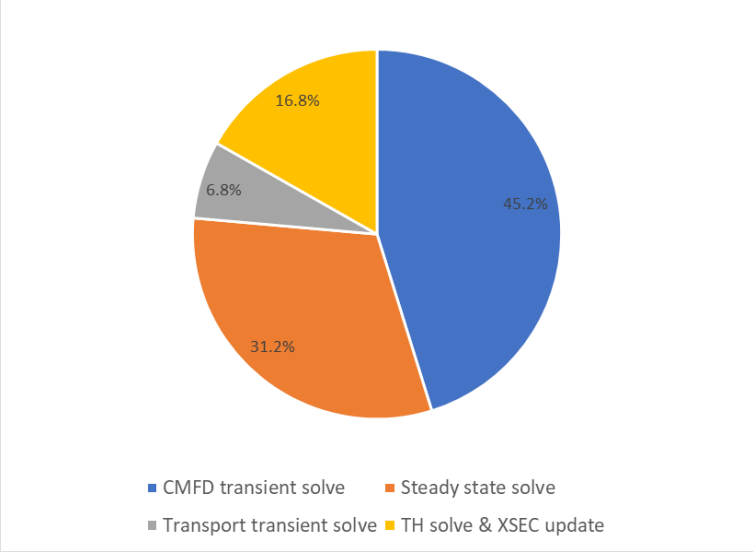

Figure 3.1. Typical Percentage running time for different modules

The reason CMFD calculation is very time-consuming is that, in transient calculation the multigroup CMFD(MGCMFD) linear system is constructed during each time step and it's approximately singular. Therefore, it requires a large number inner iteration to converge the solution. To deal with problem, 1-group CMFD acceleration method is adopted in TML to accelerate solving MGCMFD system. The idea behind this method is that 1GCMFD accurate enough to calculate coarse mesh wise fission source distribution and the fission source could be moved to the RHS of MGCMFD system. Therefore MGCMFD is not singular and is much easier to solve, and the total calculation time can be reduced remarkably.

The rest of this section is organized as follows. The theory of TML as well as 1GCMFD acceleration will be discussed in subsection 3.1.2. In subsection 3.1.3, the minicore test is used to test the1GCMFD acceleration method. Finally, in subsection 3.1.4 discussion and future work would be given.

3.2.2. Theory

3.2.2.1 3D-Transport Transient Equation

The 3D transport transient solver begins with the time-dependent Boltzmann equation:

$$\begin{aligned}&\frac{1}{v(E)}\frac{\partial\varphi(\mathbf{r},\mathbf{\Omega},E,t)}{\partial t}+\Sigma_t(\mathbf{r},E,t)\varphi(\mathbf{r},\mathbf{\Omega},E,t)+\mathbf{\Omega}\cdot\nabla\varphi(\mathbf{r},\mathbf{\Omega},E,t)=\\&\int_0^\infty\int_0^{4\pi}\Sigma_s(\mathbf{r},\mathbf{\Omega}\cdot\mathbf{\Omega}',E'\to E,t)\varphi(\mathbf{r},\mathbf{\Omega}',E',t)d\mathbf{\Omega}'dE'\\&+\frac{1}{4\pi}\chi_p(\mathbf{r},E,t)(1-\beta(\mathbf{r},t))S_F(\mathbf{r},t)+\frac{\chi_p(\mathbf{r},E,t)S_d(\mathbf{r},t)}{4\pi}\end{aligned}\tag{2.1}$$

where S_F is the total neutron fission source and S_d is the neutron delayed source, and are defined as

$$S_F(\mathbf{r},t)=\frac{1}{k_{eff}^s}\int_0^\infty\Sigma_f(\mathbf{r},E',t)\phi(\mathbf{r},E',t)dE'\tag{2.2}$$

$$S_d(\mathbf{r},t)=\sum_{k=1}^{n}\lambda_k C_k(\mathbf{r},t)\tag{2.3}$$

As shown above, S_F is adjusted by the eigenvalue determined in the steady state calculations. For time discretization, the Backward Euler is used. The time derivative term at the n_{th} time step for the given time interval Δt could be expressed as

$$\frac{1}{v(E)}\frac{\partial\varphi^n(\mathbf{r},\mathbf{\Omega},E)}{\partial t}\approx\frac{\varphi^{n+1}(\mathbf{r},\mathbf{\Omega},E)-\varphi^n(\mathbf{r},\mathbf{\Omega},E)}{v(E)\Delta t}\approx\frac{\phi^{n+1}(\mathbf{r},E)-\phi^n(\mathbf{r},E)}{4\pi v(E)\Delta t}\tag{2.4}$$

For the delay fission source part, a second-order approximation is used and therefore expressed as:

$$S_d^n(\mathbf{r})=\omega^n(\mathbf{r})S_F^n(\mathbf{r})+S_d^{n-1}(\mathbf{r})\tag{2.5}$$

where $S_d^{n-1}(\mathbf{r})$ is a source term related with the precursor and fission source for the previous two steps. As a result, the 3D-Transport Transient Equation is transformed into a Transient Fixed Source Problem(TFSP), written as

$$\begin{aligned}&\mathbf{\Omega}\cdot\nabla\varphi^n(\mathbf{r},\mathbf{\Omega},E)+\Sigma_t^n(\mathbf{r},E)\varphi^n(\mathbf{r},\mathbf{\Omega},E)=\\&\int_0^\infty\int_0^{4\pi}\Sigma_s^n(\mathbf{r},\mathbf{\Omega}\cdot\mathbf{\Omega}',E'\to E)\varphi^n(\mathbf{r},\mathbf{\Omega}',E)d\mathbf{\Omega}'dE'+\frac{1}{4\pi}\chi^n(\mathbf{r},E)S_F^n(\mathbf{r})+\frac{S_{tr}^n(\mathbf{r},E)}{4\pi}\end{aligned}\tag{2.6}$$

Here

$$\chi^n(\mathbf{r},E)=\chi^n{}_p(\mathbf{r},E)(1-\beta^n(\mathbf{r}))+\chi^n{}_d(\mathbf{r},E)\beta^n(\mathbf{r})\tag{2.7}$$

$$
\begin{aligned}
&S_{tr}^{n}(\mathbf{r},E)=A(\mathbf{r},E)\phi^{n}(\mathbf{r},E)+B(\mathbf{r},E)S_{F}^{n}(\mathbf{r},E)+C^{n}(\mathbf{r},E)\\
&A^{n}(\mathbf{r},E)=\frac{-\phi^{n}(\mathbf{r},E)}{v(E)\Delta t}\\
&B^{n}(\mathbf{r},E)=\chi_{d}(\mathbf{r},E)(\omega^{n}(\mathbf{r})-\beta^{n}(\mathbf{r}))\\
&C^{n}(\mathbf{r},E)=\chi_{d}(\mathbf{r},E)S_{d}^{n-1}(\mathbf{r})+\frac{\phi^{n-1}(\mathbf{r},E)}{v(E)\Delta t}
\end{aligned}
\tag{2.8}
$$

3.2.2.2 3D-CMFD Transient Equation

The 3D-CMFD transient Equation could be written as

$$
\begin{aligned}
&\frac{1}{v(E)}\frac{\partial\phi(\mathbf{r},\mathbf{\Omega},t)}{\partial t}=-\Sigma_{t}(\mathbf{r},E,t)\phi(\mathbf{r},E,t)+\nabla\cdot D(\mathbf{r},E)\nabla\phi(\mathbf{r},E,t)+\int_{0}^{\infty}\Sigma_{s}(\mathbf{r},E'\rightarrow E,t)\phi(\mathbf{r},E',t)dE'\\
&+\chi_{p}(\mathbf{r},E,t)(1-\beta(\mathbf{r},t))S_{F}(\mathbf{r},t)+\chi_{p}(\mathbf{r},E,t)S_{d}(\mathbf{r},t)
\end{aligned}
\tag{2.9}
$$

By using the same time-discretization method, the 3D-CMFD TFSP could be formed as

$$
\begin{aligned}
&-\nabla\cdot D^{n}(\mathbf{r},E)\nabla\phi^{n}(\mathbf{r},E)+\Sigma_{t}^{n}(\mathbf{r},E)\phi^{n}(\mathbf{r},E)=\int_{0}^{\infty}\Sigma_{s}^{n}(\mathbf{r},E)\phi^{n}(\mathbf{r},E')dE'\\
&+\chi^{n}S_{F}^{n}(\mathbf{r})+S_{tr}^{n}(\mathbf{r},E)
\end{aligned}
\tag{2.10}
$$

Just the same as 3D-Transport TFSP, the CMFD transient fixed source equation could be written as

$$
S_{tr}^{n}(\mathbf{r})=A(\mathbf{r},E)\phi^{n}(\mathbf{r},E)+B(\mathbf{r},E)S_{F}^{n}(\mathbf{r},E)+C^{n}(\mathbf{r},E) \tag{2.11}
$$

In the multigroup form,

$$
-\nabla\cdot\mathbf{J}_{g}^{n}(\mathbf{r},E)+\Sigma_{t}^{n}(\mathbf{r})\phi_{g}^{n}(\mathbf{r})-\sum_{g'}\Sigma_{g'\rightarrow g}\phi_{g'}^{n}(\mathbf{r})=\chi_{g}^{n}S_{F}^{n}(\mathbf{r})+S_{tr,g}^{n}(\mathbf{r}) \tag{2.12}
$$

Define

$$
\begin{aligned}
&\mathbf{M}=-\nabla\cdot D_{g}^{n}(\mathbf{r})\nabla\\
&\mathbf{S}=\sum_{g'}\Sigma_{s,g'\rightarrow g}\\
&\mathbf{F}=\chi_{g}^{n}v\Sigma_{f,g}\\
&\mathbf{S_{tr}}=\mathbf{A}\Phi+\mathbf{BF}\Phi+\mathbf{C}
\end{aligned}
\tag{2.13}
$$

Then the 3D-CMFD TFSP could be written as

$$
\mathbf{(M-S-F-A-BF)\Phi=C} \tag{2.14}
$$

The cross sections in each coarse mesh are calculated by homogenization from 3D-Transport TFSP. For each CMFD problem, it takes only one outer iteration to solve. However, this linear system is almost singular, and takes a lot of inner iterations to get converged results.

3.2.2.3 Transient MultiLevel Methodology

The TML iteration scheme is illustrated in Figure 3.2. For each time step, the 3D-transport TFSP is solved first and the angular subpin distribution is calculated. In this level, the angular and spatial distribution inside the coarse mesh is assumed to be accurate while the amplitude of the scalar flux in each coarse mesh is not accurate. For intermediate time step, the CMFD coefficients are calculated by linear interpolation with the coefficients at the beginning and end of the coarse time step. Then the CMFD TSFP is solved and the angular flux is corrected by the CMFD scalar flux. In this step, the spatial distribution is assumed to accurate but the corewise amplitude is not accurate. Then in the EPKE level, the corewise amplitude is calculated, and the subpin angular flux and CMFD scalar flux are corrected.

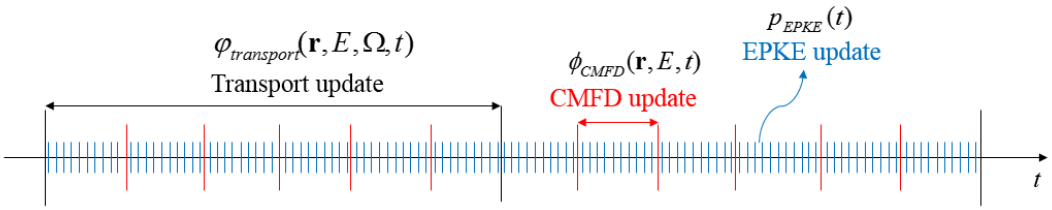

Figure 3.2 Illustration of TML iteration scheme

3.2.2.4 1-Group CMFD Acceleration

1-group CMFD(1GCMFD) is a lower-order method in Energy space to accelerate the MGCMFD calculation. It has been adopted into the Multilevel in Space and Energy Diffusion(MSED) scheme to solve the multigroup diffusion eigenvalue problem. The idea of 1GCMFD acceleration in transient solver is just the same at that in MSED, i.e. 1GCMFD is used to converge the fission source. Therefore, the fission source stays at the RHS of linear system and MGCMFD system don't turn singular and become easier to solve.

The spatially discretized MGCMFD equation for TFSP is written as:

$$\sum_s A_s J^{net}_{g,m,s} + (\Sigma^n_{t,m,g}\phi^n_{g,m} - \sum_{g'} \Sigma^n_{t,m,g'\to g}\phi^n_{g'})V_m = (\chi^n_{g,m}S^n_{F,m} + S^n_{tr,g,m})V_m \tag{2.15}$$

where *m* denotes the coarse mesh index, and *s* denotes the index of surface

$$J^{net}_{g,m,s} = -D_{g,m,s}(\phi^n_{g,m} - \phi^n_{g,m(s)}) + D_{g,m,s}(\phi^n_{g,m} + \phi^n_{g,m(s)}) \tag{2.16}$$

Sum the Eq.(2.15) over g, the equation turns to be

$$\sum_s A_s J^{net}_{m,s} + <\Sigma^n_{a,m}>\Phi^n_m V_m = (\chi^n_m S^n_{F,m} + S^n_{tr,m})V_m \tag{2.17}$$

Where Φ_m^n is the 1G flux, and corresponding coefficients are collapsed as:

$$\Phi_m^n = \sum_g \phi_{g,m}^n \tag{2.18}$$

$$<\Sigma_{a,m}^n> = \frac{\sum_g \Sigma_{a,m,g}^n \phi_{g,m}^n}{\Phi_m^n} \tag{2.19}$$

$$\chi_m^n = \sum_g \chi_{g,m}^n \tag{2.20}$$

$$S_{Fm}^n = \sum_g \nu\Sigma_{f,g,m}^n \phi_{g,m}^n = <\nu\Sigma_{f,m}^n> \Phi_m^n \tag{2.21}$$

$$S_{tr,m}^n = <A_m^n> \Phi_m^n + B_m^n S_{F,m}^n + C_m^n \tag{2.22}$$

$$<A_m^n> = \frac{\sum_g A_{m,g}^n \phi_{g,m}^n}{\Phi_m^n} \tag{2.23}$$

$$B_m^n = \sum_g B_{g,m}^n \tag{2.24}$$

$$C_m^n = \sum_g C_{g,m}^n \tag{2.25}$$

For current term,

$$J_{m,s}^{net} = -<D_{m,s}>(\Phi_m^n - \Phi_{m(s)}^n) + <D_{m,s}>(\Phi_m^n + \Phi_{m(s)}^n) \tag{2.26}$$

$$<D_{m,s} + D_{m,s}> = \frac{\sum_g (D_{m,s} + D_{m,s})\phi_{g,m(s)}^n}{\Phi_{m(s)}^n}$$

$$<D_{m,s} - D_{m,s}> = \frac{\sum_g (D_{m,s} - D_{m,s})\phi_{g,m}^n}{\Phi_m^n} \tag{2.27}$$

$$<D_{m,s}> = \frac{-<D_{m,s} - D_{m,s}> + <D_{m,s} + D_{m,s}>}{2}$$

$$<D_{m,s}> = \frac{<D_{m,s} - D_{m,s}> + <D_{m,s} + D_{m,s}>}{2}$$

Written

$$J_{m,s}^{net} = M_1 \Phi_1 \tag{2.28}$$

$$<\Sigma_{a,m}^n> = R_1 \tag{2.29}$$

Then the 1GCMFD TFSP is written as

$$(\mathbf{M_1 - R_1 - A_1 - B_1 F_1 - F_1})\mathbf{\Phi_1} = \mathbf{C_1} \tag{2.30}$$

In 1GCMFD acceleration, the coefficient $(\mathbf{M}_1, \mathbf{R}_1, \mathbf{A}_1, \mathbf{B}_1\mathbf{F}_1, \mathbf{F}_1)$ is collapsed by the flux from MGCMFD calculation in previous step. Then 1G scalar flux distribution are calculated and the fission source are updated. Then the MG scalar flux can be calculated by

$$(\mathbf{M}-\mathbf{S}-\mathbf{A})\Phi=\mathbf{C}+(\chi+\mathbf{B})\mathbf{F}_1\Phi_1 \tag{2.31}$$

In TML, MG-CMFD is used in following two parts, First, MG-CMFD is used in the 3D-transport TFSP to accelerate the convergence of transport problem. In this part, only 1 1GCMFD/MGCMFD coupled outer iteration is used for each transport iteration. This is because, if the source distribution from transport part are not accurate, the 1G-CMFD could not be accurate. Therefore, there's no need to use 1G-CMFD to converge the source with multiple inner iterations. MG-CMFD is also used in CMFD level in TML scheme. In this scheme, there are multiple 1GCMFD/MGCMFD coupled iterations for each intermediate interval. The reason is that at the beginning, the coefficient of 1GCMFD is homogenized by flux in previous intermediate time step. The coefficient is not accurate. Therefore multiple outer iterations are needed to get correct 1GCMFD coefficient. Typically, the maximum 1G-CMFD/MG-CMFD coupled iterations are set to be 3. The flow chart for TML with 1G-CMFD is shown in Figure 3.

3.2.3. Test and Results

To test the result, the minicore transient problem is used. It's a 3X3 core with 7X7 assembly. 47g library is used. The results are obtained using the TML scheme with 1GCMFD and with/o 1GCMFD acceleration, on the Nightfort server with 9 cores. As indicated by Figure 4, Fig 5 and Table 1, using 1GCMFD, the time of simulation can be reduced by 40%, while the accuracy is unaffected (the maximum error is in reactivity no more than 0.2%).

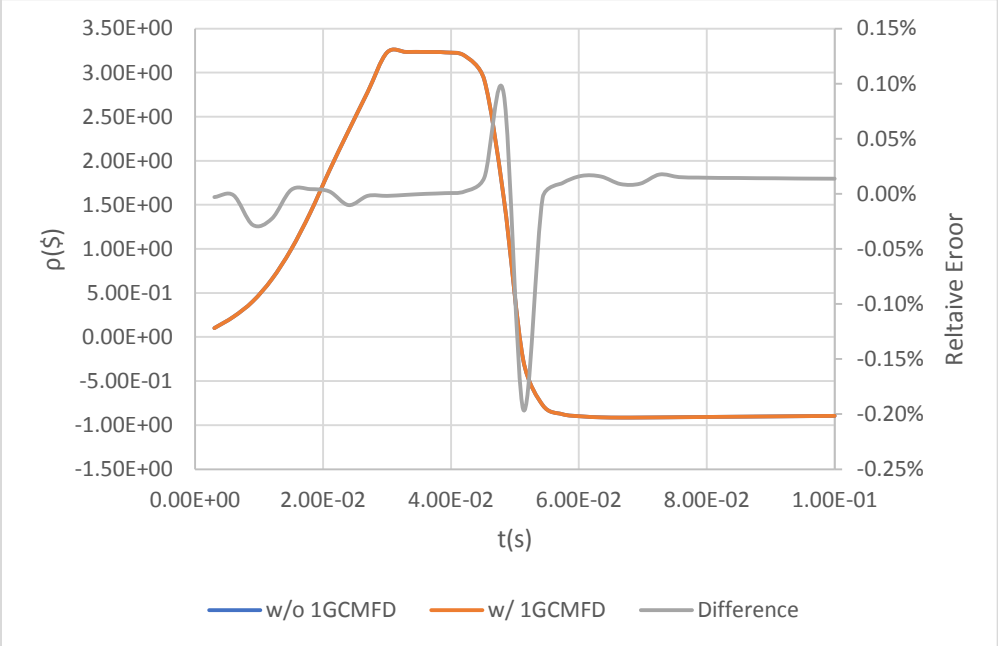

Figure 3.3 Comparison of Reactivity of w/o 1GCMFD and w/ 1GCMFD cases

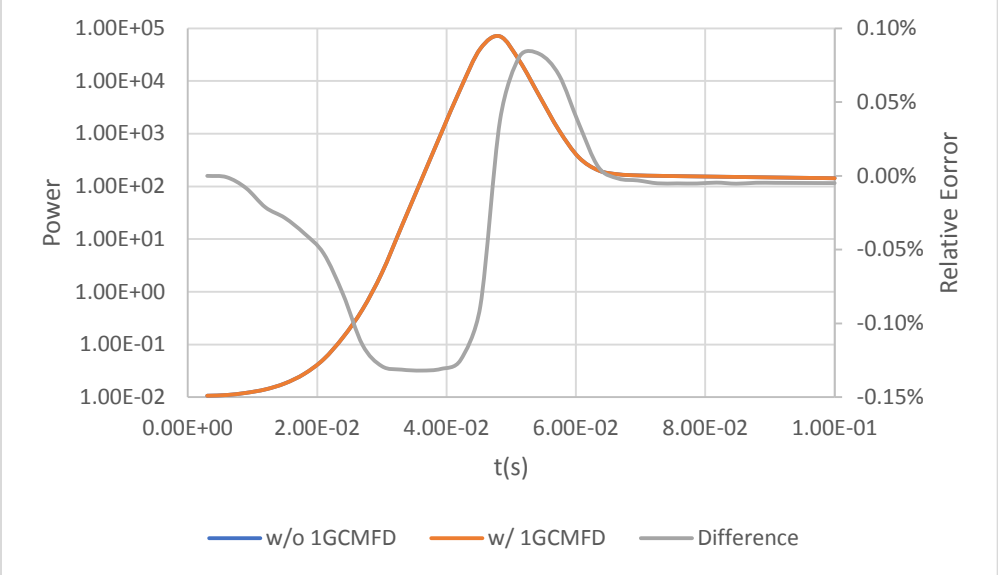

Figure 3.4 Comparison of Power of w/o 1GCMFD and w/ 1GCMFD cases

Table 3.2 Comparison of total calculation time of w/o 1GCMFD and w/ 1GCMFD cases

	w/o 1GCMFD	w/1GCMFD	Time Reduction
Time	55.8 min	32.8 min	40.5%

3.2.4. Discussion and Future Work

A preliminary 1G-CMFD acceleration is implemented into the TML scheme of MPACT. For a simple test, it shows a potential to reduce the total calculation time by around 40%. In future work, it will be tested for a larger problem such as SPERT Test 86. At the same time, a one-group CMFD level will be added into the TML scheme to reduce the number of MG-CMFD iterations.

3.3 Delayed Energy Deposition Model

The energy released by a fission event consists of various energy modes. Most energy are released instantaneously in the form of kinetic energy from fission products and fission neutrons, prompt gamma rays, or gamma rays from the capture of neutrons. An additional 7% (approximately) of energy are released some time after the fission event, from the radioactive decay of fission products, in the form of delayed beta and gamma rays.

For the nominal reactor burnup calculation to compute the flux re-normalization factor, we have verified in a separate effort that the explicit delayed energy model does not result in significant difference with regard to the depletion isotopics and k-eff as compared to the equilibrium delayed energy. This is because the time scale for the delayed energy modes to achieve equilibrium is relatively small, leading to a negligible time-integrated effect on the depletion rate of isotopes. However, for fast transients such as RIAs, we are interested in a power excursion typically within a second. In such time scale, the delayed energy release is lagged, in response to the drastic changes of power, which should be considered explicitly.

3.3.1 Proposed explicit delayed energy model

We start with writing the thermal power of a reactor into a prompt component and a delayed component,

$$P(t) = P_{pr}(t) + P_{de}(t) \tag{3.1}$$

As mentioned previously, the prompt power $P_{pr}(t)$ is contributed from the energy release of the prompt modes that directly relate to neutron fission and capture rates, i.e.,

$$P_{pr}(t) = f\sum_j V_j \left((1-\gamma)\sum_{iso} \kappa_{f,iso} N_{iso,j} \sum_g \sigma_{f,g,iso,j}\phi_{g,j} + \sum_i \kappa_{c,iso} N_{iso,j} \sum_g \sigma_{c,g,iso,j}\phi_{g,j} \right) \tag{3.2}$$

where f is the flux normalization factor to match the core thermal power.

To determine the delayed power $P_{de}(t)$, we assume the numerous components of the delayed heat source can be lumped into a relatively small number of "groups", similar to the approach taken with delayed neutrons. If $D_{m,j}$ is defined as the concentration of delayed heat group *m* at region *j*, then the balance equation that $D_{m,j}$ satisfies is given as

$$\frac{dD_{m,j}(t)}{dt} = \gamma_m f V_j \sum_{iso} \kappa_{f,iso} N_{iso,j} \sum_g \sigma_{f,g,iso,j}\phi_{g,j} - \lambda_m D_{m,j}(t) \tag{3.3}$$

where γ_m and λ_m are the yield and decay constant of delayed heat group *m* (see Table 1). By using $D_{m,j}$, the delayed power is written as,

$$P_{de}(t) = \sum_j \sum_m \lambda_m D_{m,j}(t) \tag{3.4}$$

Rather than using Eq. (3.1), our current approach to evaluate the thermal power for both steady state and transient calculations is simplified as Eq. (3.5) by assuming the equilibrium delayed power,

$$P(t) = f\sum_j V_j \left(\sum_{iso} \kappa_{f,iso} N_{iso,j} \sum_g \sigma_{f,g,iso,j}\phi_{g,j} + \sum_i \kappa_{c,iso} N_{iso,j} \sum_g \sigma_{c,g,iso,j}\phi_{g,j} \right) \tag{3.5}$$

In a transient calculation, the normalization factor f is computed from the steady state calculation at the beginning to initialize the transient calculation. Unlike depletion calculation, f is a constant throughout the transient. For each transient time step, the power is updated after the transport solve (with solution correction using TML) and before the TH solve, as shown in Fig. 3.5.

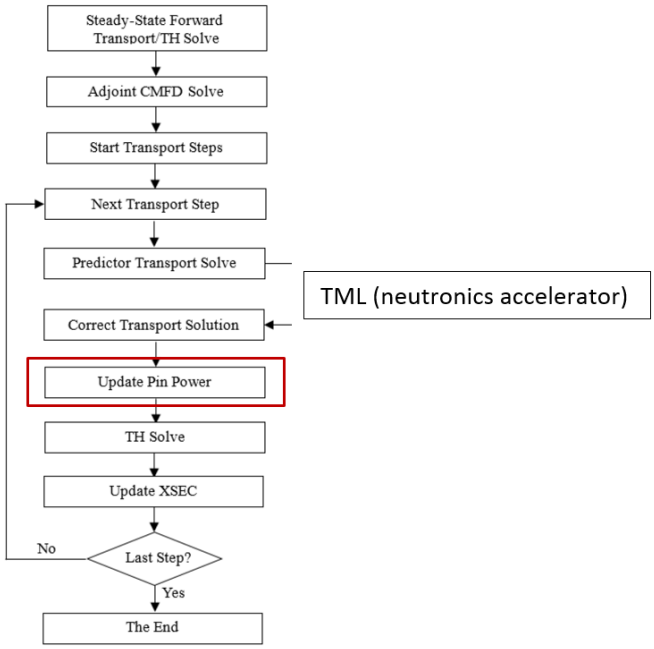

Figure 3.5 Flow chart for transient calculation with TH feedback

Although the delayed energy can be assumed on equilibrium at t=0, it is problematic to use Eq. (3.5) at t>0, since the delayed energy release from the increased power should be lagged. Eqs. (3.1-3.4) can be used to model the delayed power explicitly.

3.3.2 Preliminary results

Table 3.3 shows the typical yields and decay constants of a 11-group delayed heat set obtained by fitting the data from 1973 ANS decay heat standard [1]. These data are currently used to demonstrate the delayed energy effect for RIAs. We ran a PWR pin cell case with a ramp reactivity insertion up to 1.4$ at the beginning of 0.05s to compare the equilibrium and explicit delayed energy models.

Table 3.3 Data of delayed heat group

Delayed heat group	Yield	Decay Constant (1/s)
1	2.990E-03	1.772E+00
2	8.250E-03	5.774E-01
3	1.550E-02	6.743E-02
4	1.935E-02	6.214E-03
5	1.165E-02	4.739E-04
6	6.450E-03	4.810E-05
7	2.310E-03	5.344E-06
8	1.640E-03	5.726E-07
9	8.500E-04	1.036E-07
10	4.300E-04	2.959E-08
11	5.700E-04	7.585E-10

First the thermal feedback is turned off to verify the exponential power with two energy models. From Fig. 3.6, the power with explicit delayed energy model quickly approaches 7% low as

compared to the equilibrium model. This is reasonable since trivial amount of delayed energy could be released out of the increased power within 0.2 second. As shown in Fig. 3.7, the power difference becomes smaller due to the thermal feedback, and the power shape with explicit model is a little shifted to the right. Although the difference is not as large as the fraction of delayed energy, modeling the delayed energy explicitly should improve the accuracy of transient calculation, given the additional computation for the explicit model is small.

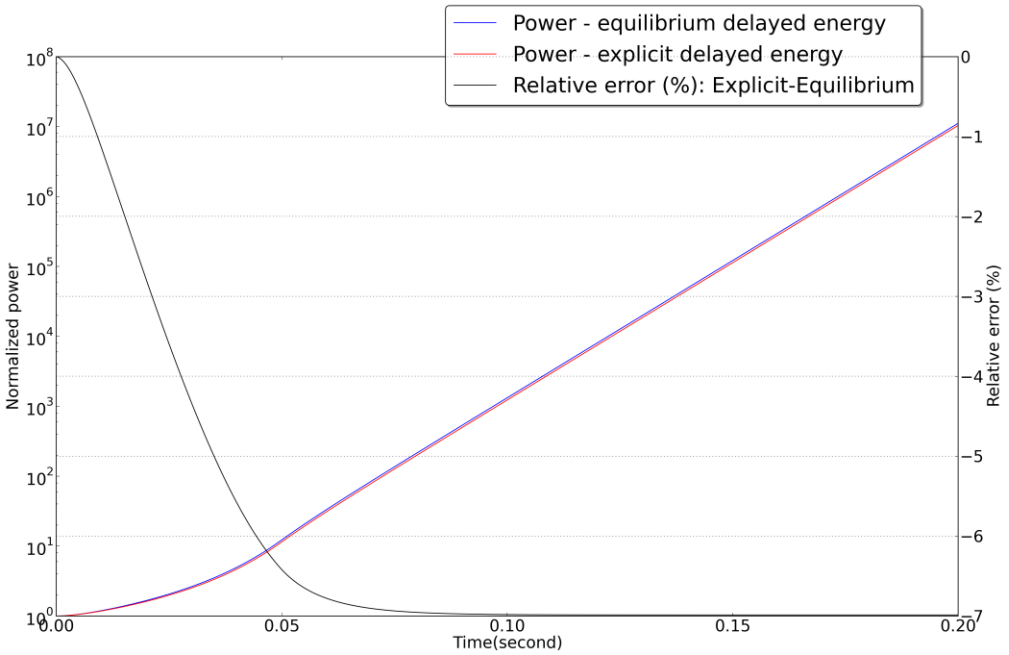

Figure 3.6 Power history without thermal feedback

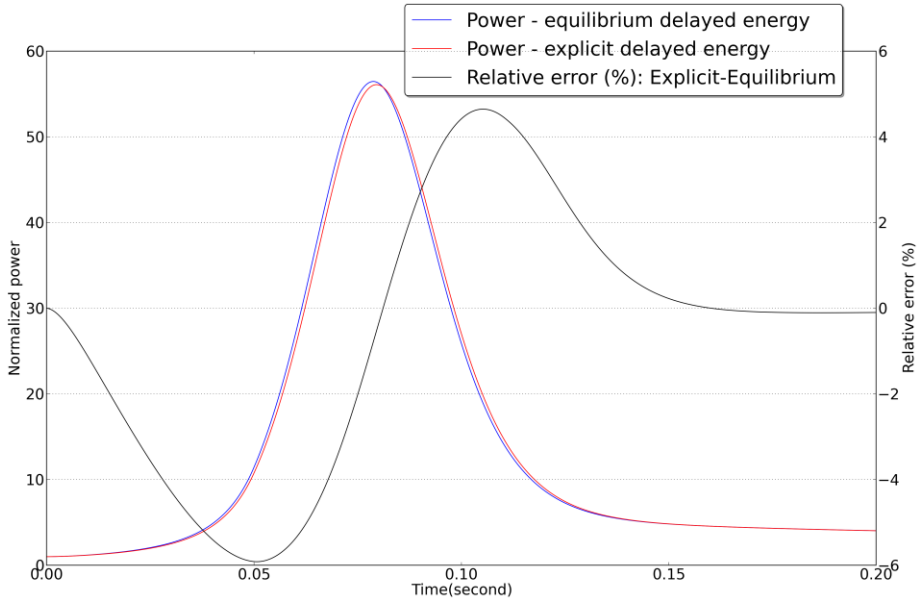

Figure 3.7 Power history with thermal feedback

3.4 Improved Robustness

During the initial evaluation of MPACT coupled to CTF, a number of bugs and subsequent issues were uncovered in the implementation of the transient within MPACT. The bug that was identified

was that the transient source (e.g. time derivative and delayed neutron precursors) was getting set to zero prior to the MOC sweeps for the transient fixed source problem.

Once this bug was resolved severe robustness issues were encountered. After some investigation it was found that the MOC transient fixed source problem had robustness issues when the model contained flat source regions with small optical thicknesses.

Finally, a third issue related to robustness was uncovered that involved the transverse leakage.

3.4.1 MOC transient fixed source problem with low density regions

Many of the models developed for VERA-CS include low density regions. Typically this is the fuel-clad gap in the fuel rods, the upper plenum region of the fuel rods above the active fuel, and gap regions in pyrex inserts and control rods. Even though the fuel-clad gap regions are small, if there are a sufficient number of them then they can cause the MOC iteration to become unstable.

This can be illustrated from a theoretical standpoint when considering a continuous multigroup time-dependent transport equation given by:

$$\frac{1}{v_g(\mathbf{r})}\frac{\partial \varphi_g(\mathbf{r},\mathbf{\Omega},t)}{\partial t}+\mathbf{\Omega}\cdot\nabla\varphi_g(\mathbf{r},\mathbf{\Omega},t)+\Sigma_{t,g}(\mathbf{r},t)\varphi_g(\mathbf{r},\mathbf{\Omega},t)= S_{s,g}(\mathbf{r},\mathbf{\Omega},t)+\frac{\tilde{\chi}_g(\mathbf{r})}{4\pi k_{eff}}S_F(\mathbf{r},t)+S_{tr,g}(\mathbf{r},t), \tag{3.6a}$$

where

$$\tilde{\chi}_g(\mathbf{r})=\chi_g(\mathbf{r})+\sum_k \chi_{d,k,g}\left(\lambda_k\tilde{C}_k(\mathbf{r},t)-\beta_k(\mathbf{r})\right), \tag{3.6b}$$

$$\chi_g(\mathbf{r})=\chi_{p,g}+\sum_k \beta_k(\mathbf{r})\left(\chi_{d,k,g}-\chi_{p,g}\right), \tag{3.6c}$$

$$S_{tr,g}(\mathbf{r},t)=\sum_k \chi_{d,k,g}\lambda_k C_k(\mathbf{r},t), \tag{3.6d}$$

and the precursor equations are:

$$\frac{\partial C_k(\mathbf{r},t)}{\partial t}=\beta_k(\mathbf{r})S_F(\mathbf{r},t)-\lambda_k(\mathbf{r})C_k(\mathbf{r},t)\quad k=1,2,\ldots. \tag{3.7}$$

Here S_F is the fission source, and S_S is the scattering source.

In MPACT the time discretization is performed using the isotropic approximation:

$$\frac{1}{v_g(\mathbf{r})}\frac{\partial\varphi(\mathbf{r},\mathbf{\Omega},t)}{\partial t}\approx\frac{1}{v_g(\mathbf{r})4\pi}\frac{\partial\phi(\mathbf{r},t)}{\partial t}, \tag{3.8}$$

and the numerical method for the time integration is implicit Euler. This leads to the following time discretized transport equation:

$$\mathbf{\Omega}\cdot\nabla\varphi_g^n(\mathbf{r},\mathbf{\Omega})+\Sigma_{t,g}^n(\mathbf{r})\varphi_g^n(\mathbf{r},\mathbf{\Omega})=S_{s,g}(\mathbf{r},\mathbf{\Omega})+\frac{\tilde{\chi}_g^n(\mathbf{r})}{4\pi k_{eff}}S_F^n(\mathbf{r},t)+S_{tr,g}^n(\mathbf{r})-\frac{\phi_g^n(\mathbf{r})-\phi_g^{n-1}(\mathbf{r})}{v_g(\mathbf{r})\Delta t_n 4\pi}, \tag{3.9}$$

where the superscript n is the time step index.

If one examines the terms on the right hand side of Eq. (3.9) and considers a low density or nearly voided region that is not fissionable, then we have:

$$\boldsymbol{\Omega}\cdot\nabla\varphi_g^n(\mathbf{r},\boldsymbol{\Omega})+\Sigma_{t,g}^n(\mathbf{r})\varphi_g^n(\mathbf{r},\boldsymbol{\Omega})=\overbrace{S_{s,g}(\mathbf{r},\boldsymbol{\Omega})}^{\varepsilon}+\frac{\tilde{\chi}_g^n(\mathbf{r})}{4\pi k_{eff}}\overbrace{S_F^n(\mathbf{r},t)}^{0}+\overbrace{S_{tr,g}^n(\mathbf{r})}^{0}-\frac{\phi_g^n(\mathbf{r})-\phi_g^{n-1}(\mathbf{r})}{v_g(\mathbf{r})\Delta t_n 4\pi},$$

$$\boldsymbol{\Omega}\cdot\nabla\varphi_g^n(\mathbf{r},\boldsymbol{\Omega})+\Sigma_{t,g}^n(\mathbf{r})\varphi_g^n(\mathbf{r},\boldsymbol{\Omega})=\varepsilon-\frac{\phi_g^n(\mathbf{r})-\phi_g^{n-1}(\mathbf{r})}{v_g(\mathbf{r})\Delta t_n 4\pi}. \tag{3.10}$$

It is clear that the time derivative on the right hand side of Eq. (3.10) can contribute negatively if the flux is increasing with respect to time. Moreover, it possible for this term drive the whole RHS of Eq. (3.10) negative. A negative source in the 2D MOC sweep will produce negative fluxes. Thus, something must be done to ensure non-negativity of the RHS of Eq. (3.9).

This is effectively the same issue experienced previously for the transverse leakage term in the 2D MOC equation of the 2D/1D method. For steady state this is illustrated by the following equation:

Previously, the transverse leakage issue was solved by transverse leakage splitting. Thus, a similar approach to ensuring a positive RHS of Eq. (3.9) for transient is adopted. Namely, the time derivative component of the transient source is split between the right and left hand sides of Eq. (3.9) based on a condition that guarantees the source is non-negative.

To implement the splitting a slightly different, and more accurate approximation for the time derivative is used

$$\frac{\varphi_g^{n-1}(\mathbf{r},\boldsymbol{\Omega})}{v_g(\mathbf{r})\Delta t_n}-\Sigma_{split,g}^n(\mathbf{r})\varphi_g^n(\mathbf{r},\boldsymbol{\Omega})\approx\frac{\phi_g^{n-1}(\mathbf{r})}{v_g(\mathbf{r})\Delta t_n 4\pi}-\Sigma_{split,g}^n(\mathbf{r})\phi_g^n(\mathbf{r}), \tag{3.11}$$

where $\Sigma_{split,g}^n(\mathbf{r})$ is to be defined.

Thus the new transient fixed source problem with splitting is given by

$$\boldsymbol{\Omega}\cdot\nabla\varphi_g^n(\mathbf{r},\boldsymbol{\Omega})+\left[\Sigma_{t,g}^n(\mathbf{r})-\Sigma_{split,g}^n(\mathbf{r})+\frac{1}{\Delta t_n v_g}\right]\varphi_g^n(\mathbf{r},\boldsymbol{\Omega})=$$
$$S_{s,g}(\mathbf{r},\boldsymbol{\Omega})+\frac{\tilde{\chi}_g^n(\mathbf{r})}{4\pi k_{eff}}S_F^n(\mathbf{r},t)+S_{tr,g}^n(\mathbf{r})+\frac{\phi_g^{n-1}(\mathbf{r})}{v_g(\mathbf{r})\Delta t_n 4\pi}-\Sigma_{split,g}^n. \tag{3.12}$$

The condition to ensure the source is non-negative is applied to $\Sigma_{split,g}^n(\mathbf{r})$. This condition is

$$\Sigma_{split,g}^n=\min\left(\frac{1}{v_g(\mathbf{r})\Delta t_n},\frac{\phi_g^{n-1}(\mathbf{r})}{v_g(\mathbf{r})\Delta t_n\phi_g^n(\mathbf{r})}\right), \tag{3.13}$$

which guarantees that

$$S_{tr,g}^n(\mathbf{r})+\frac{\phi_g^{n-1}(\mathbf{r})}{v(\mathbf{r})\Delta t_n}-\Sigma_{split,g}^n(\mathbf{r})\geq 0. \tag{3.14}$$

The stability and robustness added by the transient source splitting is readily evident by examining the flux residual for the `4-mini_transient` regression test; shown in Figure 3.8 below.

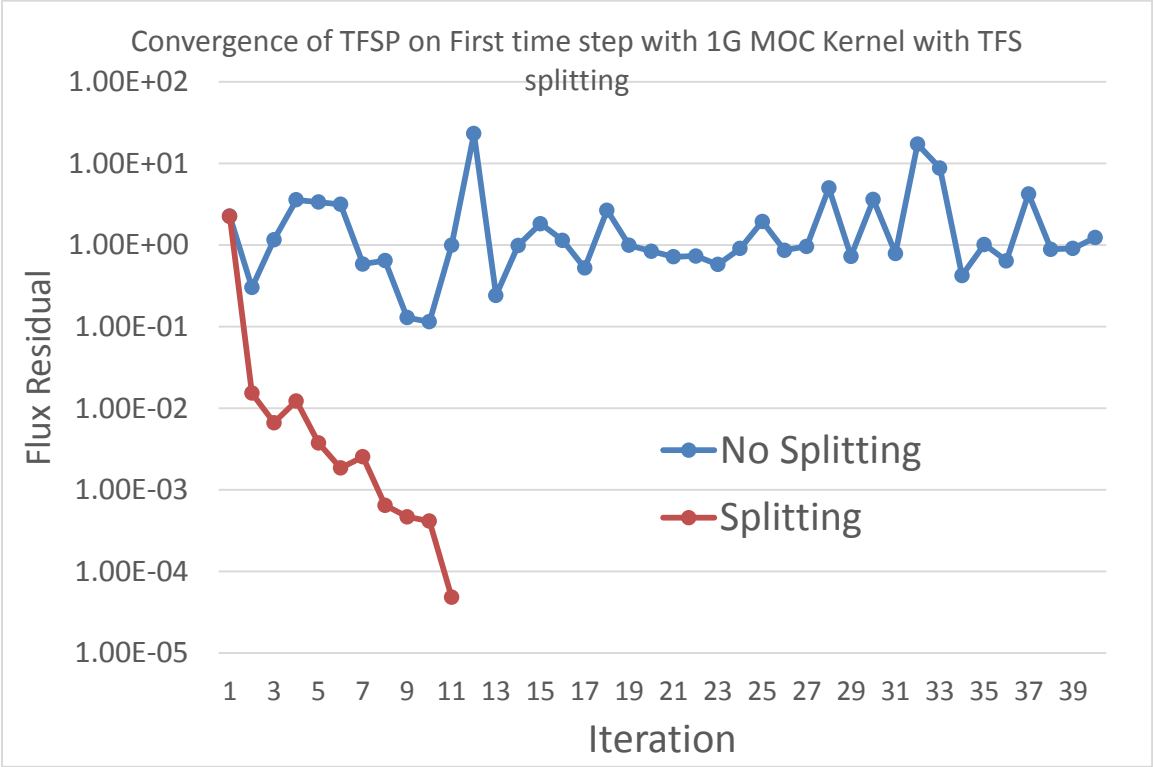

Figure 3.8: Stability gained from transient source splitting

3.4.2 Axial transverse leakage splitting for 2D/1D transients

Even with the transient source splitting some cases that were expected to run without issue were still not converging. After much debugging it was observed that during the iteration some of the total cross sections in the MOC fixed source problem were evaluating to huge numbers near infinity. With further investigation the root cause was determined to be related to how the axial transverse leakage splitting was being performed for the 2D MOC fixed source problem. The axial transverse leakage splitting is given by:

$$\boldsymbol{\Omega}\cdot\nabla\varphi_g^k(\mathbf{r},\boldsymbol{\Omega})+\left[\Sigma_{t,g}^k(\mathbf{r})-\Sigma_{TL,g}^k(\mathbf{r})\right]\varphi_g^k(\mathbf{r},\boldsymbol{\Omega})= S_{s,g}^k\phi_g^k(\mathbf{r})+\frac{\chi_g^k(\mathbf{r})}{4\pi k_{eff}}S_F^k(\mathbf{r})-\frac{L_{z,g}^k(\mathbf{r})}{\Delta z_k}-\Sigma_{TL,g}^k(\mathbf{r})\phi_g^k(\mathbf{r}). \tag{3.15}$$

$$\Sigma_{TL,g}^k(\mathbf{r})=\begin{cases}0 & S_{s,g}^k\phi_g^k(\mathbf{r})+\dfrac{\chi_g^k(\mathbf{r})}{4\pi k_{eff}}S_F^k(\mathbf{r})-\dfrac{L_{z,g}^k(\mathbf{r})}{\Delta z_k}\geq 0\\ \dfrac{S_{s,g}^k\phi_g^k(\mathbf{r})+\dfrac{\chi_g^k(\mathbf{r})}{4\pi k_{eff}}S_F^k(\mathbf{r})-\dfrac{L_{z,g}^k(\mathbf{r})}{\Delta z_k}}{\phi_g^k(\mathbf{r})} & S_{s,g}^k\phi_g^k(\mathbf{r})+\dfrac{\chi_g^k(\mathbf{r})}{4\pi k_{eff}}S_F^k(\mathbf{r})-\dfrac{L_{z,g}^k(\mathbf{r})}{\Delta z_k}<0\end{cases} \tag{3.16}$$

The logic for determining this was based on relation operations involving floating point numbers. For the transient problem, in some cases the scalar flux was evaluating to be effectively 0, but due to the nature of inexact arithmetic of floating point numbers, the resulting values were not exactly 0, but some very small positive number. This very small positive number is then divided into the total cross section on the left hand side leading to nearly infinite values for the total cross section.

To address this issue the relation operators were modified to perform “fuzzy” comparisons to account for the floating point number model.

With these changes for robustness, there have not been any further reports of problems in the convergence of the 2D/1D transient iteration even for complex real world models such as the AP1000 for which some results are shown in Section 4.4.

4. VERIFICATION, VALIDATION, AND DEMONSTRATION

4.1 C5G7-TD Numerical Benchmark

The C5G7 is a well established numerical benchmark which has been used to assess the accuracy of transport calculations without spatial homogenization [NEA 2005]. The C5G7 problem is based on a small reactor core with sixteen fuel assemblies: eight UO2 assemblies and eight MOX assemblies as shown in Figure 4.1.

Because the C5G7 is a very small reactor, ejecting a control rod with realistic cross sections would result in a very large reactivity insertion. Therefore, the control rod cross sections were adjusted such that a single control rod drive (CRD) would have more than 1$ reactivity. In addition, in order to simplify the modeling of the rod movement, the ejection of the rod was modeled as a step change in material composition. The control rod cluster was placed in a central UO2 assembly and the C5G7 transient was performed by ejecting only this rod from a full core geometry as illustrated in Figure 4.1.

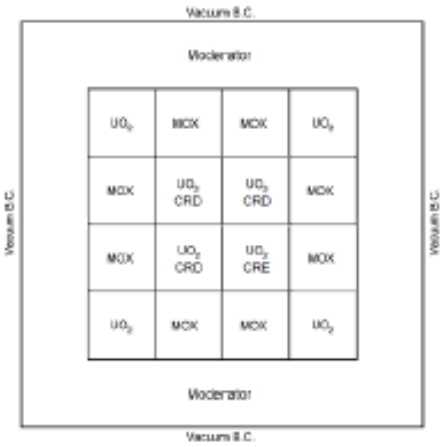

Figure 4.1 C5G7 with control rod drives (CRD) & ejected CRD (CRE)

The C5G7 transient begins from an assumed steady-state critical condition for which the eigenvalue was calculated to be 1.14802. The power distribution by fuel assembly for the C5G7 reactor at steady-state is depicted in the Figure which is color-coded by the magnitude of the power. Figure 4.2 shows the steady-state power distribution by fuel cell for the south-east quadrant of the reactor.

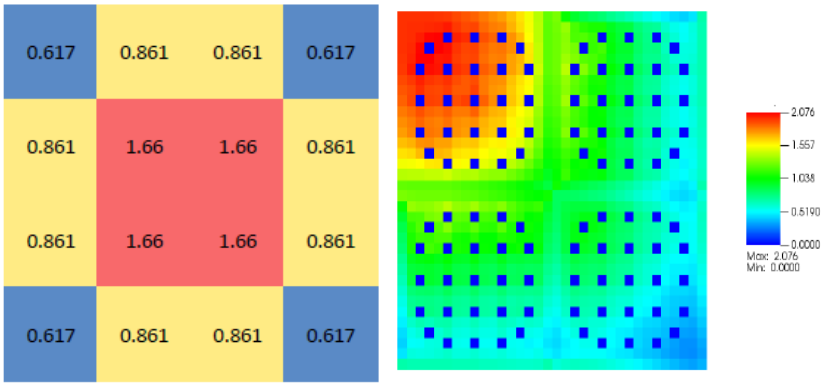

Figure 4.2 Steady-state relative power distribution

4.1.1 C5G7-TD Benchmark Model

C5G7-TD transient benchmark is based on the C5G7 benchmark model [Boyarinov, 2016] . The simulation of C5G7-TD was performed to continue the verification and validation of the transient capability in the MPACT code . Both 2D and 3D models were performed in the benchmark.

4.1.1.1 Geometry Description

In this section, geometry of the core will be specified. 2D model will be first introduced and then it will be derived into 3D model.

2D Model

The total model is a miniature light water core with 8 uranium oxide (UO_2) assemblies and 8 mixed oxide (MOX) assemblies. As of symmetry, the model can be simplified into a quarter of core having 4 assemblies, as shown in Figure 4.3. For convenience for assemblies are numbered into assembly 1~4 respectively as shown in Figure 4.4. The size of the 2D model is 64.26 cm×64.26 cm. The edge of the square shape assembly is 21.42 cm and the thickness of the moderator is 21.42 cm. The west and the north boundary uses vacuum boundary condition while the north and the east boundary, due to symmetry, take reflected boundary condition.

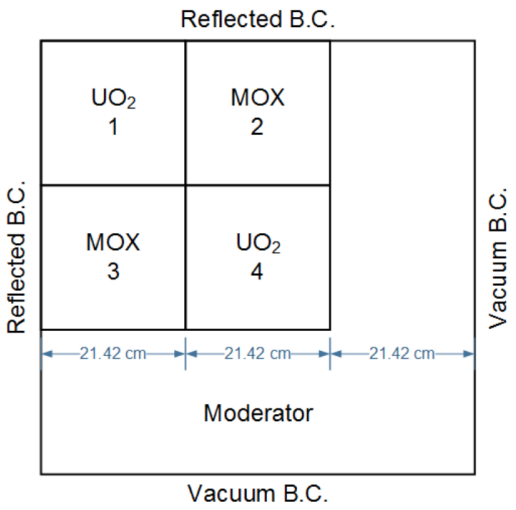

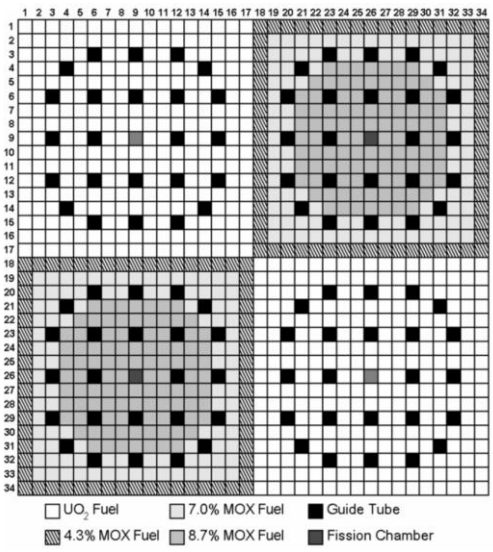

Figure 4.3 2D model of C5G7-TD benchmark Figure 4.4 2D model pin composition

The assemblies have the same geometry shape while the UO2 assemblies and MOX assemblies are same in materials respectively. For convenience they are numbered into assembly 1~4 as shown in Figure 2.1. Each assembly has a 17×17 configuration consisting 289 square cells: 264 fuel cell(UO_2 cell and MOX cell), 24 guide tube cells (represents a bank of control rods) and 1 fission chamber cell in the center as is shown in Figure 2.2. In the assembly of UO_2, there is only 1 kind of fuel, while in the assembly of MOX, there are 3 kinds of fuels with different enrichment: 4.3%, 7.0% and 8.7% respectively.

In each 17×17 grid assembly, the pitch is 1.26 cm and each square cell contains a pin: fuel pins for UO_2 and MOX cell, guide tube (with inside control rod or without control rod) for guide tube cells and instrument tube for fission chamber cell. To simplify the question the benchmark recommends that each cell shall have 2 zones as is shown in Figure 4.5: Zone 1 represent fuel pin, control rod or instrument tube in a certain cell and outside is Zone 2 which is filled with moderator. Zone 1 has the radius of 0.54 cm and is in the center of the cell.

Figure 4.5 Layout of 2D model cell

3D model

The 3D model shown in Figure 4.6 can be derived from the stated 2D model with ease. First stretch the 2D model in the axial direction to a length of 128.52 cm as the main part of the core. Then put 2 cuboid of moderator with the size of 64.26 cm×64.26 cm×21.42 cm on the top and on the bottom of the main part. Consequently, 3 parts make up he total core with a size of 64.26 cm×64.26cm×171.36 cm.

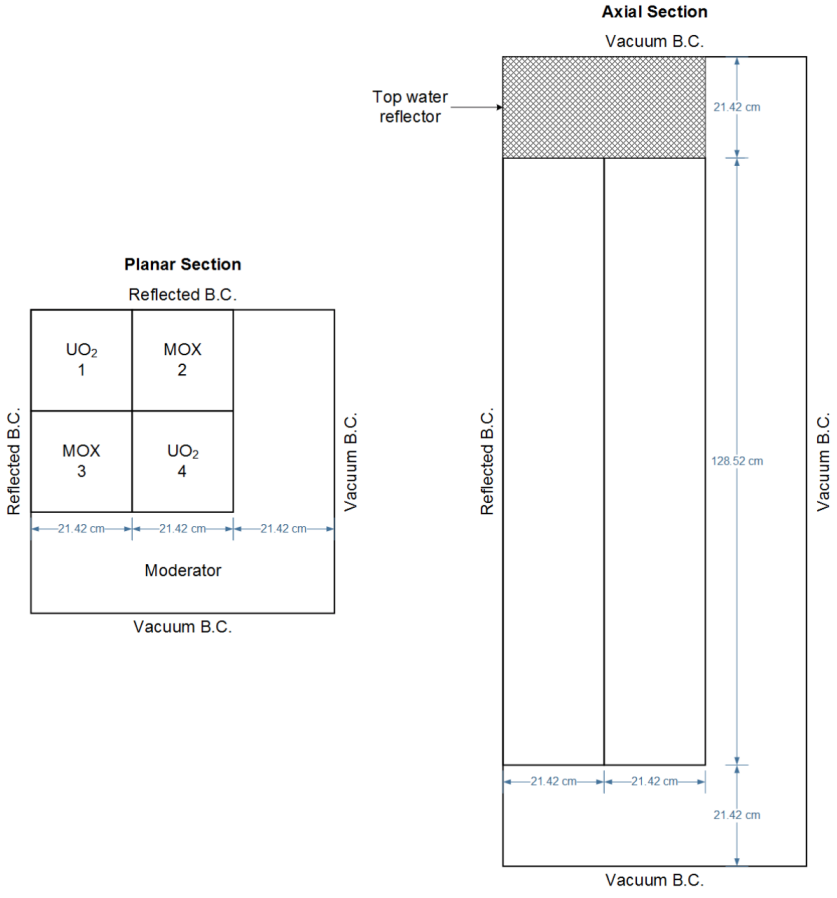

Figure 4.6 3D model of C5G7-TD benchmark

4.1.1.2 Material and Group Constant Description

Material Description

There are 8 basic materials in the benchmark: UO_2 fuel-clad, 4.3% MOX fuel-clad, 7.0% MOX fuel-clad, 8.7% MOX fuel-clad, fission chamber, guide tube, moderator and control rod. Their locations are listed in Table 4.2. Other kinds of material appear in the benchmark are either mixture of certain kinds of basic materials or materials same in composition as the basic ones but different in density, whose physics properties can be derived from the basic ones.

Table 4.2 Basic Materials in C5G7-TD benchmark

No.	Name	Location
1.	UO_2 fuel-clad	Zone 1 of UO_2 cells.
2.	4.3% MOX fuel-clad	Zone 1 of MOX cells (see in Figure 2.2).
3.	7.0% MOX fuel-clad	Zone 1 of MOX cells (see in Figure 2.2).
4.	8.7% MOX fuel-clad	Zone 1 of MOX cells (see in Figure 2.2).
5.	Fission Chamber	Zone 1 of fission chamber cell.
6.	Guide tube	Zone 1 of guide tube cell.
7.	Moderator	Zone 2 and moderator outside assemblies.
8.	Control rod	Zone 1 of guide tube cell, in the cases of inserting control rods.

Group Constant Description

The benchmark divides neutrons with different energy into seven groups. In the appendix of benchmark specification there are macroscopic cross sections and kinetic parameters containing transport cross sections, absorption cross sections, fission cross sections, average fission spectra (Chi), fission neutron yields (Nu) and 7×7scattering blocks. Other important parameters can be find, delayed neutron fractions, delayed neutron precursor decay constants, delayed neutron group data, neutron energy structure and neutron velocities can be find in the benchmark specification as necessary data of MPACT's input file or as reference.

4.1.2 Transient Descriptions

A total of 6 exercises were included in the C5G7 transient problems referred to as TD0, TD1, TD2, TD4, TD5. Each exercise contained several cases which were based on the either a 2D or 3D models and involved either an insertion/withdrawal of control rods or a density change of the moderator. Table 4.3 listed all these exercises.

Table 4.3 6 Exercises in C5G7-TD benchmark

Process / Dimension	Insertion/withdrawal of control rods	Change of moderator density
2D	TD0 (TD 0-1~TD 0-5)	TD3 (TD 3-1~TD 3-4)
	TD1 (TD 1-1~TD 1-5)	
	TD2 (TD 2-1~TD 2-3)	
3D	TD4 (TD 4-1~TD 4-5)	TD5 (TD5-1~TD5-4)

Control rods movement takes bank as unit, that is, control rods in the same bank will always in the same height and will move together. And change of density.

4.1.2.1 Exercise 0 (TD 0)

Exercise 0 is a 2D time-dependent benchmark with the process of insertion and withdrawal of control rods. At initial time the control rods insert abruptly into active core and the height of insertion is 10% active core height and stay for 1s. Then it extracted a half (remains 5% height of active core) abruptly and stay for a 1s. And at the end of 2s the control rods withdraw total out of active core. In the 2D model, this process is simulated as changing the cross section of zone 1 of control rod cells. It can be mathematically expressed as (1), (2) and (3) :

$$\sum_x(t) = \sum_x^{GT}, t = 0, t \geq 2s$$
$$\sum_x(t) = \sum_x^{GT} + 0.1(\sum_x^R - \sum_x^{GT}), 0 \leq t < 1s$$
$$\sum_x(t) = \sum_x^{GT} + 0.05(\sum_x^R - \sum_x^{GT}), 1s \leq t < 2s$$

$\sum$ refers to the seven-group macroscopic cross sections, the subscription *R* and *GT* refer to the domain of the control rod and guide tube, respectively. The subscription *x* is denoted as the reaction type, which includes absorption and scattering.

The process of TD 0 can be illustrated by Figure 4.7.

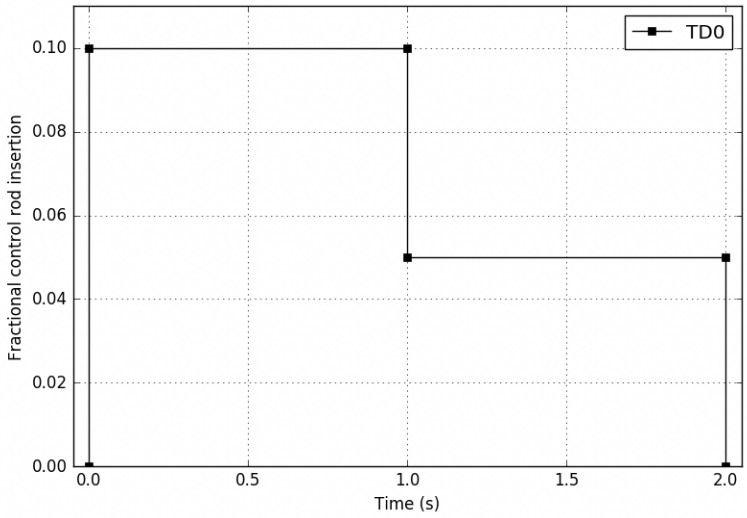

Figure 4.7 Insertion and withdrawal of control rods in TD 0

The difference of among 5 cases of TD 0 lays in the selection of bank of control rods that will move in the transient process that is listed in table 4.3.

Table 4.3 Control rod bank selections in TD 0

No.	Bank number
TD 0-1	1
TD 0-2	3
TD 0-3	4
TD 0-4	1, 3 and 4
TD 0-5	1, 2, 3 and 4

4.1.2.2 Exercise 1 (TD 1)

Exercise 1 is a 2D time-dependent benchmark with the process of insertion and withdrawal of control rods. In this exercise control rods move in a constant speed. At 0 s all control rods are out of the active core, and at the end of 1 s the depth of rods in the active core is 1% the height of active core. And then the rods withdraw with the same speed and come out of the active core at the end of 2 s. Still change of cross section is used to simulate this progress. This process can be mathematically expressed as (4), (5) and (6) and illustrated in Figure 4.8.

$$\sum_x(t) = \sum_x^{GT} + 0.01(\sum_x^R - \sum_x^{GT}), 0 \le t < 1s$$

$$\sum_x(t) = \sum_x^{GT} + 0.01(\sum_x^R - \sum_x^{GT})(2 - t), 1s \le t < 2s$$

$$\sum_x(t) = \sum_x^{GT}, t = 0, t \ge 2s$$

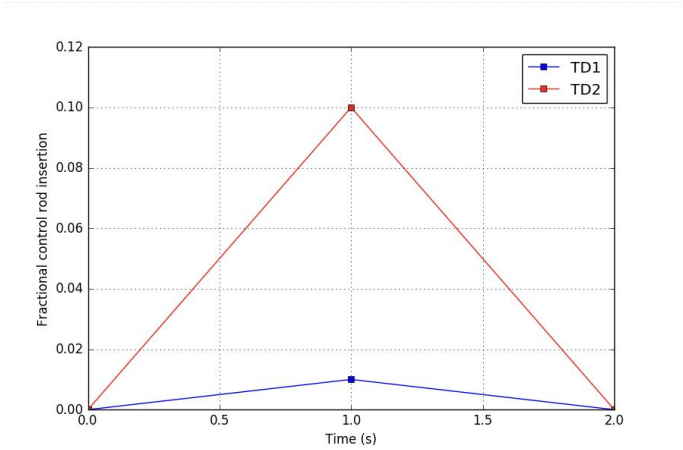

Figure 4.8 Insertion and withdrawal of control rods in TD 1 and TD 2

Still the difference of among 5 cases of TD 0 lays in the selection of bank of control rods to move.

Table 4.5 Control rod bank selections in TD 1

No.	Bank number
TD 1-1	1
TD 1-2	3
TD 1-3	4
TD 1-4	1, 3 and 4
TD 1-5	1, 2, 3 and 4

4.1.2.3 Exercise 2 (TD 2)

Exercise 2 is a 2D time-dependent benchmark with the process of insertion and withdrawal of control rods. In this exercise control rods move in a constant speed. The transient process in TD 2 is the same as TD 1 except that the depth of control rod insertion. At the end of 1 s, the depth is 10 % of active core, as is shown in Figure 4.9. This process can also be mathematically written as (7), (8) and (9).

$$\sum_x(t) = \sum_x^{GT} + 0.1(\sum_x^R - \sum_x^{GT}), 0 \le t < 1s$$

$$\sum_x(t) = \sum_x^{GT} + 0.1(\sum_x^R - \sum_x^{GT})(2 - t), 1s \le t < 2s$$

$$\sum_x(t) = \sum_x^{GT}, t = 0, t \ge 2s$$

TD 2 contains 3 problems listed in Table 3.3.

Table 4.9 Control rod bank selections in TD 2

No.	Bank number
TD 2-1	1
TD 2-2	3
TD 2-3	4

4.1.2.4 Exercise 3 (TD 3)

Exercise 3 is a 2D time-dependent benchmark with the process of density change of moderator. The moderator in the assemblies (but not the moderator outside of the assemblies) starts with normal density and decreases in density at a constant speed. At the end of 1 s, the density reaches its minimum of the initial density and the fraction is ω ($0 \leq \omega \leq 1$). Then the density increases in the same speed and reaches the initial value at the end of 2 s. For different cases in TD 3, ω takes to different fraction as is shown in Table 4.10. This process is illustrated in Figure 4.11.

Table 4.10 Minimum fractions of moderator(ω) in TD 3

No.	ω
TD 3-1	0.95
TD 3-2	0.90
TD 3-3	0.85
TD 3-4	0.80

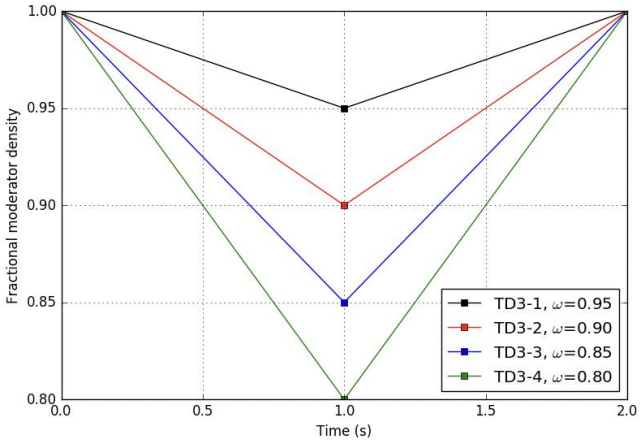

Figure 4.11 Process of moderator density change in TD 3

4.1.2.5 Exercise 4 (TD 4)

Exercise 4 is a 3D time-dependent benchmark with the process of insertion and withdrawal of control rods. The initial condition is that control rod banks and fission chambers are inserted into the upper water reflector. The speed of the insertion and withdrawal of the control rods is set as much as taking 6 s to fully insert in to assembly from fully withdrawn position. There are 5 cases in TD 4, among them the difference is still the choice of control rod banks. Cases are listed in Table 3.4 and processes are illustrated in Figure 4.12.

Table 4.7 Control rod bank selections in TD 4

No.	Bank number
TD 4-1	1
TD 4-2	3
TD 4-3	1 and 3
TD 4-4	3 and 4
TD 4-5	1 and 3

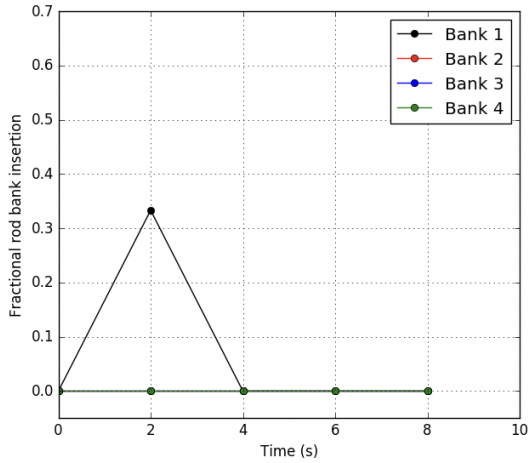

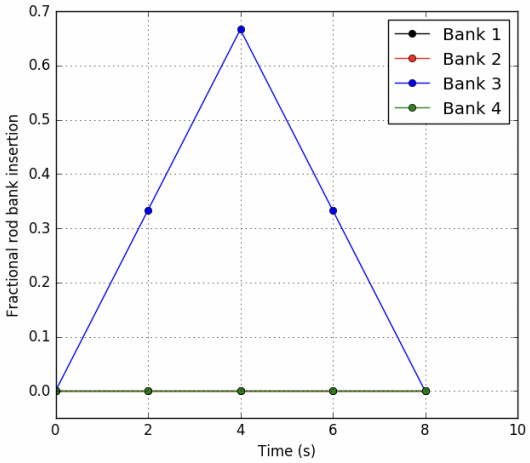

TD 4-1 TD 4-2

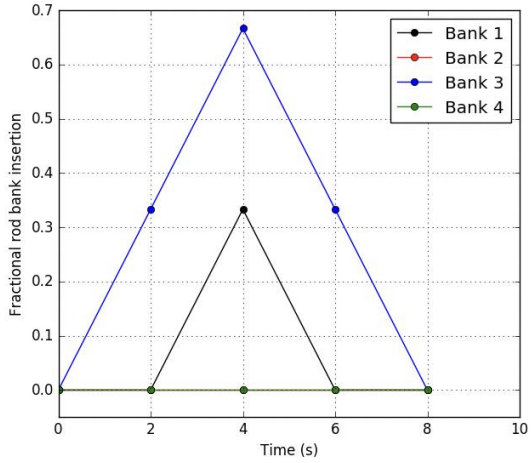

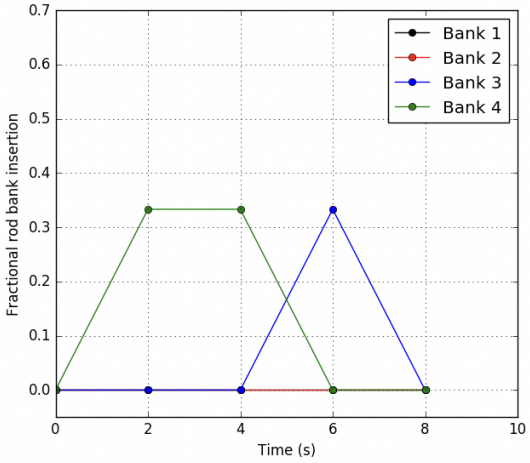

TD 4-3 TD 4-4

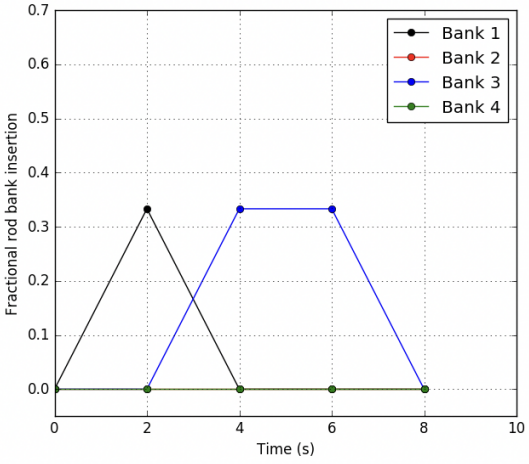

Figure 4.12 Insertion and withdrawal of control rods in TD 4

4.1.2.6 Exercise 5 (TD 5)

Exercise 3 is a 3D time-dependent benchmark with the process of density change of moderator. All control rods are positioned the fully withdrawn position at 0 s. Among the 4 cases moderator of different assemblies changes in density differently. This process is listed in Table 4.8 and illustrated in Figure 4.13. Note that in the figure of TD 5-2, moderator in assembly 2 and assembly are always same in density.

Table 4.8 Assemblies in which moderator density changes in TD 5

No.	Bank number
TD 5-1	1 and 3
TD 5-2	1, 2 and 3
TD 5-3	1, 3 and 4
TD 5-4	2, 3 and 4

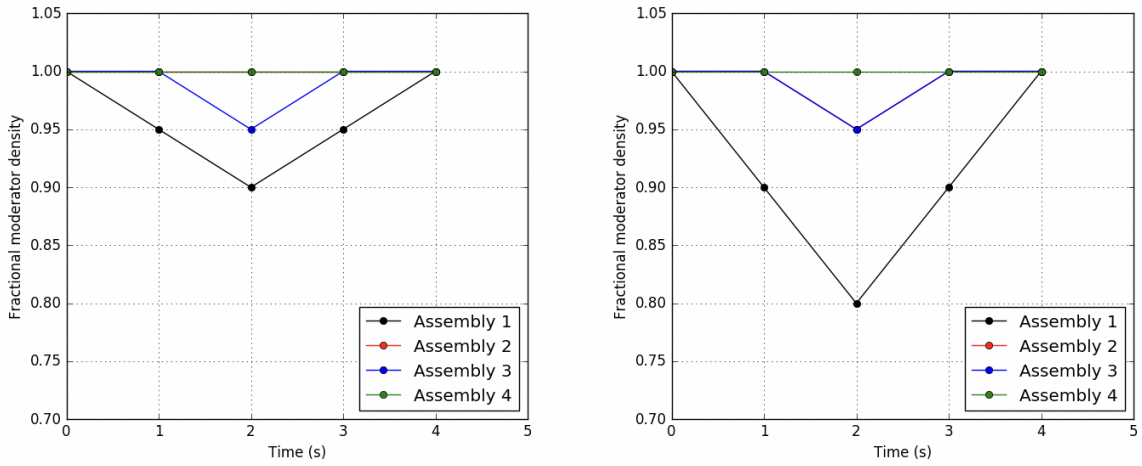

TD 5-1 TD 5-2

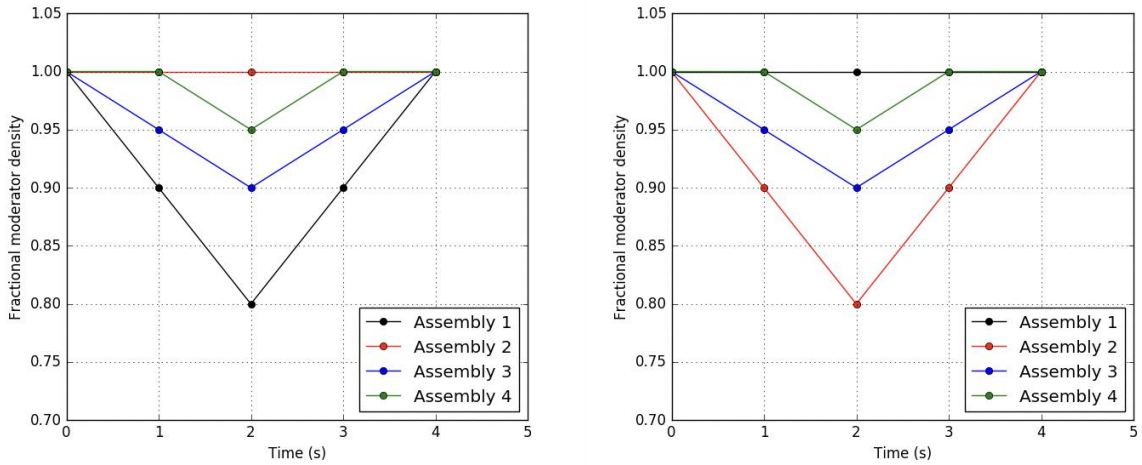

TD 5-3 TD 5-4

Figure 4.13 Process of moderator density change in TD 3

4.1.3 Simulation Results and Comparisons

Simulate all the stated cases from the 6 exercises (TD 0~TD 5). In the simulation of 2D cases, time step is set to be 0.01 s while in the 3D cases it is 0.02 instead. Now the available results contain power, delayed neutron fracture and reactivity (in the unit of $) with each time step in any case.

4.1.3.1 Power Fraction

Figure 4.14~Figure 4.19 gives the fraction of power at each time step divided by the initial power.

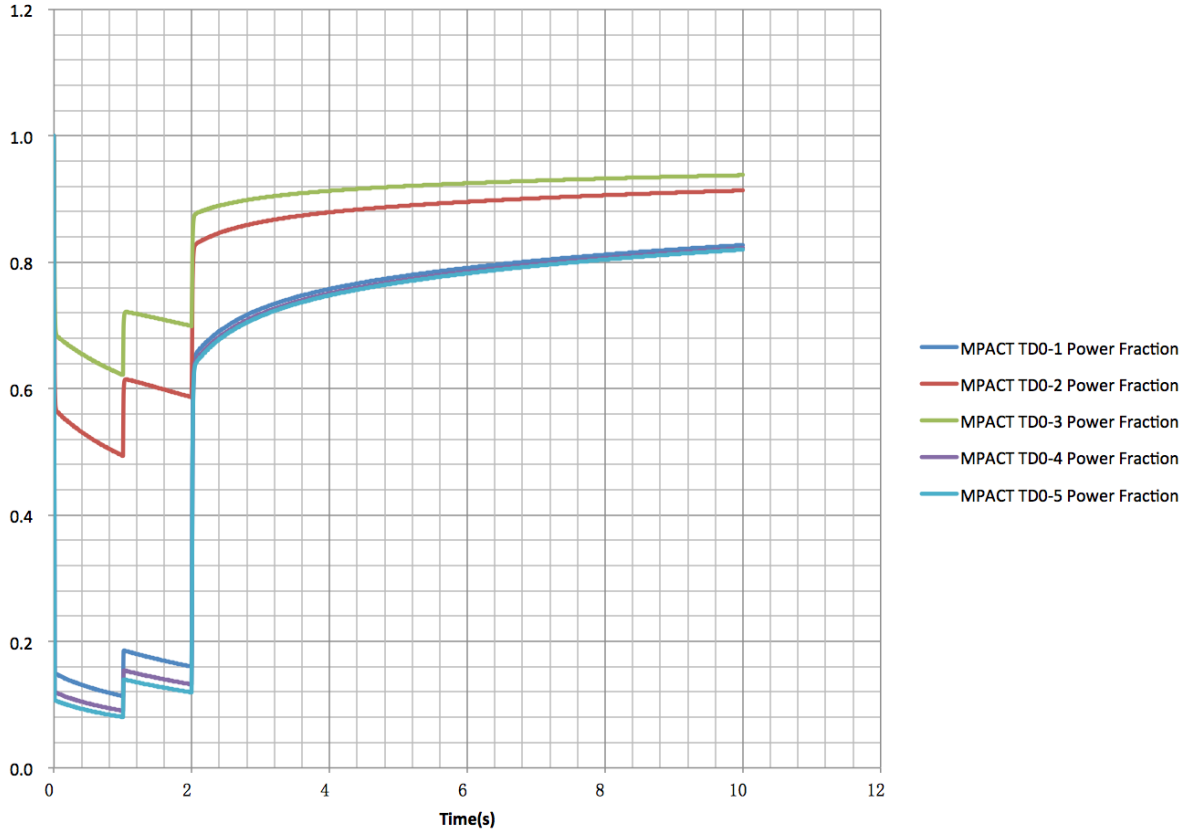

Figure 4.14 Power fraction of TD 0

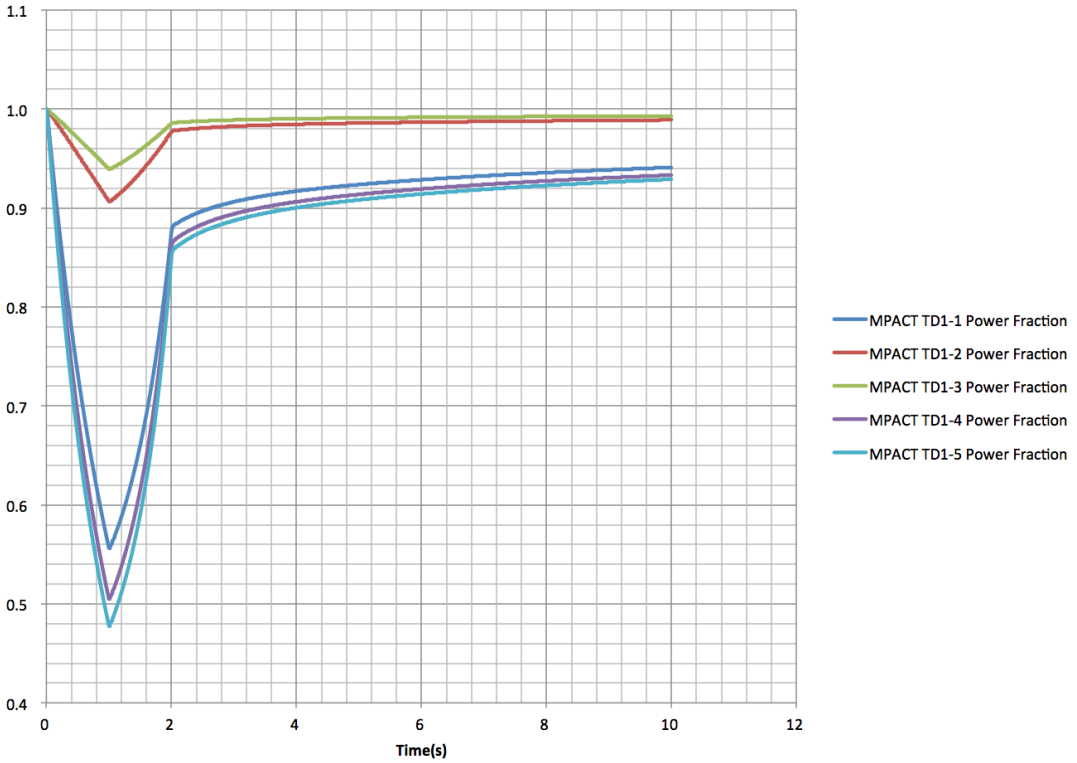

Figure 4.15 Power fraction of TD 1

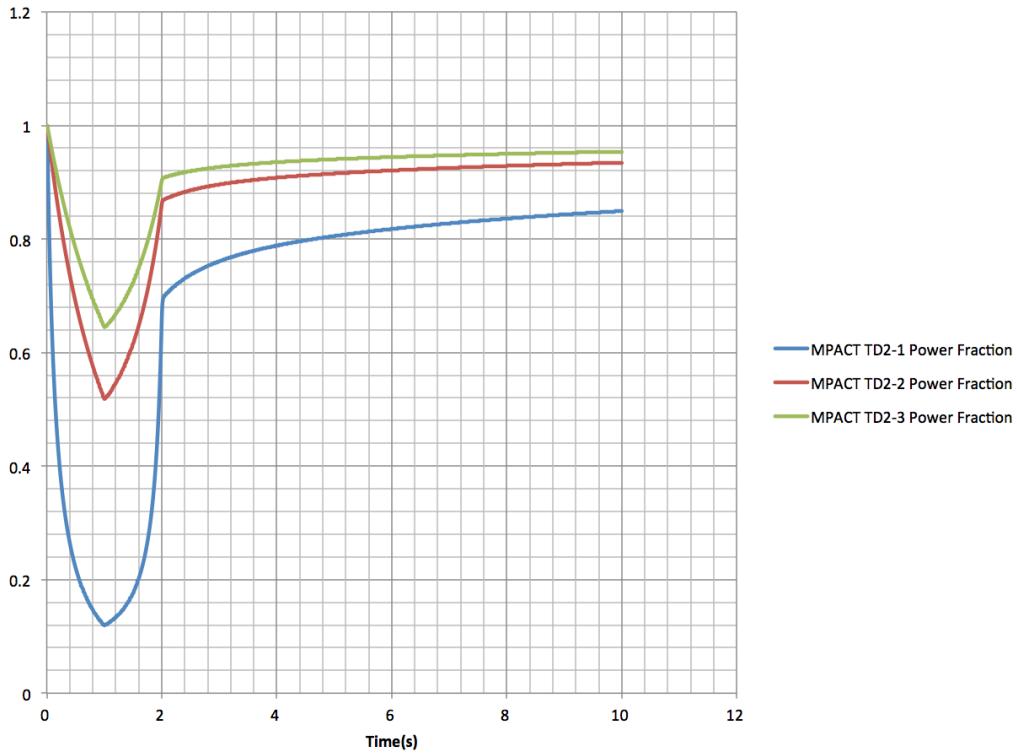

Figure 4.16 Power fraction of TD 2

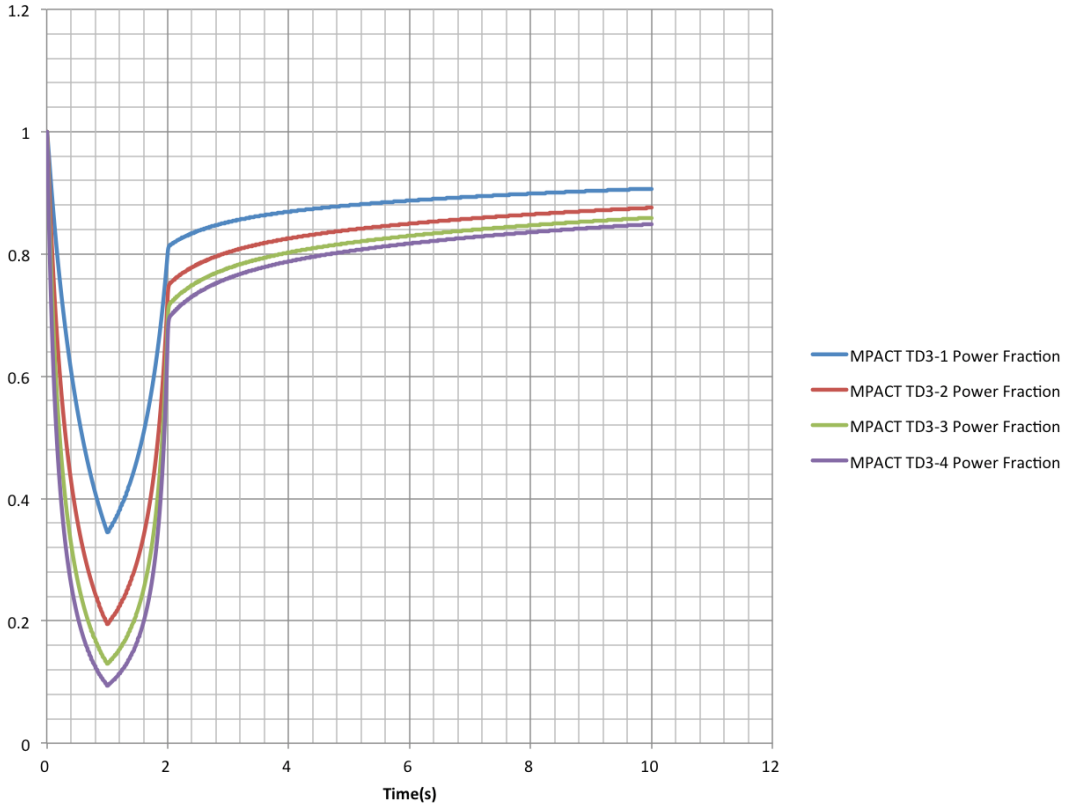

Figure 4.17 Power fraction of TD 3

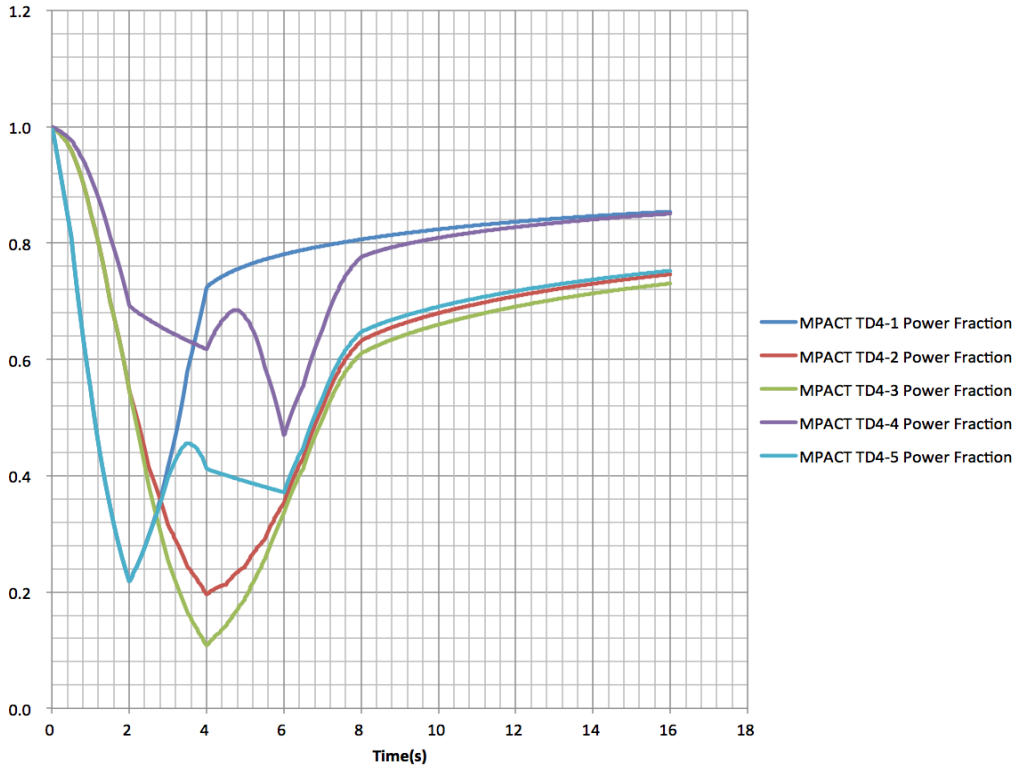

Figure 4.18 Power fraction of TD 4

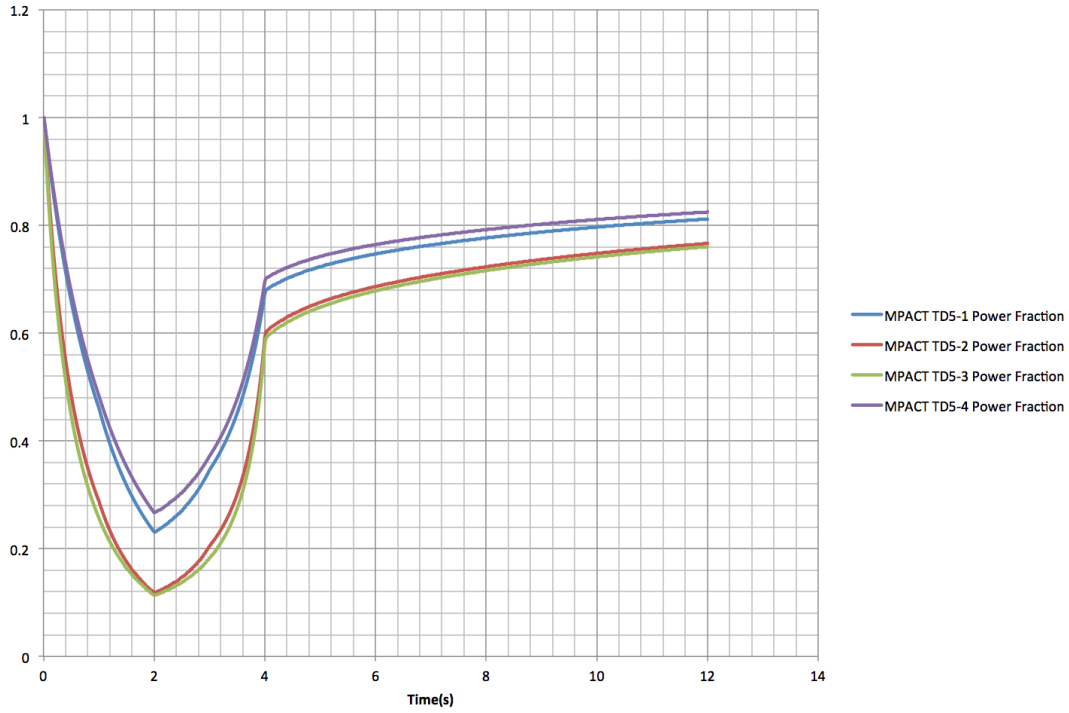

Figure 4.19 Power fraction of TD 5

The reference from results of the power fraction of TD 1, TD2 and TD 3 relative power deviation per step can be determined with the expression:

$$\Delta(t) = \frac{P_M(t) - P_R(t)}{P_R(t)} \times 100\%$$

$P_M(t)$ indicates power fraction of MPACT results at the time step of t, $P_R(t)$ indicates power fraction of the reference results at the time of t, $\Delta(t)$ indicates power fraction at the time of t.

Figure 4.20~4.22 illustrate $\Delta(t)$ of TD 1, TD 2 and TD 3 respectively.

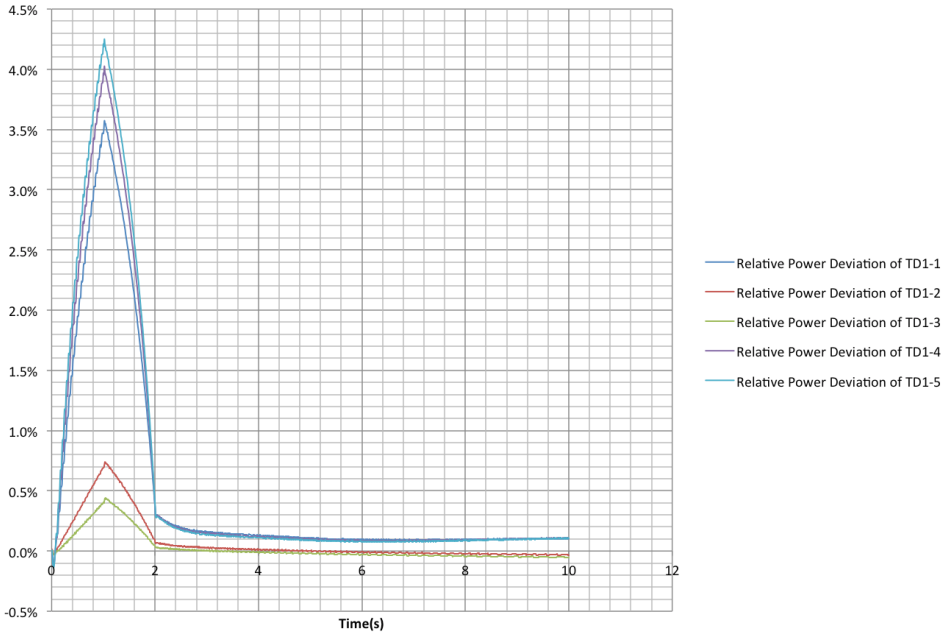

Figure 4.20 Relative power deviation of TD 1.

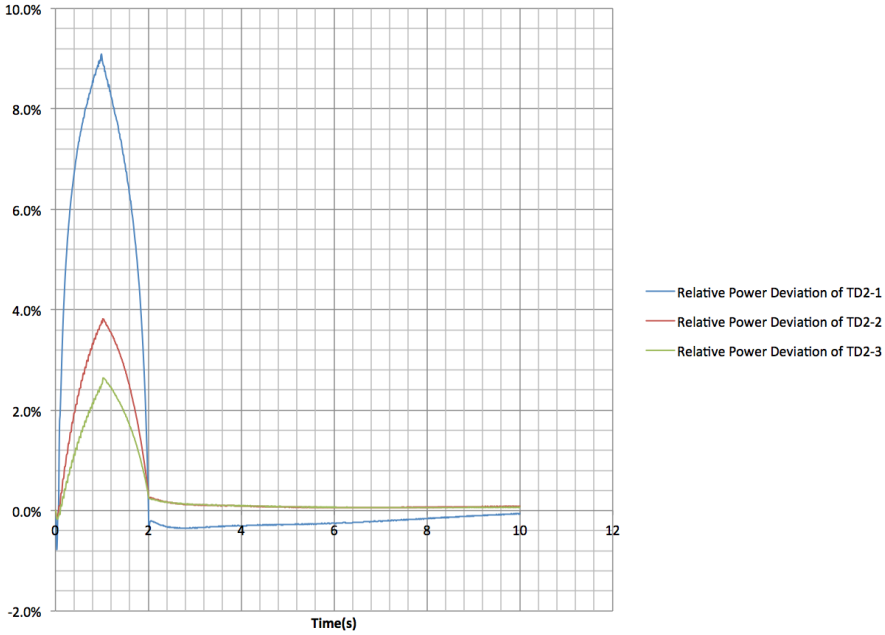

Figure 4.21 Relative power deviation of TD 2.

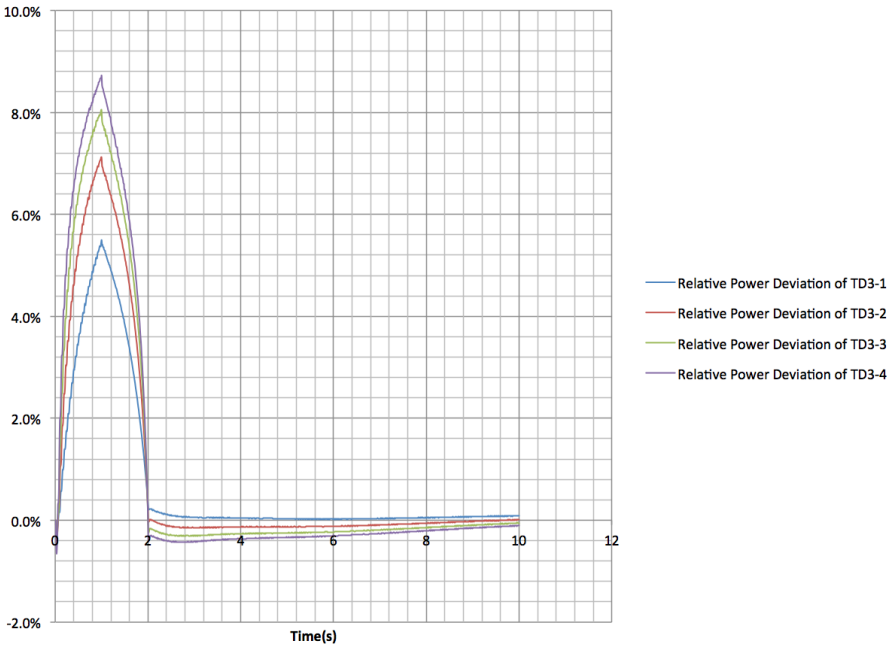

Figure 4.22 Relative power deviation of TD 3.

As indicated in the Figures, the maximum relative deviation between MPACT results and the reference results of TD 1,TD 2 and TD3 are below 5%, 10% and 9%, respectively which indicates overall very good agreement.

4.1.3.2 Reactivity

MPACT gives reactivity of any case per time step. Reactivity in the unit of dollar($) is shows in Figure 4.23~Figure 4.28.

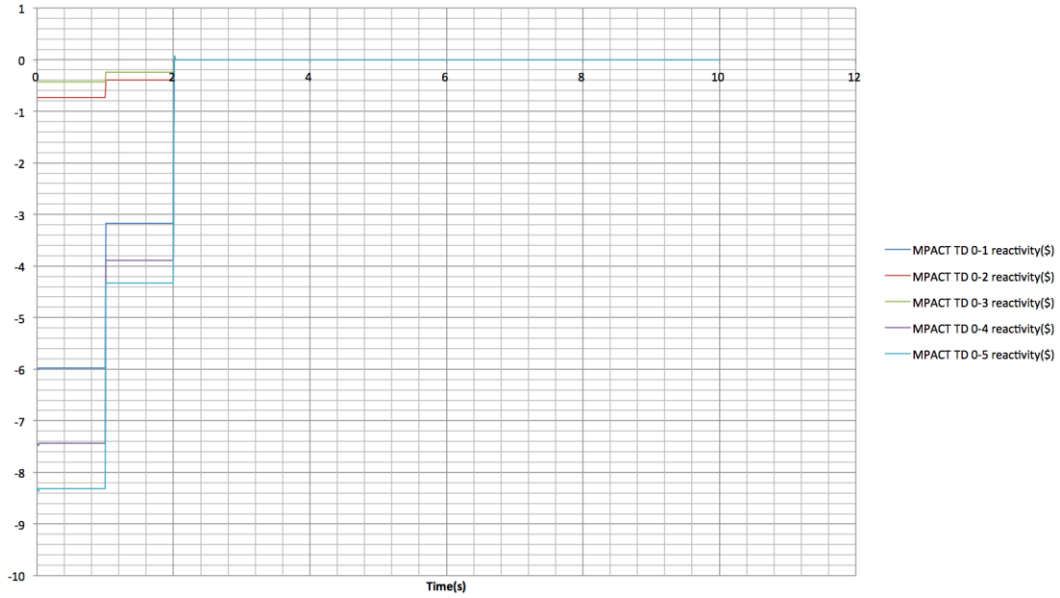

Figure 4.23 Reactivity of TD 0.

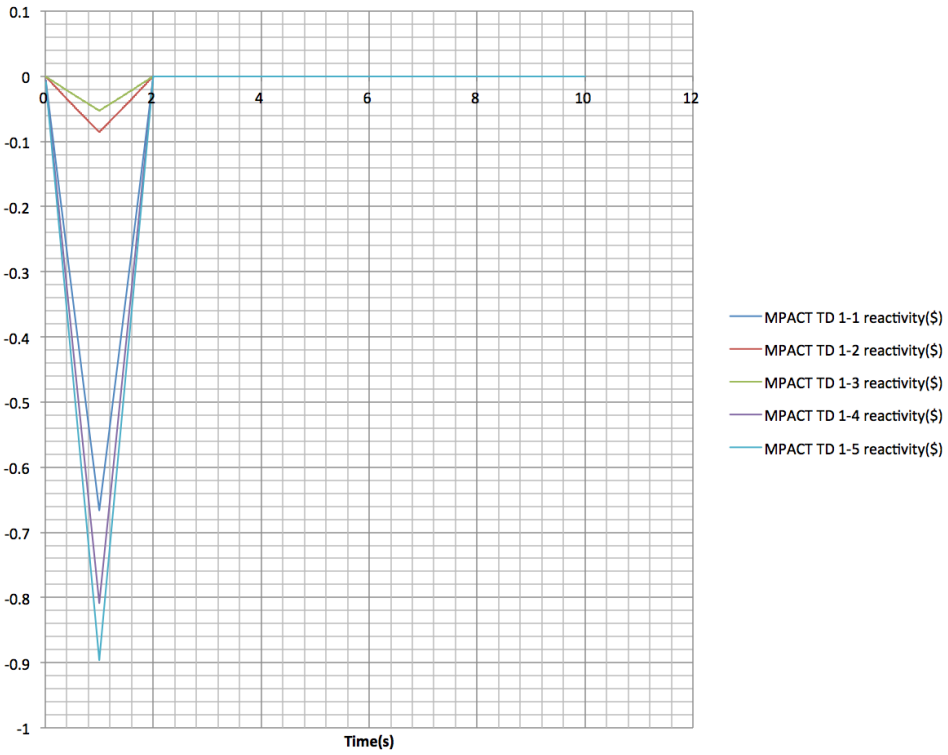

Figure 4.24 Reactivity of TD 1.

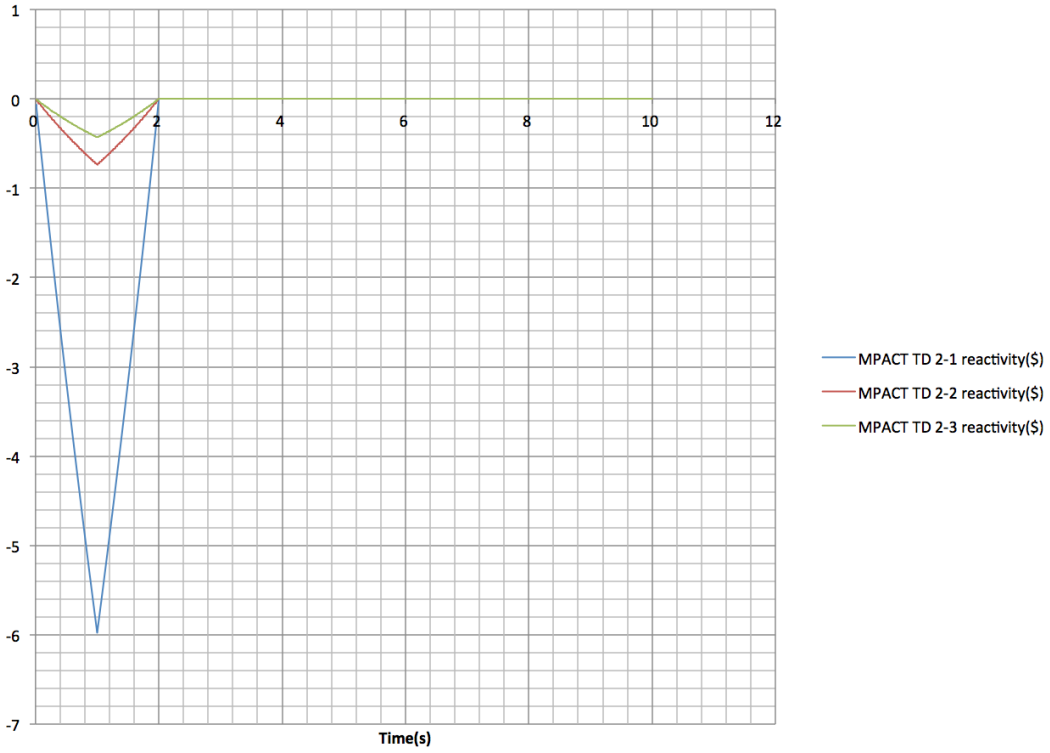

Figure 4.25 Reactivity of TD 2.

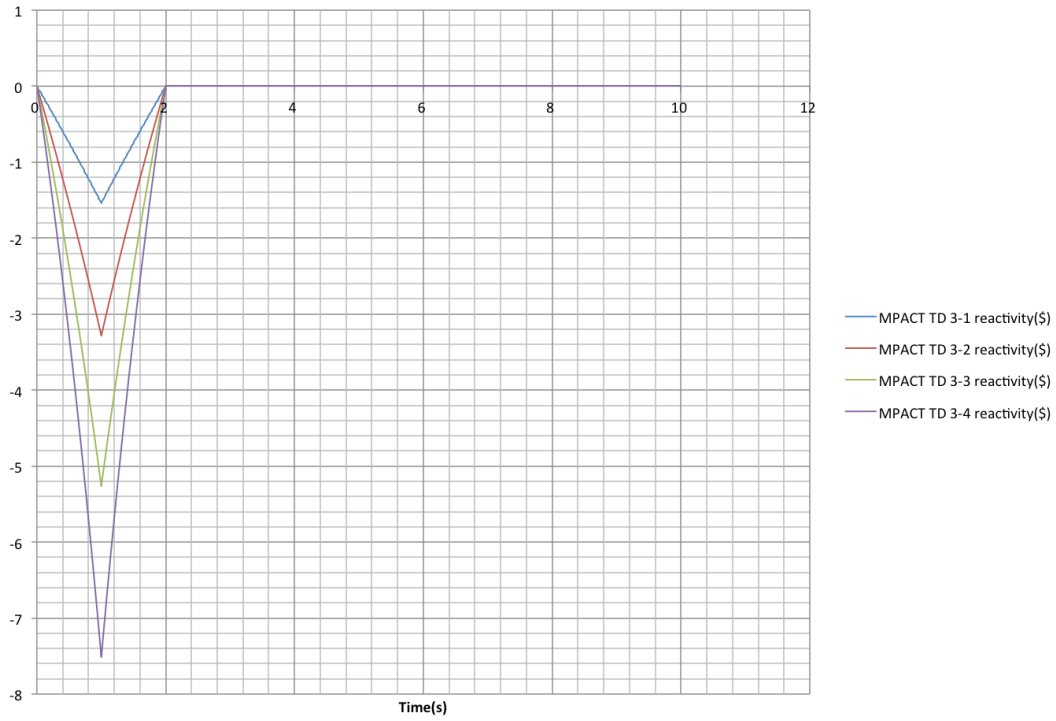

Figure 4.26 Reactivity of TD 3.

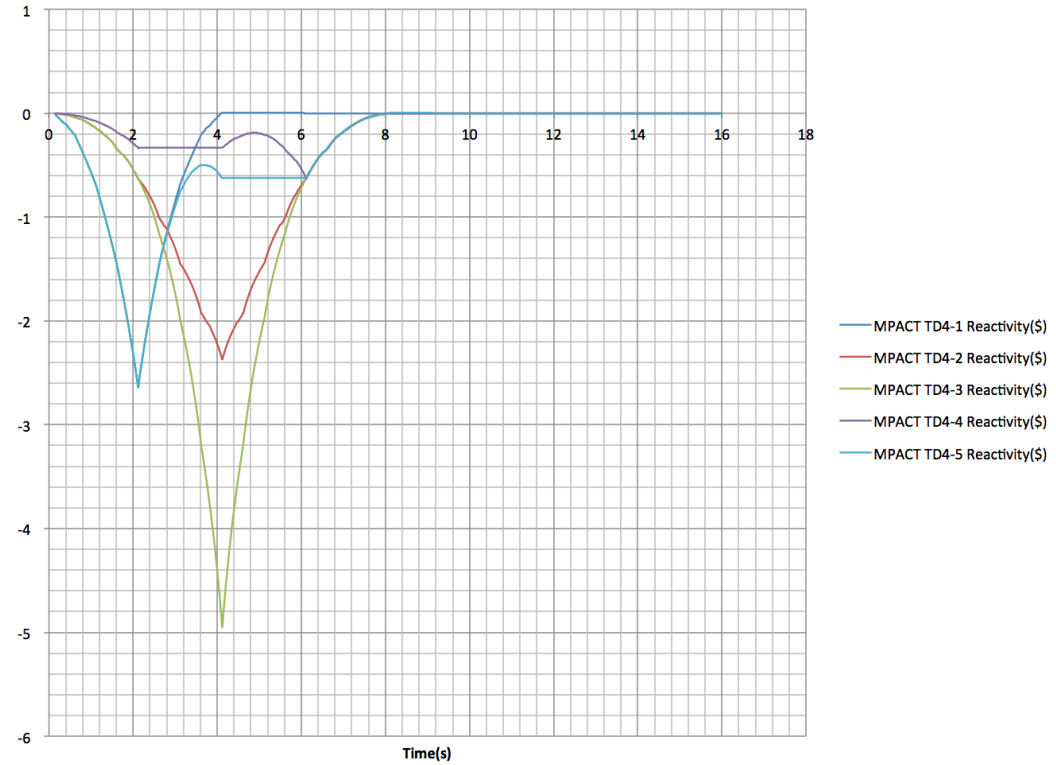

Figure 4.27 Reactivity of TD 4.

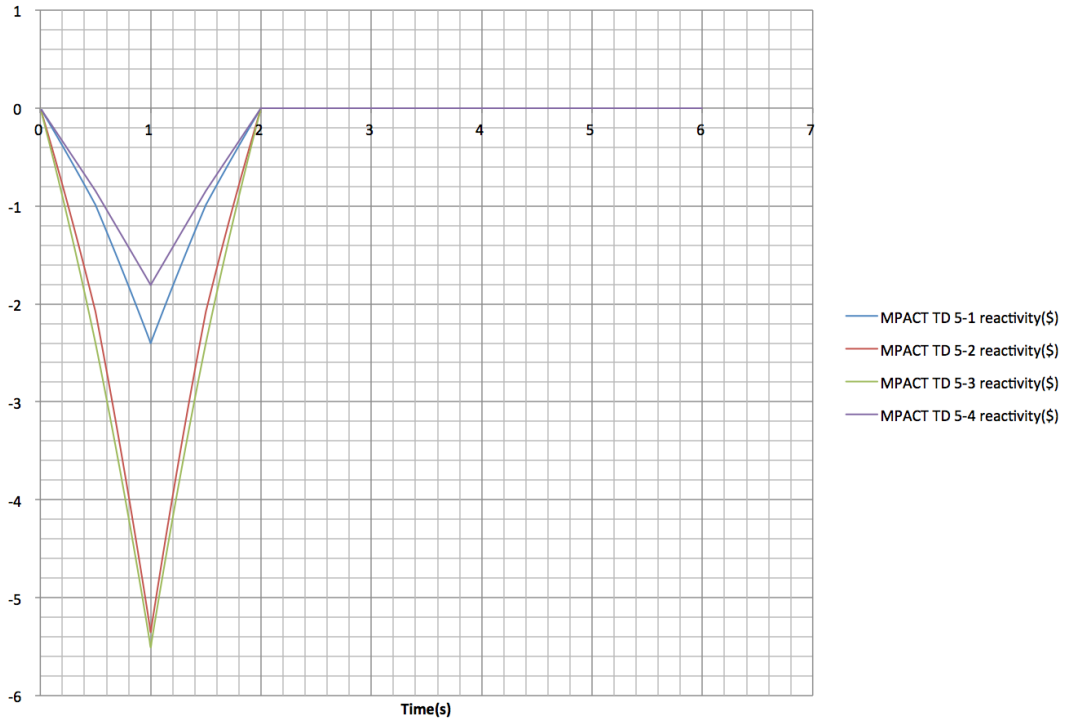

Figure 4.28 Reactivity of TD 5.

4.1.4 Detailed Comparisons of Results

Several reactor simulation softs take part in the benchmark and give the calculation results. The following subsections will take the 2D case TD1 and 3D case TD4 as examples to make comparison between results from different soft wares.

4.1.4.1 Comparison of TD1

TD 1 contains 5 cases of 2D insertion/withdrawal if control rod. Figure 4.29~Figure 4.33 are the power fraction results of TD1-1~TD1-5 respectively from different soft wares and different results have good agreement.

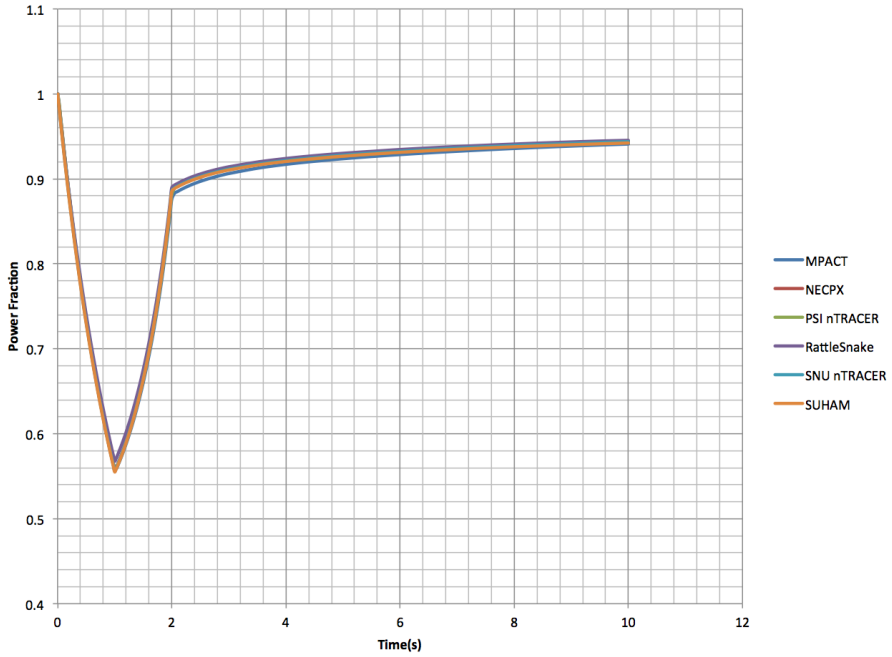

Figure 4.29 TD1-1 power fraction results from different simulation soft wares.

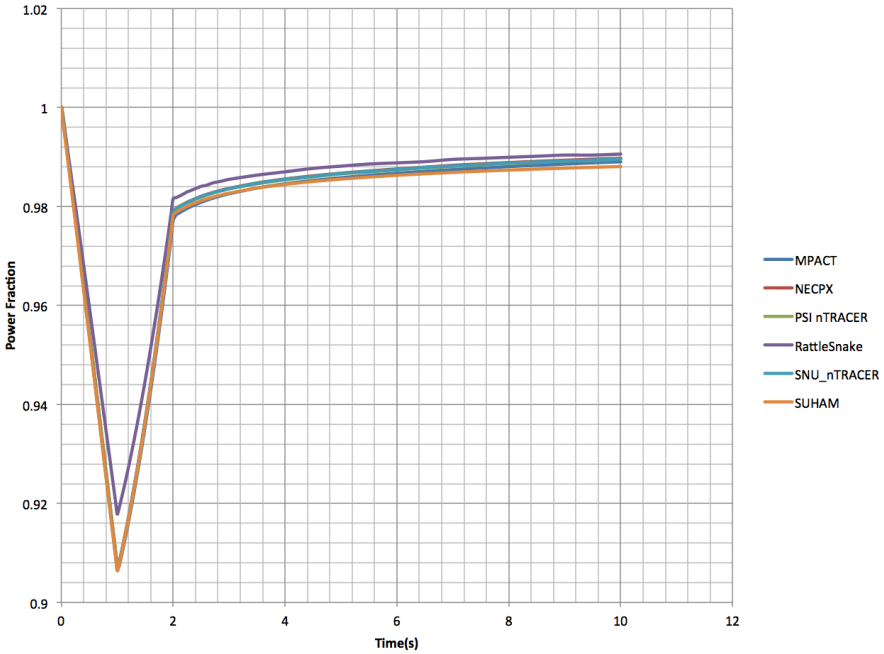

Figure 4.30 TD1-2 power fraction results from different simulation soft wares.

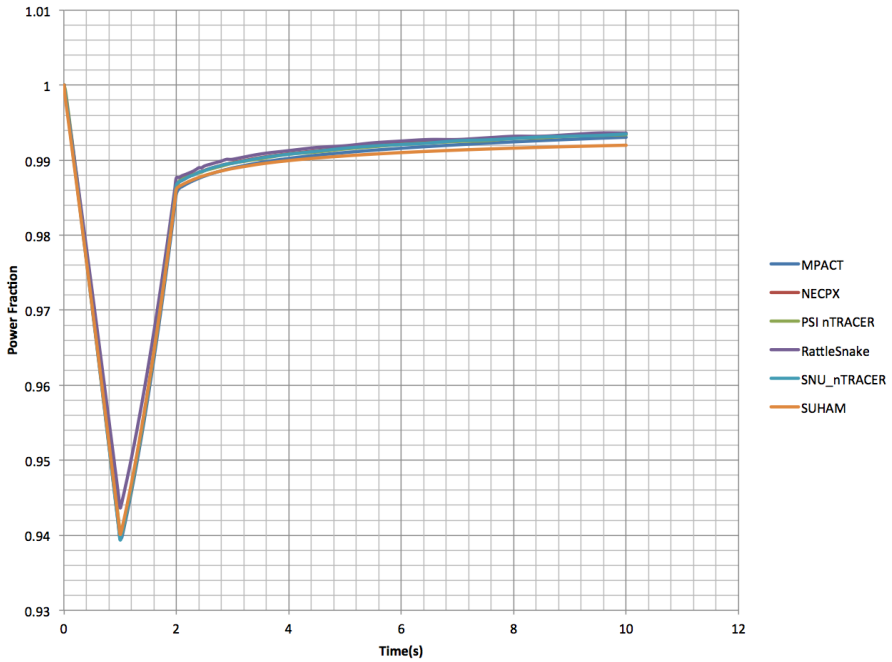

Figure 4.31 TD1-3 power fraction results from different simulation soft wares.

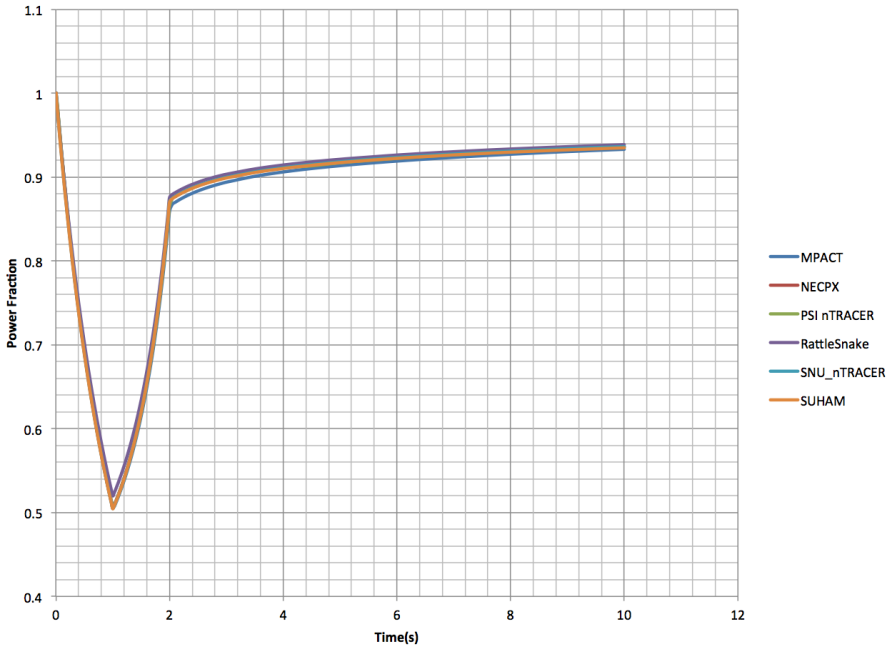

Figure 4.32 TD1-4 power fraction results from different simulation soft wares.

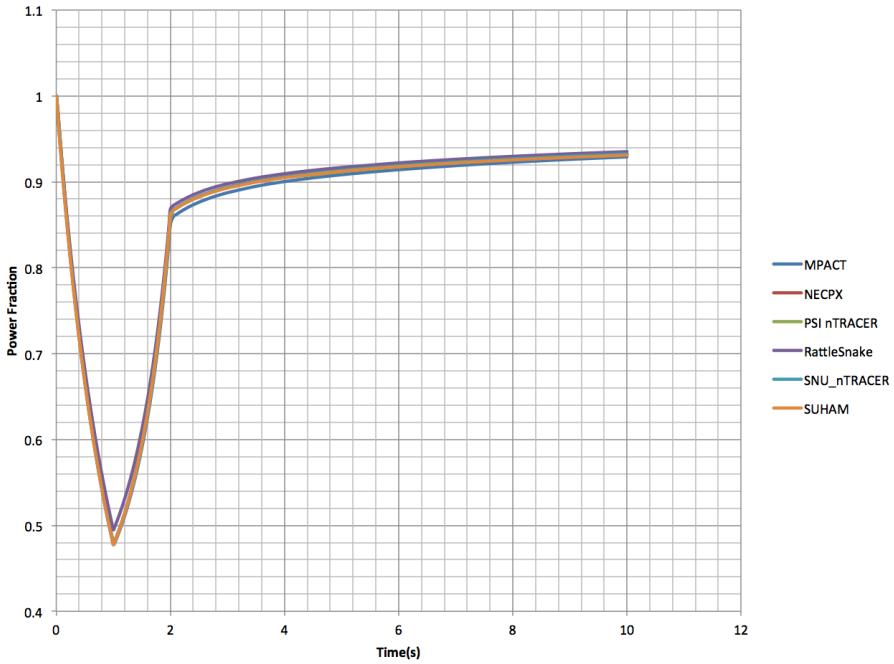

Figure 4.33 TD1-5 power fraction results from different simulation soft wares.

Because the simulation results have such good agreement, there is virtual overlap of the results. Using the MPACT results as a reference and defining the relative deviation of the power by the expression:

$$\Delta(t) = \frac{P_O(t) - P_M(t)}{P_M(t)} \times 100\%$$

In which $P_M(t)$ indicates the power fraction of MPACT results at the time step of t, $P_O(t)$ indicates power fraction of the results from other codes at the time of t, and $\Delta(t)$ indicates the power relative deviation at the time of t.

Figure 4.34~Figure 4.38 are the relative power fraction results of TD1-1~TD1-5, respectively. The figures show that the power relative deviation between MPACT and all other soft wares except the RattleSnake code is less than 1.0%, which prove the good agreement.

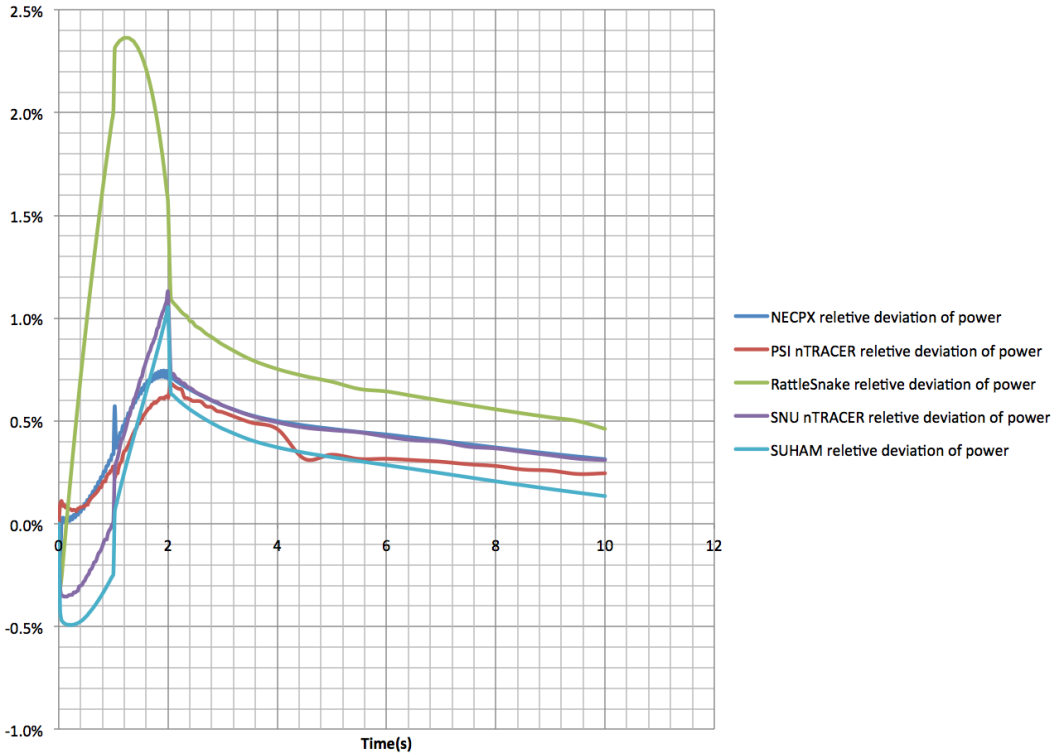

Figure 4.34 TD1-1 power relative deviation.

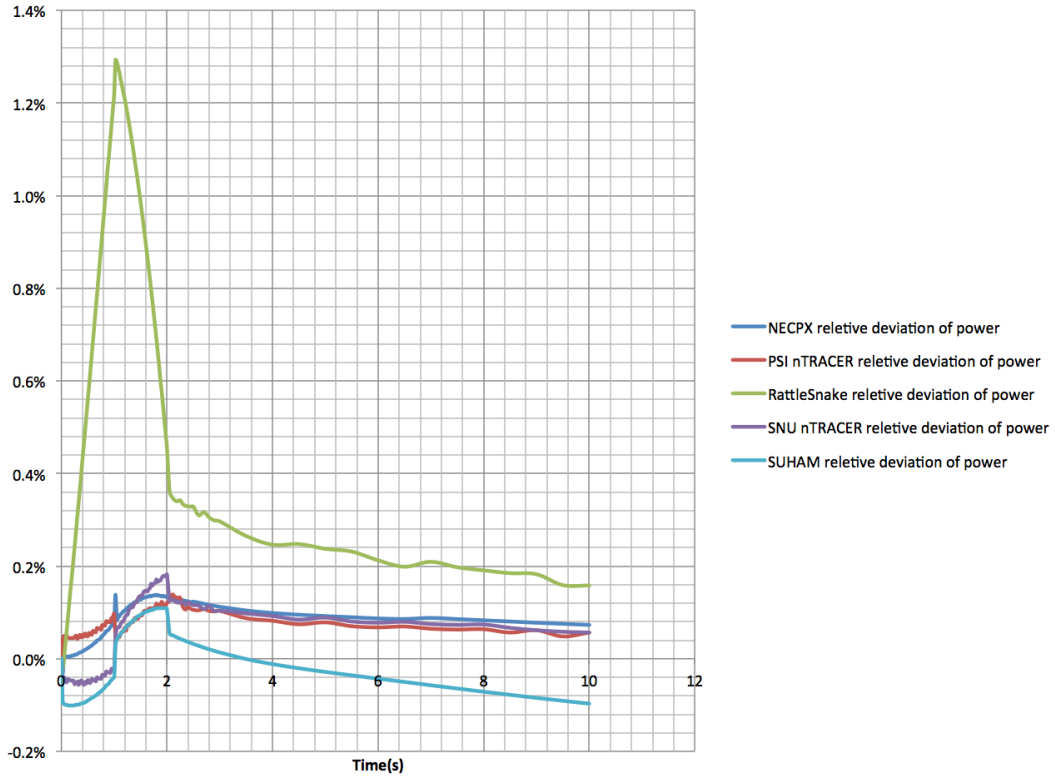

Figure 4.35 TD1-2 power relative deviation.

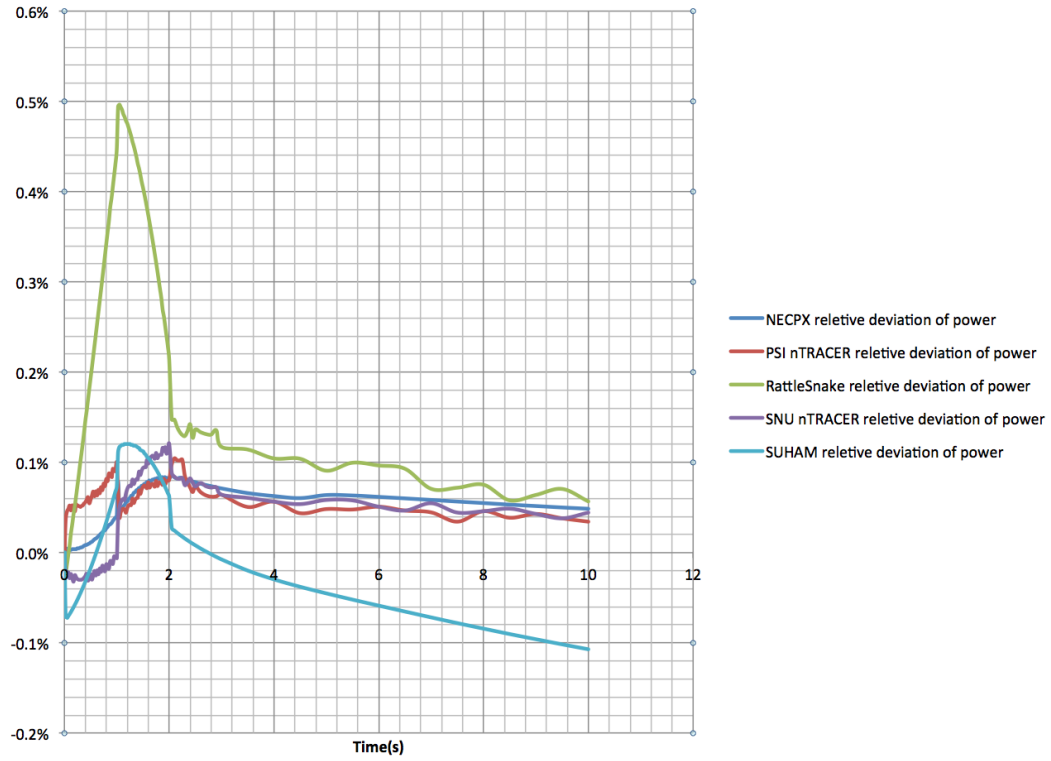

Figure 4.36 TD1-3 power relative deviation.

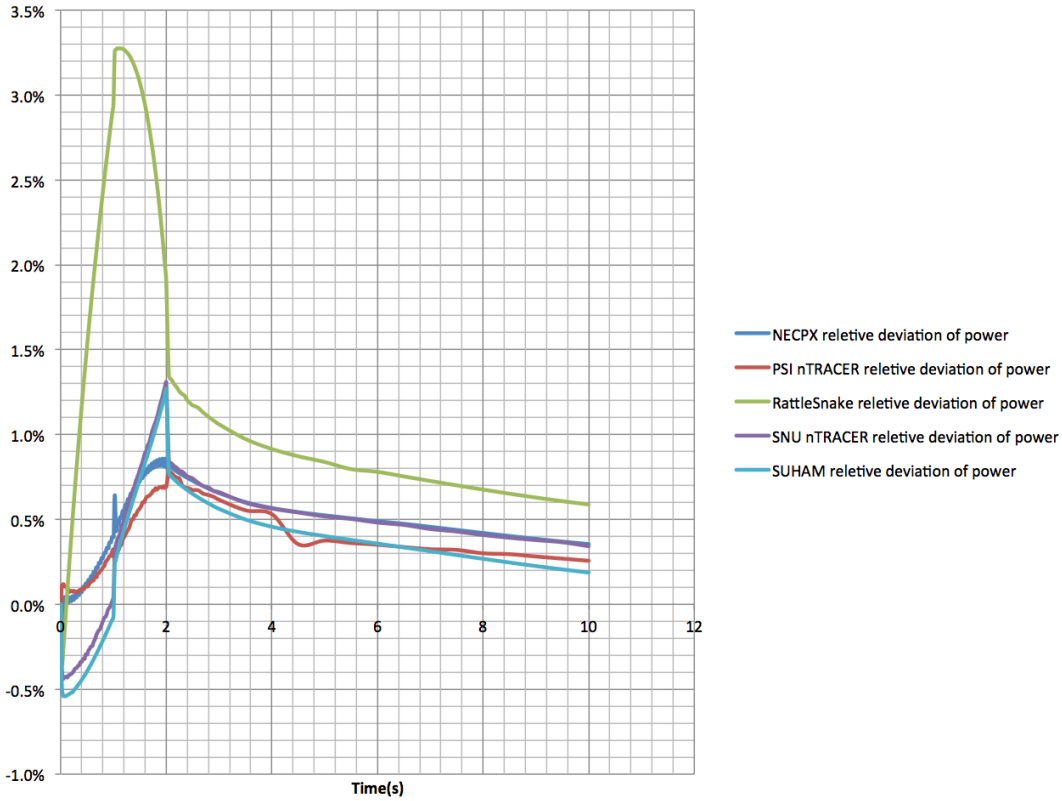

Figure 4.37 TD1-4 power relative deviation.

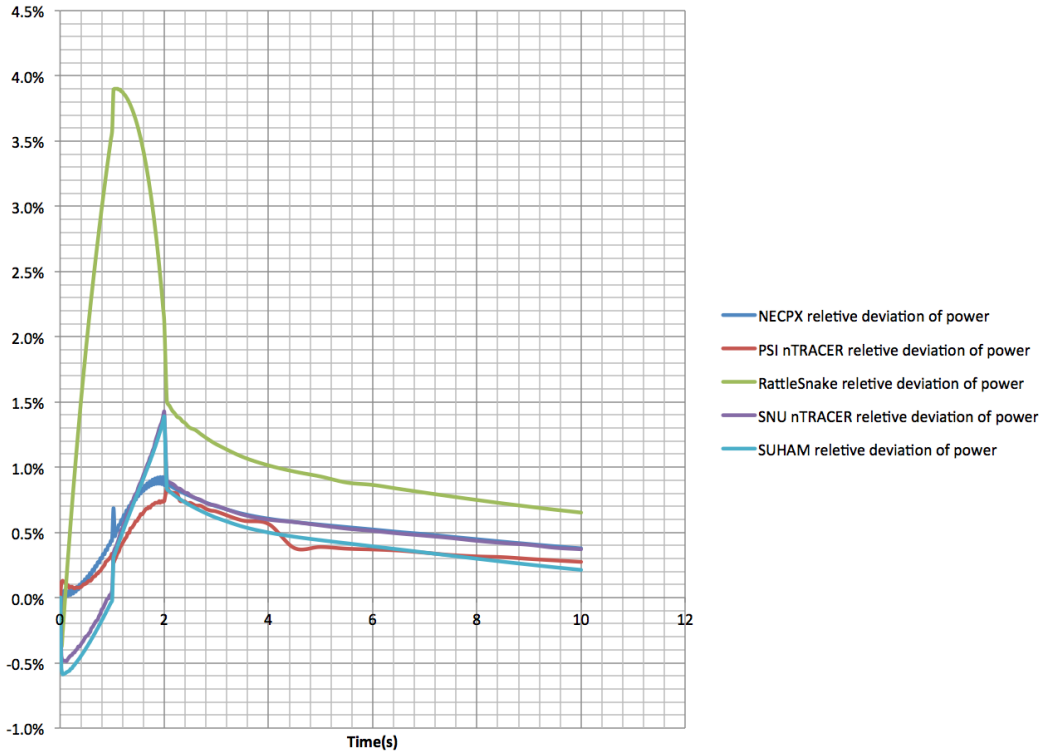

Figure 4.38 TD1-5 power relative deviation.

4.1.4.2 Comparison of TD4

Benchmark exercise TD 4 contains 5 cases of 3D insertion/withdrawal if control rod. Figure 4.39~Figure 4.43 are the power fraction results of TD4-1~TD4-5 respectively from the codes MPACT and PSI nTRACER.

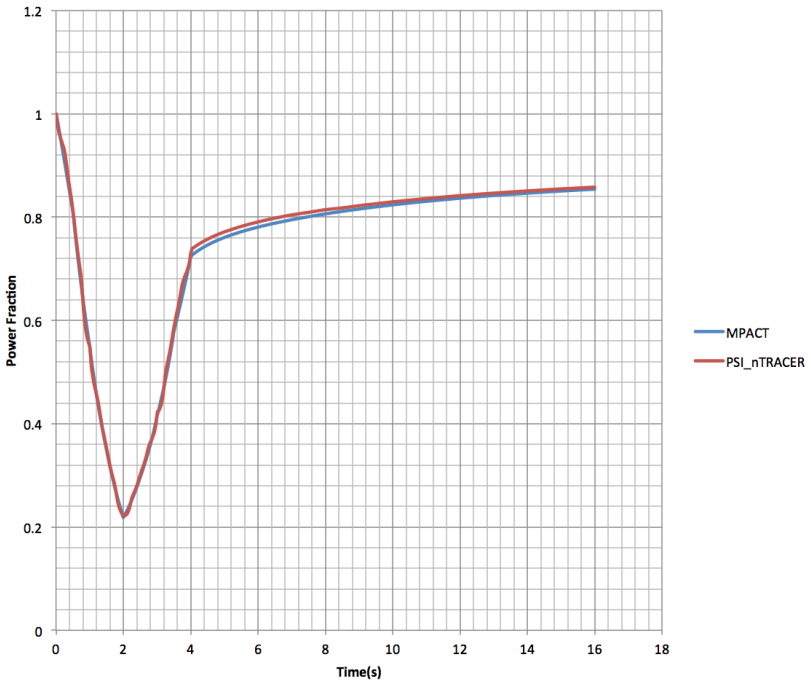

Figure 4.39 TD4-1 power fraction results from different simulation soft wares.

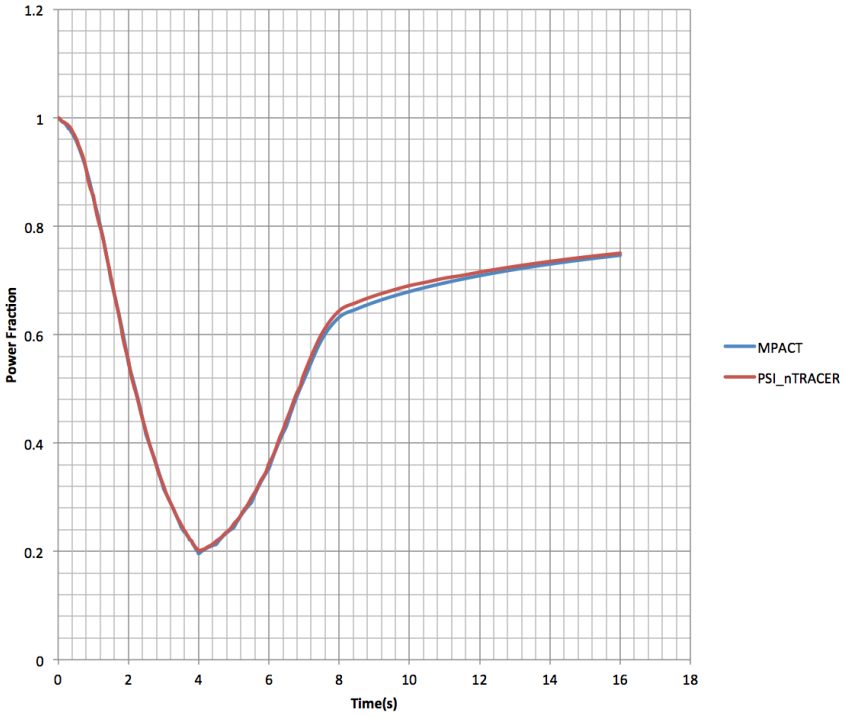

Figure 4.40 TD 4-2 power fraction results from different simulation soft wares.

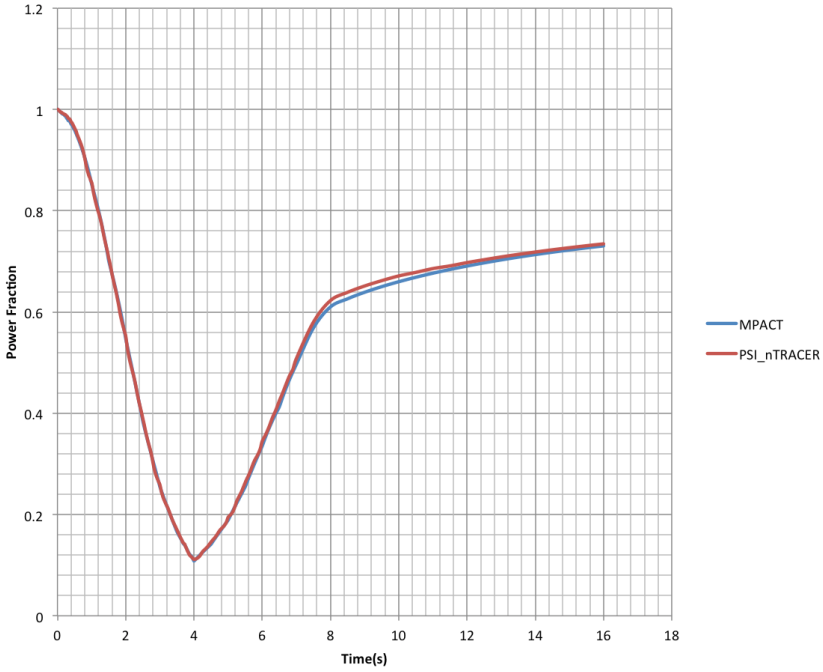

Figure 4.41 TD 4-3 power fraction results from different simulation soft wares.

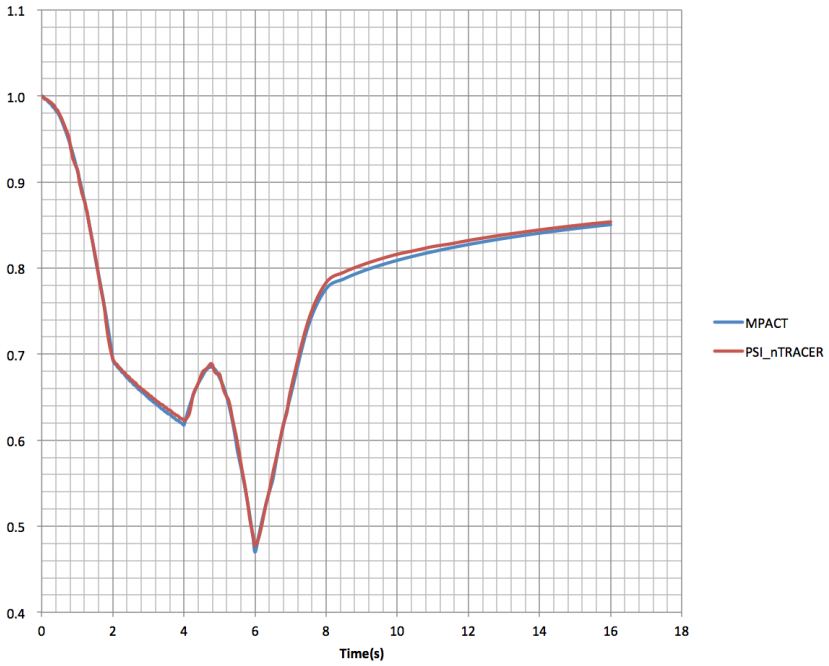

Figure 4.42 TD 4-4 power fraction results from different simulation soft wares.

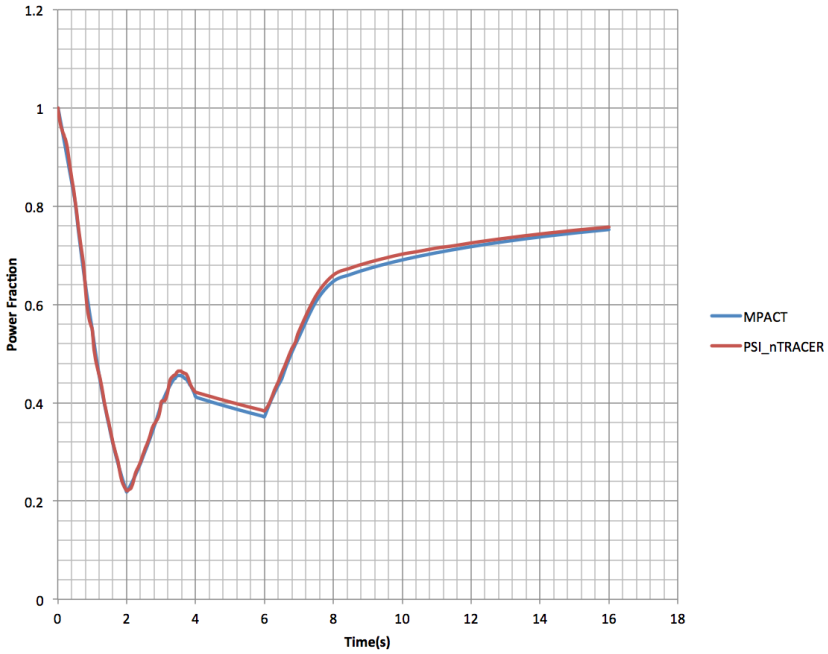

Figure 4.43 TD 4-5 power fraction results from different simulation soft wares.

Figure 4.41~Figure 4.45 shows power fraction deviation between MPACT and PSI nTRACER, using the following expression:

$$\Delta(t) = \frac{P_P(t) - P_M(t)}{P_M(t)} \times 100\%$$

in which $P_M(t)$ indicates power fraction of MPACT results at the time step of t, $P_P(t)$ indicates power fraction of the results from PSI nTRACER at the time of t, and $\Delta(t)$ indicates the power relative deviation at the time of t.

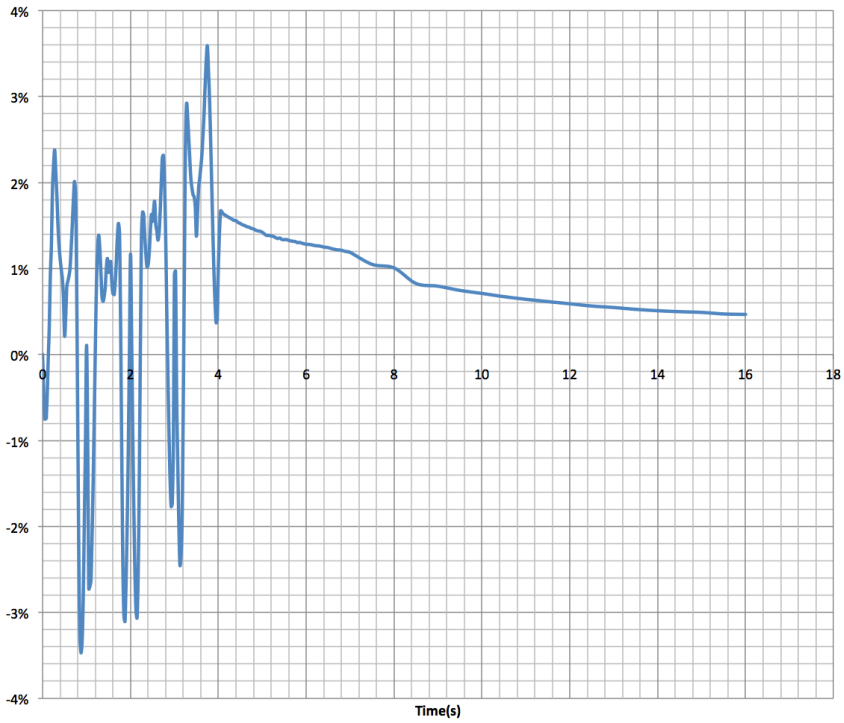

Figure 4.41 TD4-1 power relative deviation between MPACT and PSI nTRACER.

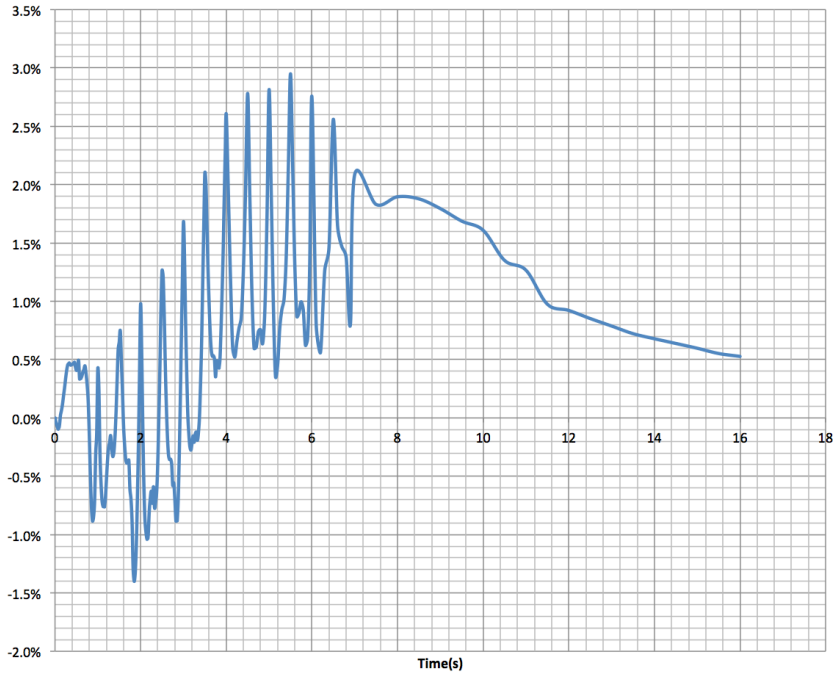

Figure 4.42 TD4-2 power relative deviation between MPACT and PSI nTRACER.

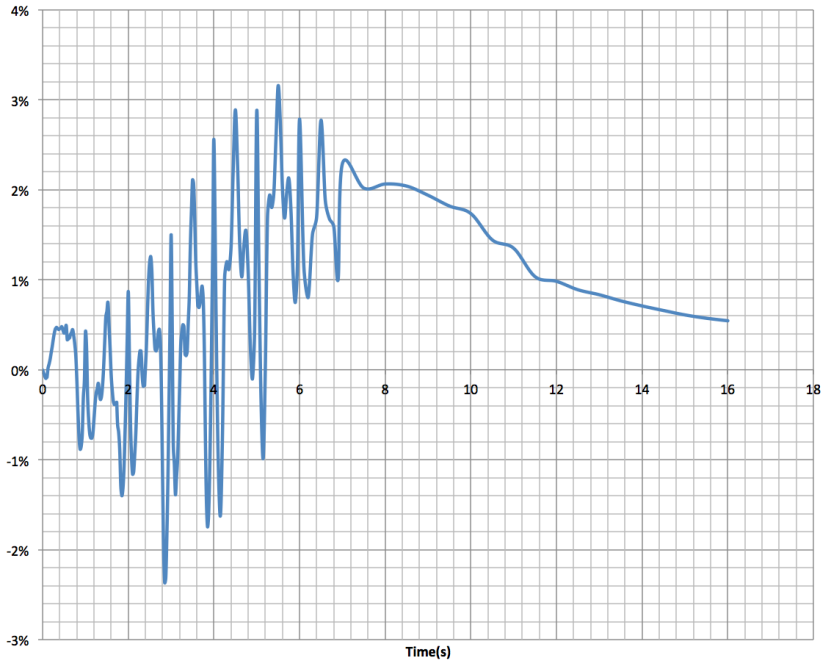

Figure 4.43 TD4-3 power relative deviation between MPACT and PSI nTRACER.

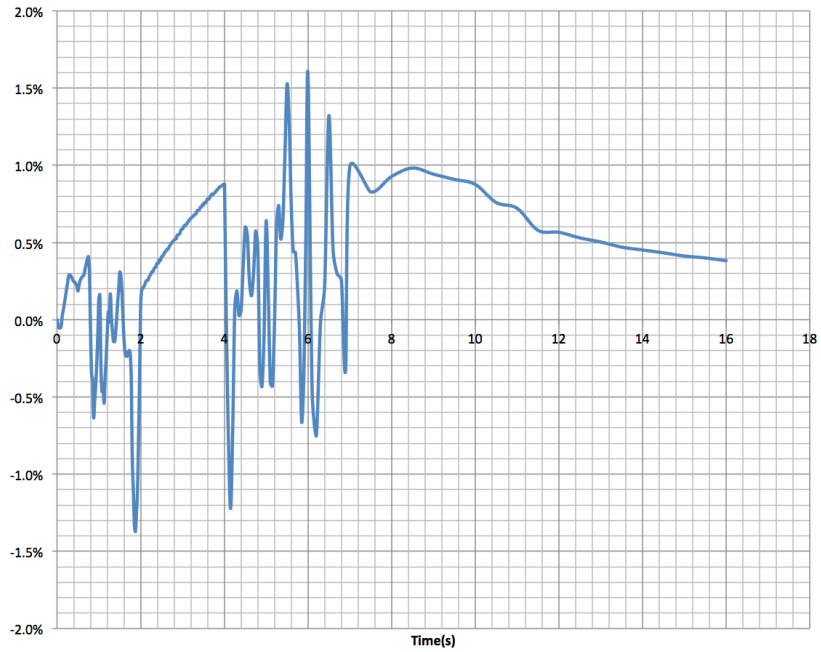

Figure 4.44 TD4-4 power relative deviation between MPACT and PSI nTRACER.

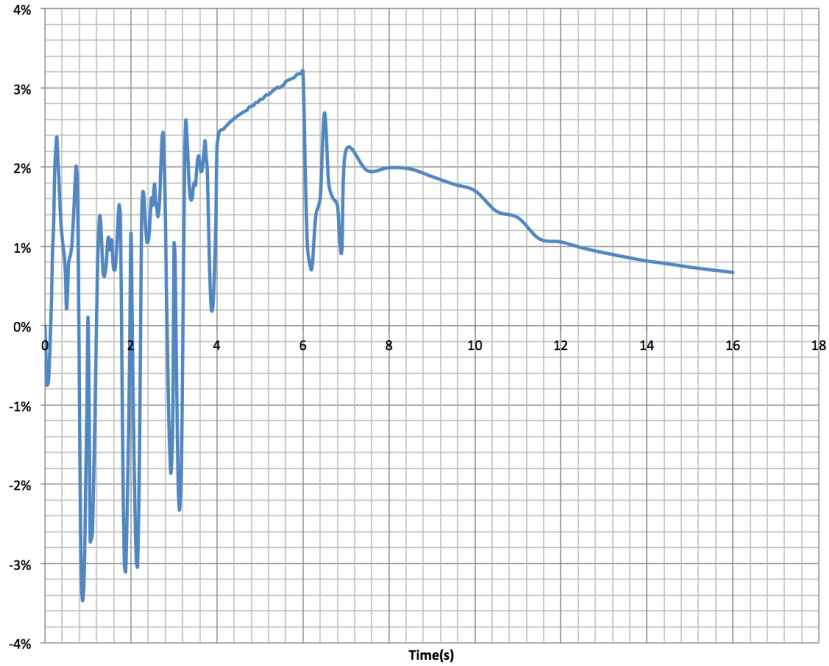

Figure 4.45 TD4-5 power relative deviation between MPACT and PSI nTRACER.

4.1.4 Summary and Conclusions

C5G7 benchmark is based on the C5G7 benchmark [Boyarinov, 2016] . The simulation of C5G7-TD was performed to continue the verification and validation of the transient capability in the MPACT code . Both 2D and 3D models were performed in the benchmark. A total of 6 exercises were included in the C5G7 transient problems referred to as TD0, TD1, TD2, … , TD5. Each exercise contained several cases which were based on the either a 2D or 3D models and involved either an insertion/withdrawal of control rods or a density change of the moderator. Both the 2D and 3D benchmarks were performed with MPACT and the results indicate generally very good agreement with the reference solution and for most cases good agreement with other code participants.

4.2 Progress towards VERA-CS Analysis of SPERT

The SPERT experiments have been used previously for code-to-code benchmarking of MPACT against KENO [Neutronics modeling of the SPERT III E-Core critical experiments with MPACT and KENO] and for comparison against experimental transient results [https://www.casl.gov/sites/default/files/docs/CASL-U-2015-0158-000.pdf], so they are a natural choice for validation of the coupled transient capability.

4.2.1 SPERT Modeling Challenges and Resolution

The SPERT geometry provides a variety of challenges that require special consideration for modeling. There are 60 assemblies—48 standard assemblies, 8 control rod assemblies, and 4 transient assemblies. The standard assemblies consist of a 5x5 grid of fuel pins. The control rod assemblies consist of two distinct axial regions—a follower region containing a 4x4 grid of fuel pins surrounded by a bypass region and the poison region containing a borated steel channel box. The transient assemblies consist of a 4x4 grid of fuel pins surrounded by a bypass region with a quarter

of the cruciform transient blade in one corner of the bypass region. All of the fuel grids are centered in the assemblies with a pin pitch of 1.4859 cm.

Since MPACT requires a uniform pin lattice structure across assemblies, SPERT must be modeled with quarter pin geometry. Unfortunately, this option is not available currently with VERA input, so the model can only be built with the MPACT native input. This further necessitates that the CTF input deck(s) be built independently since there is no VERA input file from which to use the automated process to generate CTF inputs.

While both MPACT and CTF are independently capable of modeling the SPERT geometry (or at least a reasonable approximation of it), the extra planar and axial heterogeneity provide significant challenges to mapping between the two codes. Fundamentally, MPACT is built around the fuel pin structure, while CTF is built around the channel structure. Since MPACT is the master code when coupled to CTF, the mapping between the two codes was built around MPACT's existing pin power structure. Hence, there is no means by which to pass moderator TH data from CTF to MPACT for the bypass regions in the control rod and transient assemblies. As an initial resolution, the MPACT mapping routine was modified to recognize the bypass region and skip that region when updating TH properties for coupled calculations. The moderator properties in the bypass region are assumed to remain at inlet conditions. For cold zero power, this should have negligible effect on the results. For hot conditions, it may be necessary to modify MPACT to approximate the temperatures of the bypass region in another manner.

The poison region above the follower region in the control rod assemblies challenged the data structures used for passing power and TH data between MPACT and CTF. Modifications were considered for MPACT, but deemed to have potentially undesirable future consequences. Instead, the problem was resolved by a minor modeling approximation. The moderator region internal to the poison box was converted from rectangular pin meshes to the same quarter pin meshes used for modeling the fuel with water in place of the fuel and clad. This itself was not an approximation, but it required the inner dimension of the poison box to be increased slightly to accommodate the full grid of water pins. The outer dimension of the poison box was increased to conserve the volume of the poison box. The effect of this approximation was investigated and determined to be less than 5 pcm on k-eff for an infinite array of control rod assemblies.

Combining assemblies with different numbers of channels and fuel rods into a single model also creates problems with the mapping routine. The internal CTF fuel rod map necessarily has zero entries for the control rod or transient assemblies. However, CTF interprets these zeros as boundary conditions and adds offsets as appropriate. For the SPERT model, this interpretation is incorrect and the offset must be negated to properly map between CTF and MPACT. As a temporary resolution, the offset is removed (boundary conditions are not affected since there are no partial assemblies in the CTF model). While this allows the mapping routine to work correctly for SPERT, final resolution that is generally implementable may require a significant refactor of the internal CTF mapping routine.

In addition to the geometry issues discussed above, it was discovered that the fluid flow through the core was not being distributed to the assemblies correctly. MPACT uses the maximum flow area of the axial sections comprising each assembly to determine the flow area of the assembly, which in turn is used to determine the percentage of the total core flow rate directed to that assembly. For the control rod assembly, this methodology artificially increases the flow rate for the control rod

assemblies since the poison region contains a significantly larger flow area. The determination of the flow area was modified to only consider axial sections with fuel to resolve this issue.

Finally, there is some discrepancy between how CTF and STH utilize the flow rates with respect to the bypass regions for simulations containing multiple assemblies. Resolution of this issue is ongoing, but not expected to provide a significant hurdle.

Of note, none of these issues are specific to transients. They exist for steady-state as well, and their resolution in steady-state is sufficient is equally valid for transients.

4.2.2 Initial Results

In order to investigate the above issues and determine satisfactory resolution, a series of progressively more complex simulations was performed. Initially, the three types of assemblies were simulated individually. As previously stated, the MPACT and CTF models had to be built independently. Single assembly MPACT models were created from an existing full core SPERT model. The corresponding CTF models were built by hand for the standard, control rod, and transient assemblies.

The individual steady-state assembly models were run with STH and coupled to CTF. Reflective boundary conditions were utilized on the sides and vacuum boundary conditions above and below the assembly. Figures X1, X2, and X3 show the axial moderator and fuel temperature profiles for the standard assembly, the control rod assembly, and the transient assembly, respectively. For each assembly, the moderator and fuel temperature are shown for three locations in the assembly, which are depicted in the inset assembly overview.

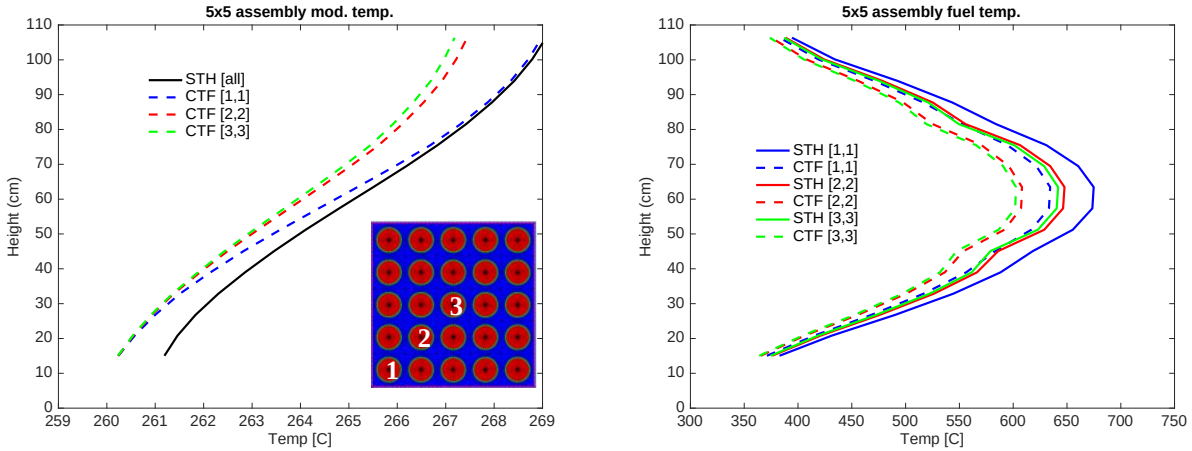

Figure 4.46. Axial moderator and fuel temperature profiles for 3 locations in the standard assembly

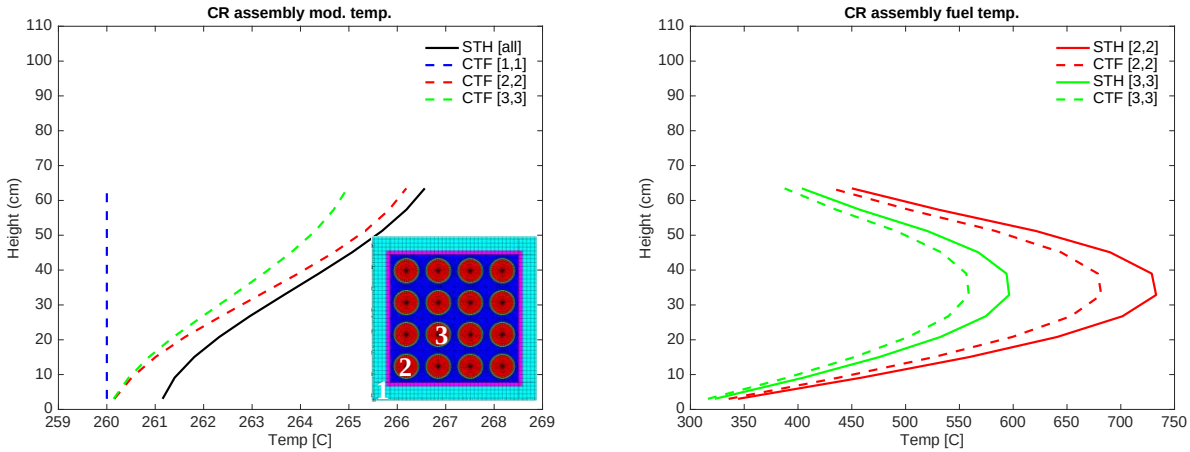

Figure 4.47. Axial moderator and fuel temperature profiles for 3 locations in the control rod assembly

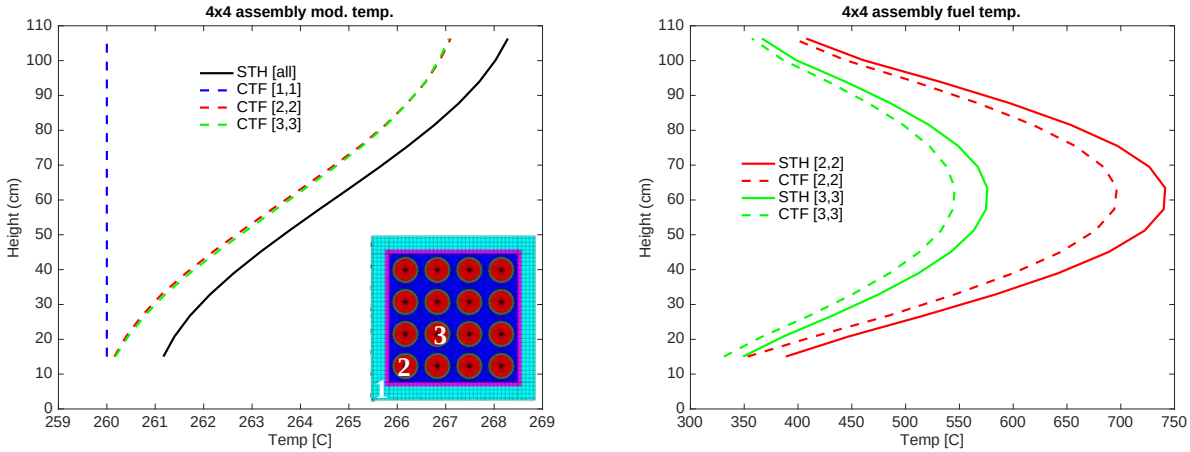

Figure 4.48. Axial moderator and fuel temperature profiles for 3 locations in the transient assembly

These plots show that the modifications to MPACT and CTF allow for coupled calculations that produce reasonable results. From previous investigations, we know that the discrepancy between the CTF and STH results is almost entirely due different correlations used for the TH properties (thermal conductivity, specific heat, etc.). [CASL-U-2017-1303-000].

Having gained confidence that the individual assembly coupling issues have been resolved for SPERT, a 2x2 assembly model was created for MPACT and CTF containing all 3 types of assemblies. A simple overview of the model is shown in Figure X4. This simulation that revealed both the issue with internal CTF mapping for different sized assemblies and the flow rate distribution issue discussed in the previous section have been resolved. Results are not presented since they are still tainted by the flow rate discrepancy between MPACT STH and CTF. However, this minor issue aside, the model demonstrates the ability to run coupled MPACT-CTF for transients.

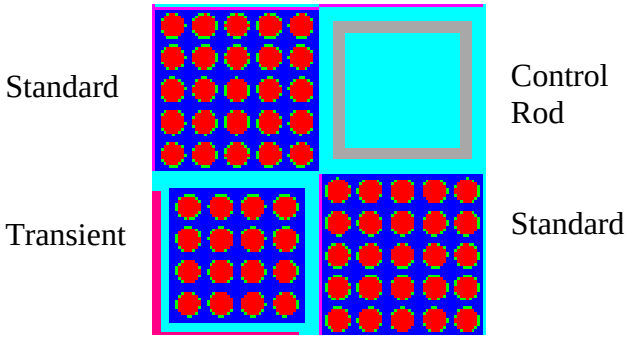

Figure 4.49. 2x2 SPERT model

Additional testing was done to ensure that both MPACT and CTF are able to run in parallel with the 2x2 model without encountering new obstacles. Finally, with that assurance in place, a CTF full core SPERT input was developed. The CTF input is designed to be run in parallel on 16 processors. MPACT can be run in parallel on 16 or more processors. It has been verified that the full core coupled transient model runs without encountering any fatal errors.

4.2.3 Remaining Work

The input development to simulate the SPERT transient with coupled MPACT-CTF has been completed, and the necessary code modifications are nearly so. All that remains is to resolve the flow rate discrepancy between MPACT STH and CTF and determine the final disposition of the code modifications. Once the first of these is completed, the full core SPERT transient can be simulated with coupled MPACT-CTF and compared to both experiment and MPACT standalone results.

4.3 DNB Demonstration on Hypothetical SMR

During the fuel heat-up phase of a RIA, the width of the pellet-cladding gap decreases due primarily to the larger thermal expansion coefficient of the fuel pellet relative to the cladding. In the event of gap closure (i.e. the fuel pellet contacts the cladding), the effective gap thermal conductance may increase by an order of magnitude or more, which greatly enhances the heat transfer rate from the fuel pellet to the cladding. The resultant increase in cladding outer surface heat flux may lead to local departure from nucleate boiling (DNB) leading to possible cladding oxidation and/or cladding burst failure.

Recent development and testing efforts have been made to enable the CTF dynamic gap and fuel modeling capability within VERA-CS [1]. The CTF dynamic gap model is capable of predicting gap closure and resulting gap conductance increase during an RIA event due to differential thermal expansion, cladding strain, and other effects. This preliminary capability provides a significant advancement in the physical modeling of fuel and coolant behavior during RIA, relative to previous studies based on a constant gap conductance assumption [2].

4.3.1 Detailed Single-Pin Dynamic Gap Model Results

The dynamic gap model in CTF was applied first to a single-pin test problem using standalone CTF with a prescribed power pulse boundary condition. The model is based on the ‘TK1’ test from the NSRR Takahama RIA test series, which was previously analyzed with VERA-CS [3].

Figure 4.50 provides the time-dependent power pulse, which was applied as a time-dependent heat generation rate in the CTF fuel rod. For this model, the gap begins in an open condition and gap

closure occurs at approximately t=0.011 s (Figure 4.51) as the fuel heats up and expands at a faster rate than the cladding. The CTF dynamic gap model currently assumes an effective combined roughness of the fuel pellet and cladding of approximately 4.6E-06 m, which is assumed to correspond to a closed gap. In the approximately 0.003 s before gap closure, the gap conductance begins to increase noticeably due to reduced gap thickness and resulting enhancement to heat transfer through the gap gas.

Once the gap is closed, the gap conductance increases rapidly. The closed gap conductance model consists primarily of a solid contact component and a gas conduction component. The solid contact component increases as a function of contact pressure (Figure 4.52), which increases due to continued thermal expansion of the fuel after initial gap closure. Due to competing effects, the gap conductance decreases slightly until about 0.033 s before increasing again; however, the gap conductance remains roughly an order of magnitude higher than in the open-gap state, and therefore the ΔT across the gap remains small throughout the closed-gap portion of the transient.

Results for cladding-to-coolant heat transfer regime and cladding temperature are presented in Figure 4.53. DNB occurs at approximately 0.022 s due to the large increase in cladding surface heat flux which is delayed with respect to the power peak. Results are presented for the post-DNB regime as well; however, the post-DNB modeling capabilities of CTF have not been sufficiently tested at this time, and the primary calculation of interest is the onset of DNB.

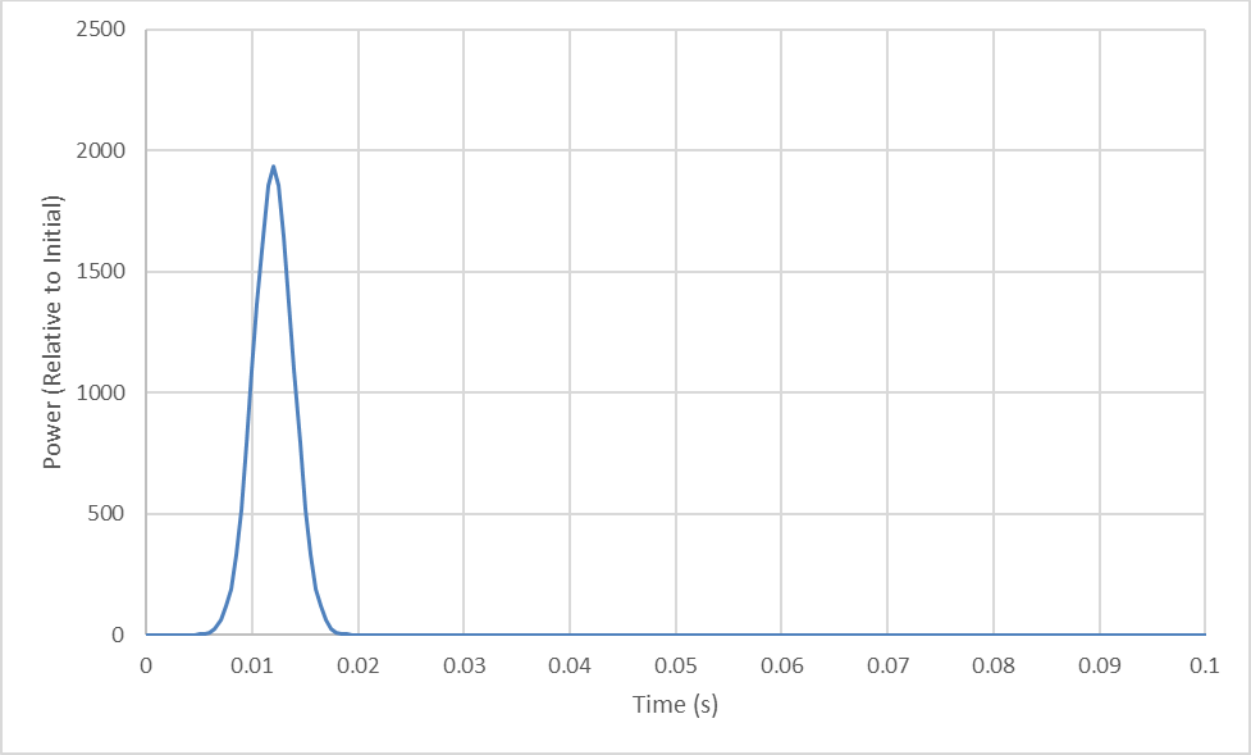

Fig. 4.50 - Power pulse for the NSRR Takahama test

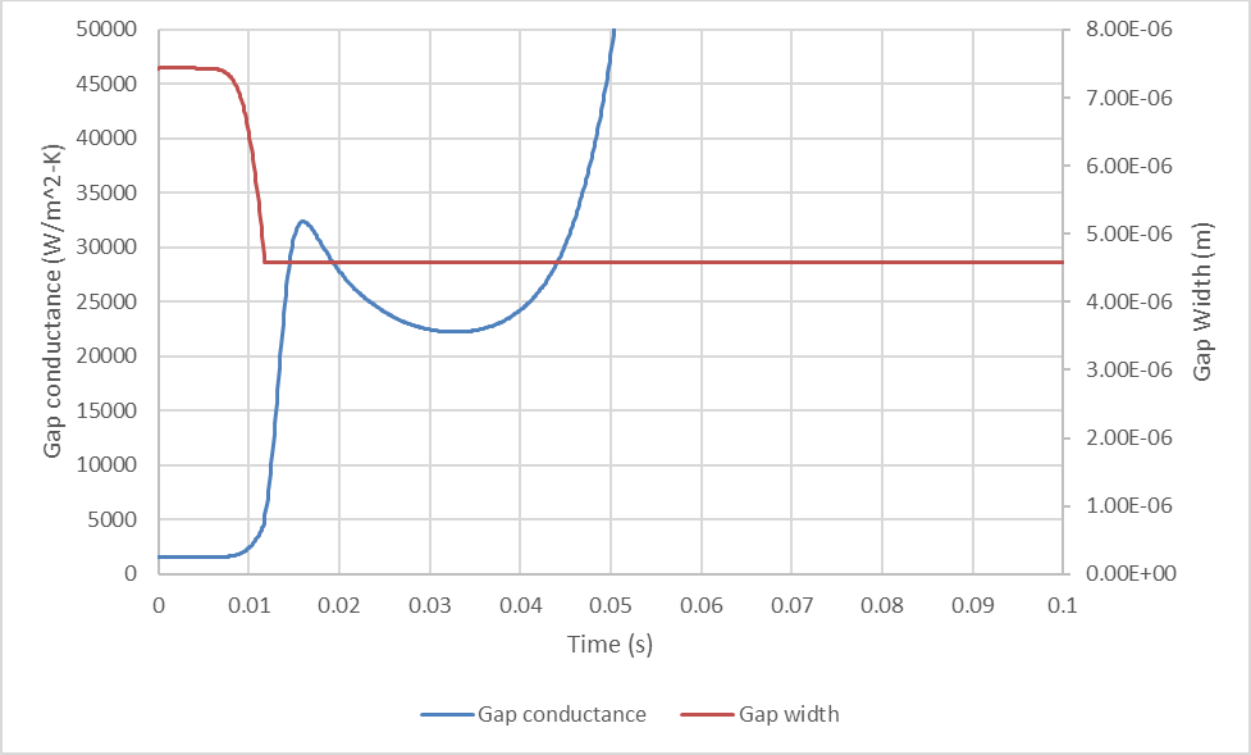

Figure 4.51 - Gap width and gap conductance predicted by the dynamic gap model for the NSRR TK1 test

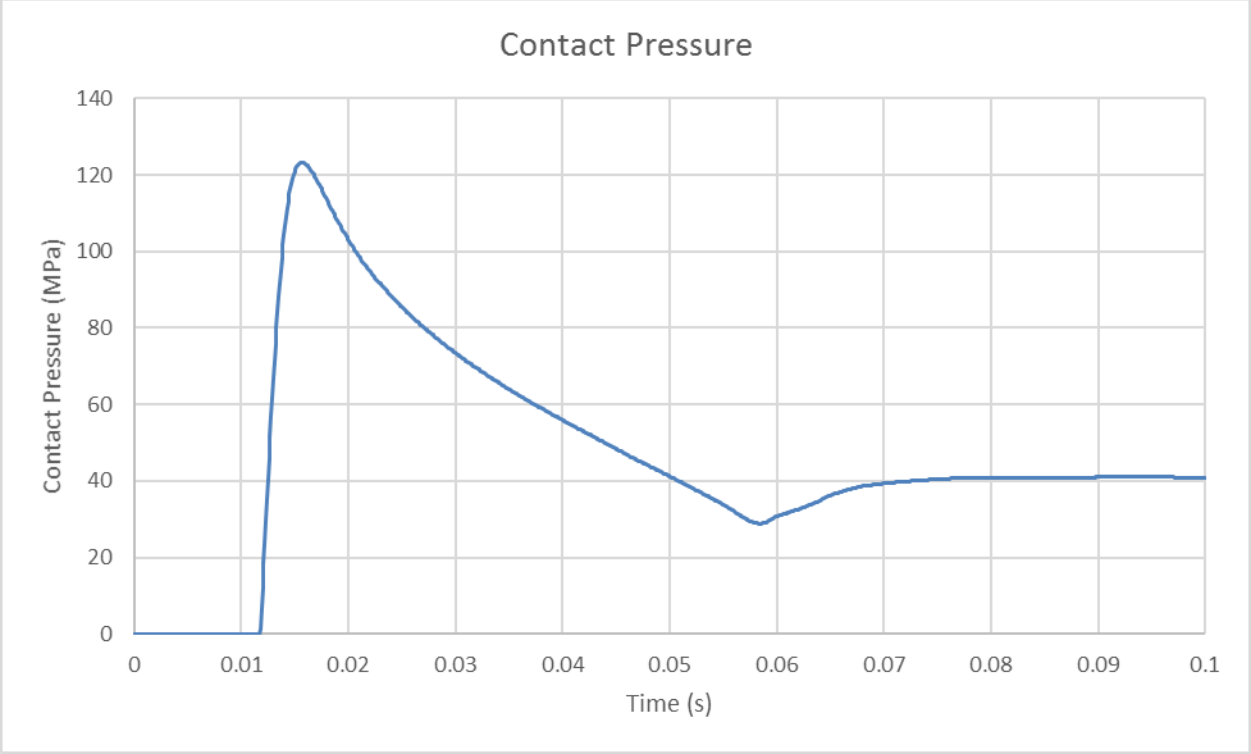

Figure 4.52 - Contact pressure between fuel pellet and cladding predicted by the dynamic gap model for the NSRR TK1 test

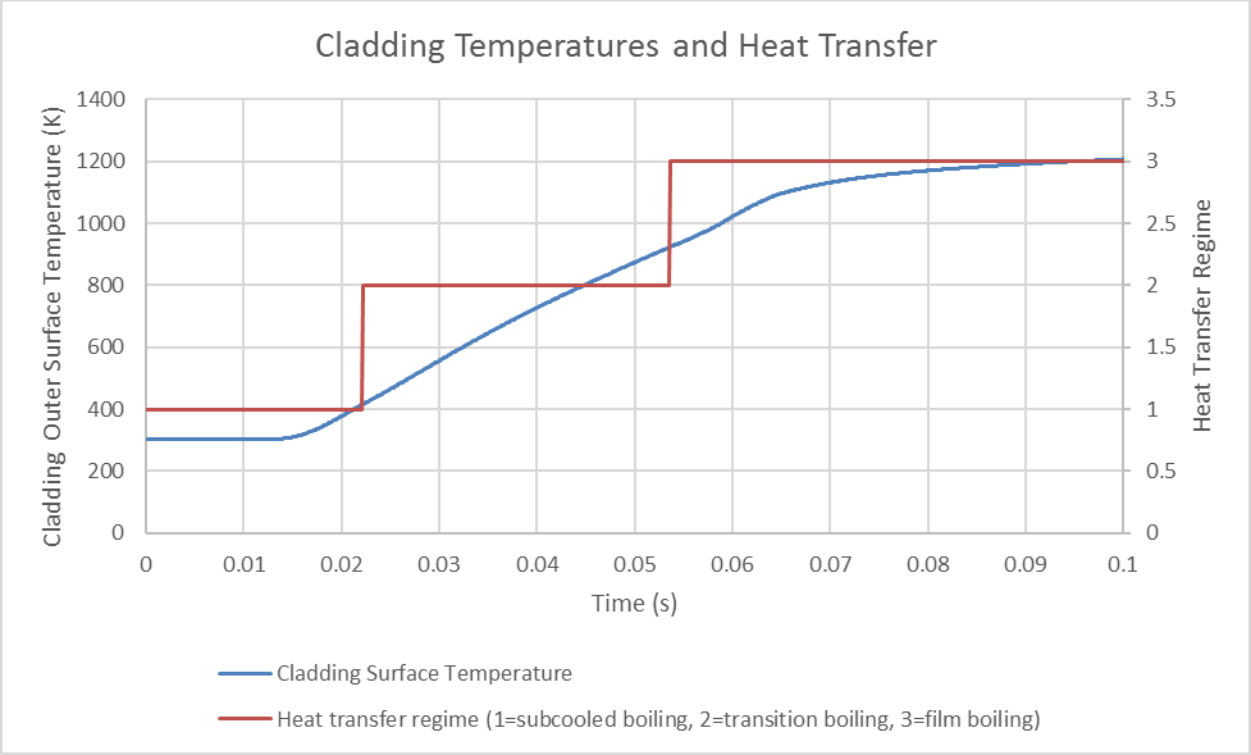

Figure 2.53 - Cladding temperature and wall heat transfer regime for the NSRR TK1 test

4.4 Preliminary Full Core AP1000 Demonstration

A preliminary simulation was performed of a Rod ejection event for the **AP1000** core at the end of cycle (EOC) hot zero power (HZP) and hot full power (HFP) conditions. In this section, preliminary HFP results are provided only. Additional **AP1000** simulations and analyses can be found in CASL-X-2017-1417-000 as part of the L3:AMA.CP.P15.11 milestone.

Depletion calculations were first performed to deplete the core to end of Cycle 1 and then calculations were restarted to simulate the rod ejection events at EOC. A brief description of the **AP1000** core and the VERA-CS model are given below, followed by the transient analyses.

4.4.1 *AP1000* Cycle 1 Depletion Calculations

The **AP1000** first core loading pattern consists of 5 fuel regions covering a wide range of enrichments including radially zoned enrichment in 2 regions. There is also a combination of burnable absorbers; the Westinghouse integral fuel burnable absorber (IFBA) and the wet annular burnable absorber (WABA) are used. The fuel description is summarized in Table 0.

Table 0.9 *AP1000* reactor cycle 1 fuel loading description

Region Summary			
Fuel Region	**Assemblies**	**# Fuel Rods**	**w/o U-235**
1	16	264	0.74
2	49	264	1.58
3	28	264	3.2
4	36	64	3.4
		152	3.8
		48	4.2
5	28	64	4.0
		152	4.4
		48	4.8
TOTAL	157		
Axial Blanket			
Fuel Region		**# Fuel Rods**	**w/o U-235**
3		264	1.58
4		264	3.2
5		264	3.2

The **AP1000** plant operates following the MSHIM control strategy, an advanced operational strategy that entails operation with multiple control rod banks inserted in the core. M-banks based on tungsten material are used for reactivity control, and standard silver-indium-cadmium (Ag-In-Cd) rods, (AO-bank), are used for axial power distribution control. The quarter core control banks configuration is shown in Figure 0..

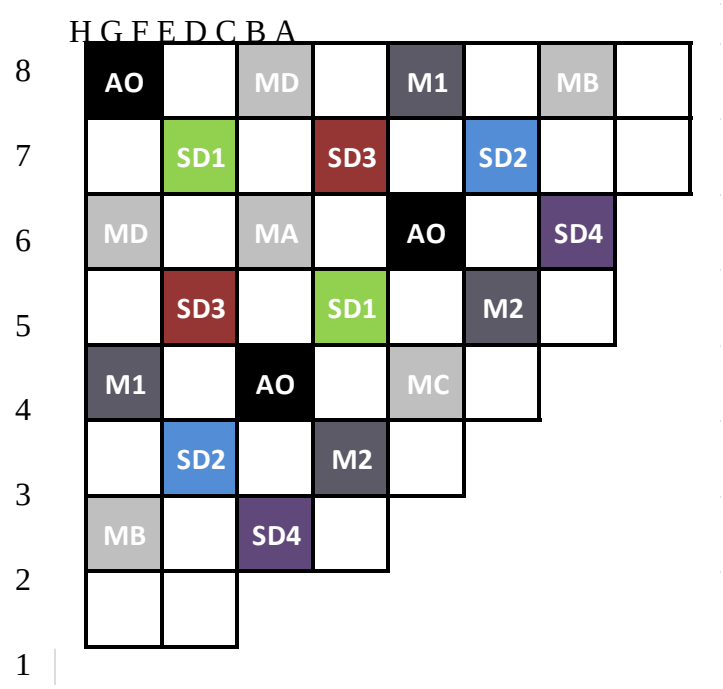

Bank		Number of Clusters
MA	(MSHIM Control Gray Bank A)	4
MB	(MSHIM Control Gray Bank B)	4
MC	(MSHIM Control Gray Bank C)	4
MD	(MSHIM Control Gray Bank D)	4
M1	(MSHIM Control Black Bank 1)	4
M2	(MSHIM Control Black Bank 2)	8
AO	(AO Control Bank)	9
S1	(Shutdown Bank 1)	8
S2	(Shutdown Bank 2)	8
S3	(Shutdown Bank 3)	8
S4	(Shutdown Bank 4)	8
TOTAL		69

Figure 0.54 Control Rod Locations

The **AP1000** VERA-CS depletion model set the core power at 100% and core inlet temperature to 537.2 °F consistent with HFP inlet temperature for the **AP1000** plant Cycle 1. The criticality search was set to boron and xenon was set to equilibrium. The feedback was turned on, so moderator density was calculated by CTF. The fuel temperatures were calculated using a lookup table defined as a function of rod power and burnup.

The mechanical shim (MSHIM) control strategy of **AP1000** will operate the plant with control rods inserted, by maintaining the AO bank at 238 steps, MA or MD banks at 90 steps or fully withdrawn, and switching them every 1 GWD/MTU.

A quarter-core model was used for the depletion calculations with 56 axial meshes, 4 in the bottom reflector region, 3 in the top reflector region, and 49 in the active fuel region. The quadrature set used 16 directions. Flux calculations used a 51 energy group library, with transport-corrected P0 scattering. MPACT performed the transport sweeps using 896 cores of INL's falcon computing platform, using spatial domain decomposition only. The CTF model included 11471 channels, 22813

gaps, and 11471 rods in the quarter-core model. For parallel processing, CTF partitioned the spatial domain based on quarter assembly boundaries and performed the simulations on 157 cores.

4.4.1 Transient Calculations

In typical licensing applications, the rod ejection events are simulated with additional conservatisms, such as reducing the Doppler feedback and the delayed neutron fraction, and increasing the moderator coefficient and the ejected rod worth. Because these 'dials' have not been implemented in VERA-CS, those parameters are calculated by the code and used as dictated by the physics of the problem in VERA-CS simulations.

For both HZP and HFP case, a 5 second transient was simulated for the rod ejection events.

4.4.1.1 Initial Conditions and Accident Assumptions

Initial Power Level: The accident was analyzed with core at either HZP or HFP initial conditions. The initial power level for the HZP case was assumed to be 1.E-03% of the nominal power. For the HFP case, the calculations started at 100% of the nominal power.

Initial RCS Flow: Full reactor coolant flow was assumed to maximize heat transfer from the clad to the coolant.

Initial Core Inlet Temperature and Pressure: The core inlet temperature and outlet pressure were assumed constant at their nominal values consistent with the nuclear design model, 537.2°F at HFP and 557°F at HZP and 2250 psia, respectively.

Ejected Rod: Based on analysis performed using the Westinghouse tools, most limiting control rod location was identified as F-12 for the ejected rod. Ejection is assumed to be completed in 0.1 seconds. In both HZP and HFP simulations, the ejected rod is assumed to be initially fully inserted in the core. In reality, control rods would have rod insertion limits (RIL). Initial full insertion was assumed to artificially maximize the reactivity during the ejection transient.

Reactor Trip: The reactor trip was simulated by dropping in the partially or fully withdrawn rod banks using conservative control rod acceleration and terminal velocity. An additional conservatism was applied by assuming that the rod adjacent to the ejected rod at G-11 location did not trip; i.e. remained fully withdrawn following the trip signal. The typical trip time delay of 0.5 seconds was applied, making the start of rod motion for shutdown 1.2 seconds into the transient.

4.4.1.2 Rod Ejection Simulations

A restart for rod ejection was initiated from EOC at either HFP conditions with full core symmetry. Preliminary calculations were performed with MPACT with internal heat conduction feedback and later on MPACT coupled with CTF. The control rod was ejected from a fully inserted position in order to have a large worth and to create a superprompt critical transient, leading to a power pulse dampened by Doppler feedback. This severe scenario would facilitate assessing the code with respect to the expected results.

Different time step sizes were chosen for different periods in the transient, depending on the rod movements and to optimize the run time with large time step sizes in the periods after the rod was fully ejected. Table 0 shows the periods and the time step sizes used in the simulations. This time step size scheme resulted in 193 state-point calculations for a 5 second transient.

Table 0.10 Time Step Sizes used in the Simulations

Time Period	Time Step Size	Remark
0.0-0.1	0.005	Rod Ejection
0.1-1.2	0.010	No rod movement
1.2-2.0	0.025	Reactor trip
2.0-3.7	0.100	Reactor trip continues
3.7-5.0	0.100	No Rod Movement

Other transient input options included the following:

- Prompt kinetics calculation was used during the transient solver.
- CMFD acceleration was performed during the transient solve.
- Theta discretization method was used with the theta value of 1.0 (equivalent to Backward Euler method).

Those input options as well as the time step sizes given in Table 0 were used in both HFP and HZP simulations.

4.4.1.3 MPACT with Internal T/H

At the end of Cycle 1 at full power, a restart for rod ejection was initiated. As described above, the ejected rod was initially at fully inserted position. Within 0.1 seconds, the ejected rod cleared the core in 264 steps. Figure 0. shows the power pulse starting at 100% power and reaching ~740% of the initial power at 0.13 seconds into the transient. At the peak, the total reactivity insertion (Figure 0.) was ~500 pcm, which was slightly less than a dollar with β_{eff}= 0.0053. Radial pin-power distribution at the peak of the power pulse is seen in Figure 0.. The power distribution was highly asymmetric and localized, as expected. High power rods were clustered in and around the ejected rod, and power tapered off away from the ejected rod. The maximum power peaking factor reached 5.8 at the peak of the pulse.

Axial power profiles in the assembly with the ejected rod at selected times during the transient are shown in Figure 0.. As the rod was being ejected, power peaking occurred in the region below the tip of the control rod until the rod was fully ejected.

The thermal-hydraulics feedback was applied to the neutronic solver in MPACT using a simplified internal TH module, which utilized 1D radial heat conduction/convection equations to provide the radially-dependent Doppler feedback and 1D axial mass/energy equations for the channel flow with the constant pressure assumption. The internal transient TH conduction solver implemented in MPACT did not include transient convection and therefore was not adequate for longer transients. Nevertheless, the fuel temperature distribution as shown in Figure 0. provided the principal feedback mechanism to turn the pulse around.

MPACT with internal T/H calculations required ~34 hours of wall-clock time on 3584 cores on INL's *falcon* to simulate 193 state-points for a 5 second rod ejection at HFP transient.

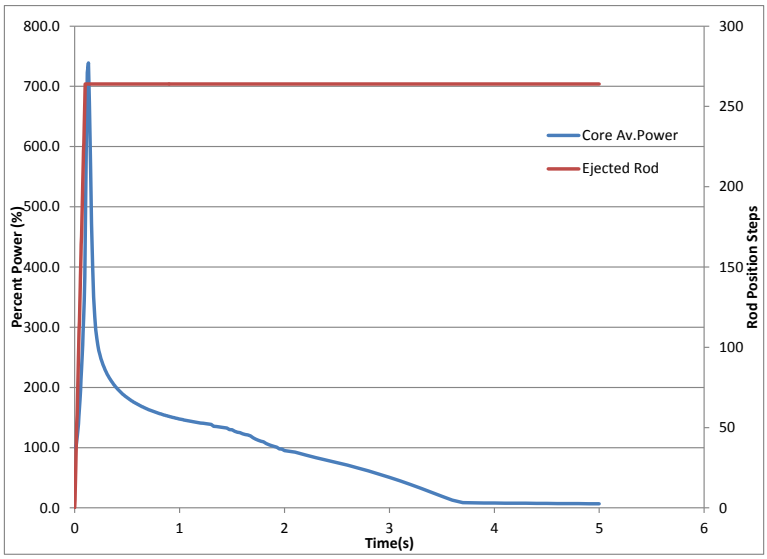

Figure 0.55 Core Average Percent Power and Ejected Rod Position

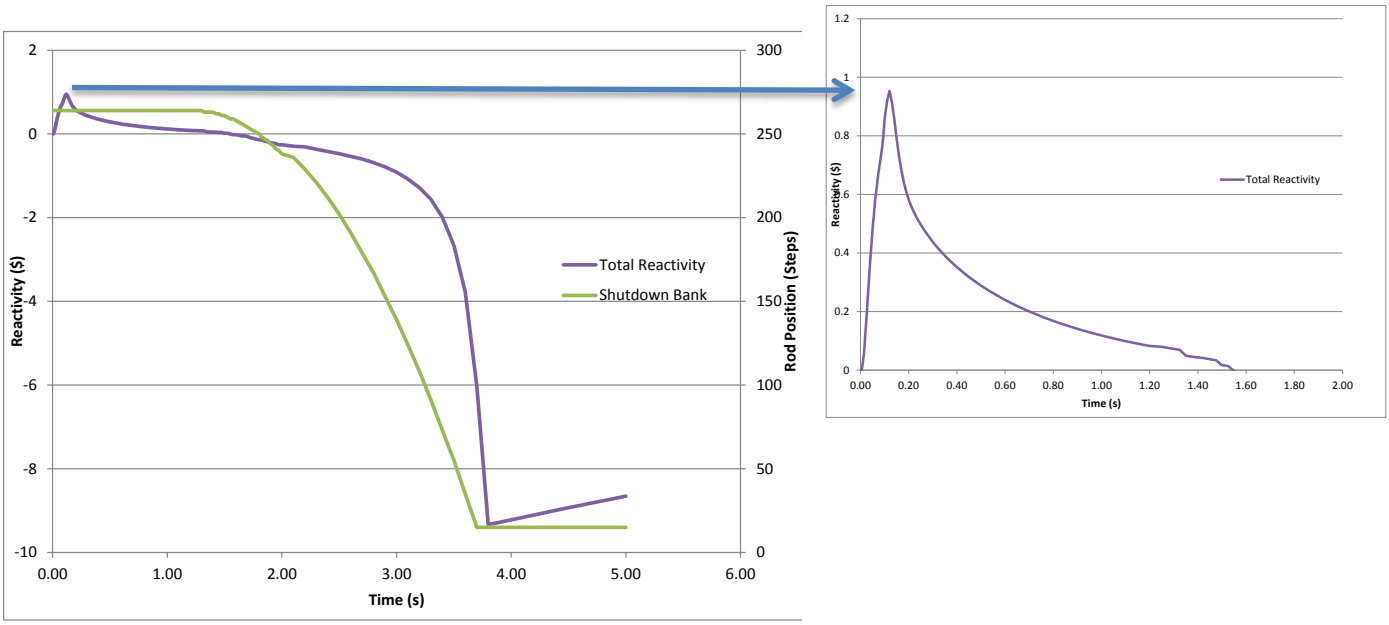

Figure 0.56 Core Total Reactivity and Shutdown Rod Position

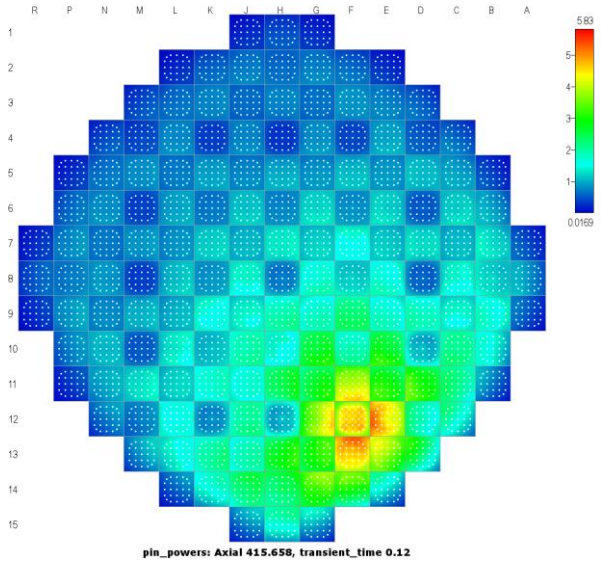

Figure 0.57 Pin Power Distribution near the top of the core at time = 0.13 s.

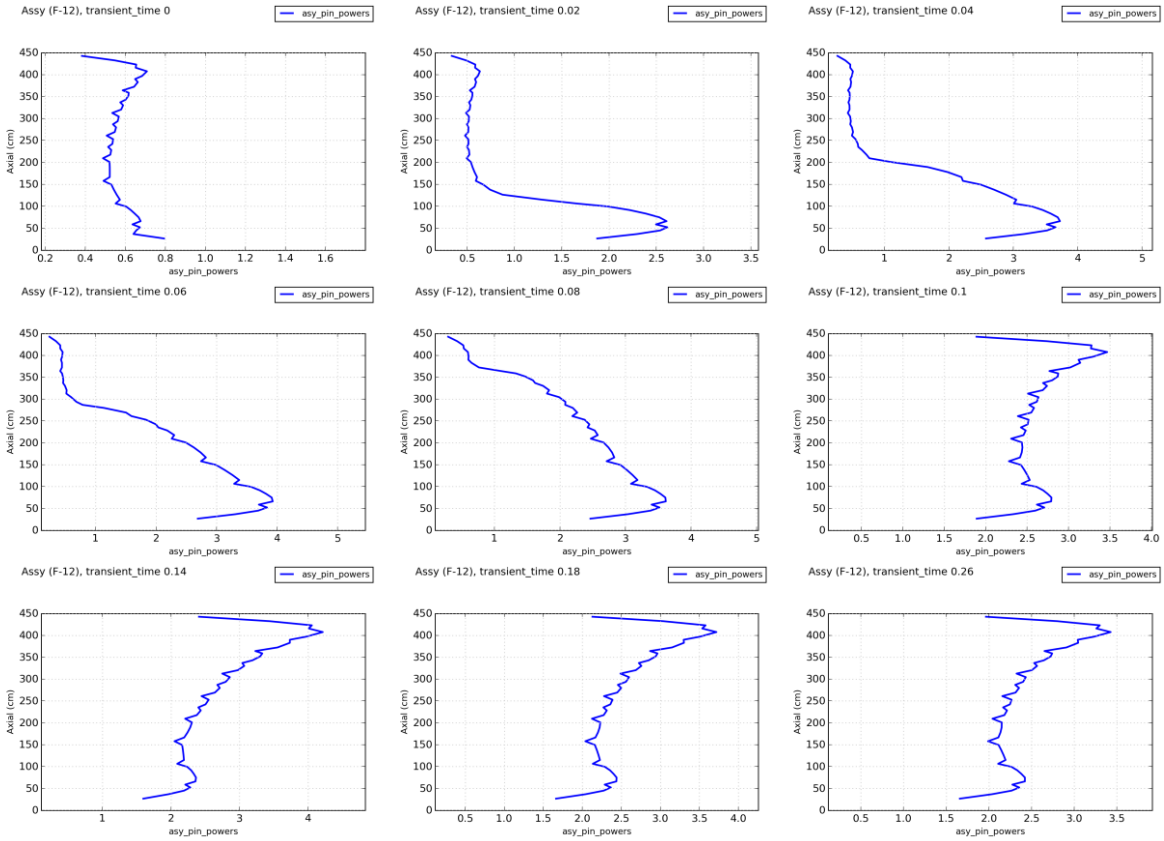

Figure 0.58 Assembly Average Axial Power Distribution at different transient times

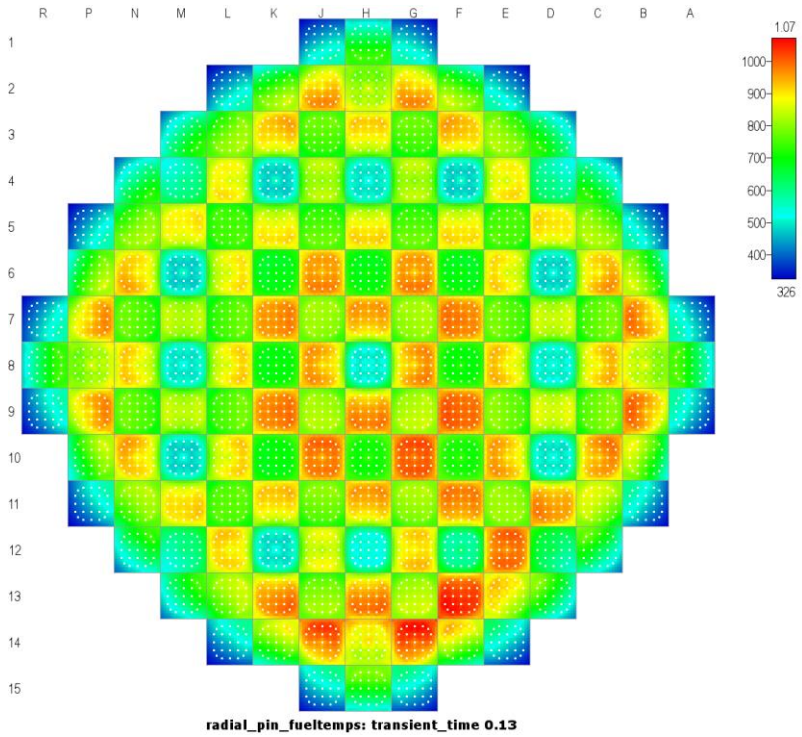

Figure 0.59 Fuel Temperature Distribution near the top of the core at time = 0.13 s.

4.4.1.4 MPACT Coupled with CTF

The same transient, i.e., rod ejection at HFP at the end of Cycle 1 was re-run with MPACT coupled with CTF. As previously indicated, the simplified TH model implemented in MPACT may provide sufficient accuracy for the first few milliseconds of a fast transient event, such as the RIA, since the thermal-hydraulics aspects may not have enough time to catch up with the neutronics during this initial period. At the tail end of the power pulse however, a more rigorous thermal-hydraulic modeling maybe required to comprehensively capture the associated TH phenomena. These phenomena are modeled in CTF coupled to MPACT within the CASL core simulator VERA-CS.

As before, the ejected rod was initially at fully inserted position. Within 0.1 seconds, it was ejected from the core, clearing 264 steps. Figure 0.60 shows the power pulse starting at 100% power and reaching ~635% of the initial power at 0.11 seconds into the transient. This peak value is ~100 percentage points smaller than that of MPACT with internal TH. At the peak, the total reactivity insertion was ~490 pcm, which was slightly less than a dollar with β_{eff}= 0.0053. Peak power and total reactivity insertion results (Figure 0.) indicate that CTF predicted slightly higher fuel temperatures, leading to stronger Doppler feedback and a more 'narrow' power pulse.

Figure 0. shows the core-wide radial pin power distribution close to the top of the core, axial pin power distribution at F-13 assembly location, and the F-13 assembly pin power distribution at the time of peak power. The radial power distribution was similar to what MPACT with internal TH predicted; higher peaking factors were observed in and around the ejected rod location and power tapered off away from the ejected rod. The maximum power peaking factor reached 5.7.

CTF calculations provide not only the temperature feedback to neutronics calculations but also evaluate phenomena that are important to safety at the sub-channel level. Parameters that are important to safety are fuel and clad temperatures and departure from nucleate boiling ratio (DNBR).

Figure 0.63 shows the maximum fuel, clad and liquid temperatures, as well as the peak linear heat rate. The maximum fuel temperature started at around 1768°C at the beginning of the transient and reached 2283.5°C at around 3.3 seconds, after which decreased with the reactor trip. Because a constant gap conductance was assumed in the calculations rather than a dynamic gap conductance model, the clad temperatures remained relatively low, reaching a maximum of 411.6°C. The maximum liquid temperature mostly remained at saturation temperature until the reactor trip. The peak linear heat rate followed the core power behavior.

Figure 0.64 shows the minimum DNBR (MDBR) and the associated equilibrium quality during the transient. W-3 correlation was used to calculate the critical heat flux. As the figure suggests, DNB was reached (DNBR < 1.0, assuming no uncertainties) at ~ 0.53 seconds, which was when equilibrium quality became positive, indicating two-phase conditions. It is observed that both the MDNBR and the associated equilibrium quality plots have oscillatory behavior. This is due to the fact that although the MDNBR is expected to occur in the hot assembly, it may occur in a different location (channel and axial level) at each time step, and the thermal-hydraulic conditions may be slightly different. With the core trip, channel conditions returned to subcooled liquid and the MDNBR began to rise.

MPACT coupled with CTF calculations required ~48 hours of wall-clock time on 3584 cores on INL's *falcon* to simulate 193 state-points for a 5 second rod ejection at HFP transient.

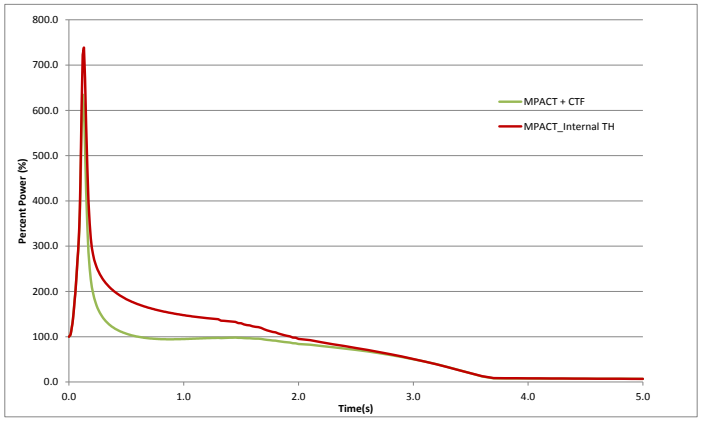

Figure 0.60 Core Average Percent Power with MPACT-CTF Coupled

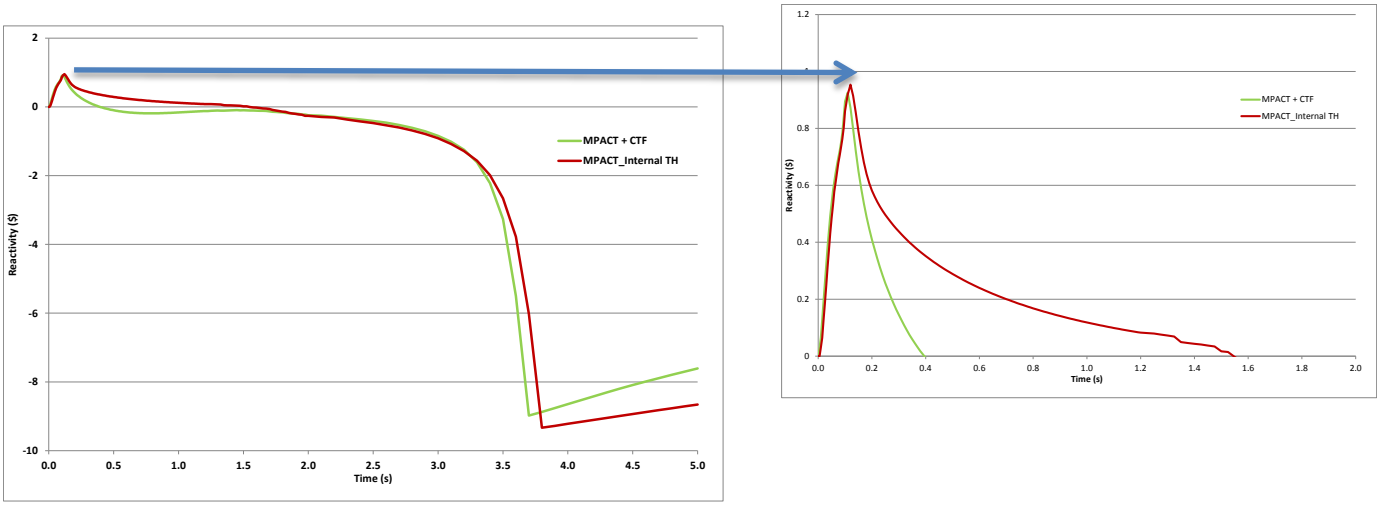

Figure 0.61 Core Total Reactivity with MPACT-CTF Coupled

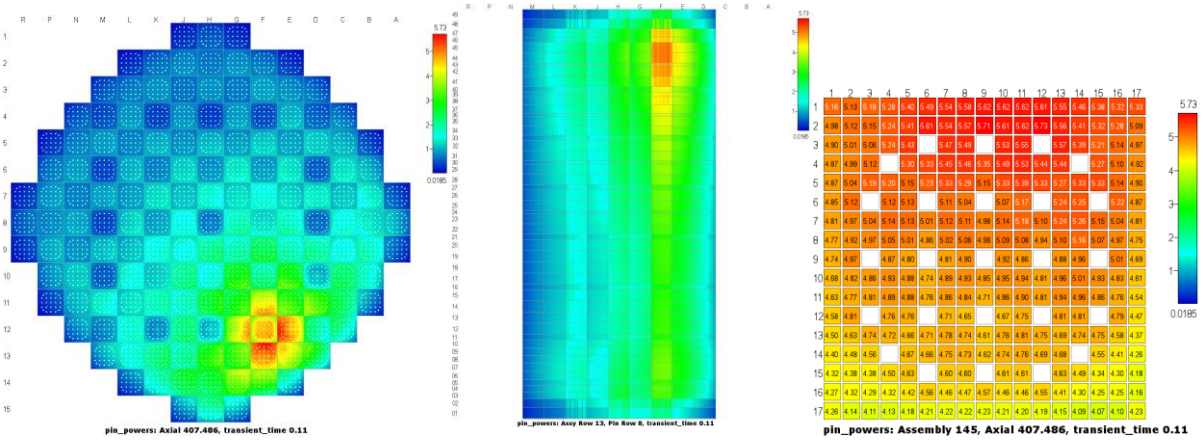

Figure 0.62 Core-Wide and Assembly Pin Power Distribution at time = 0.11 s.

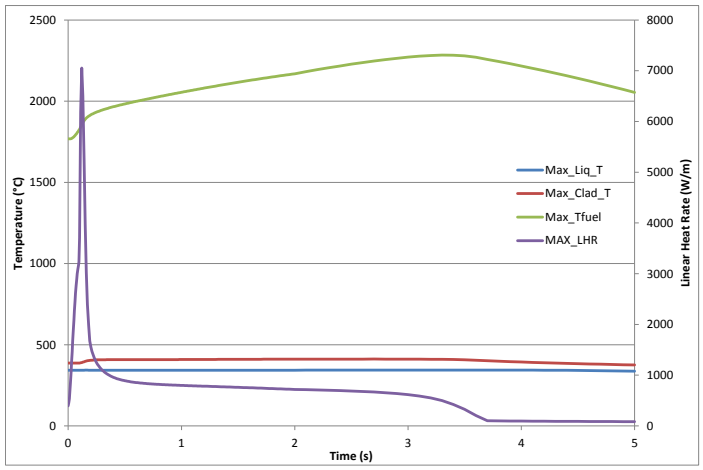

Figure 0.63 Maximum Temperatures and Linear Heat Rate for HFP Rod Ejection.

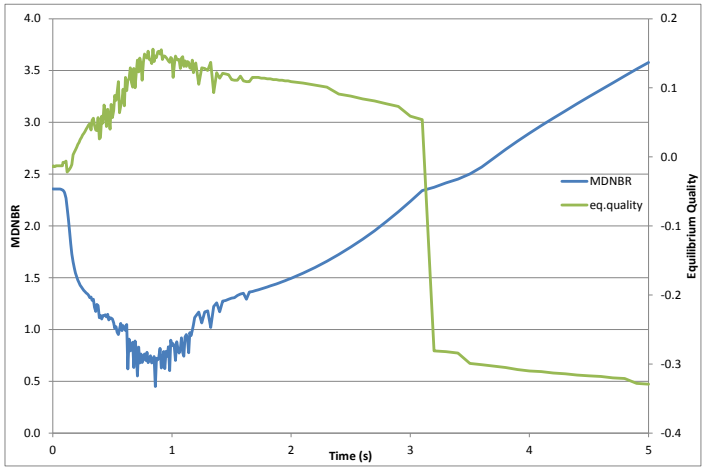

Figure 0.64 Minimum DNBR and Equilibrium Quality

5. CONCLUSIONS AND FUTURE WORK

5.1 Conclusions

The objective of this milestone was to continue the development, implementation, verification, and validation of the methods in VERA-CS necessary to solve the whole-core time-dependent neutron transport equations with pin-resolved detail for a practical PWR applications. This capability is necessary to provide the time dependent pin resolved neutron flux for analysis of the Reactivity Insertion Accident (RIA) as specified in the CASL RIA Challenge Problem Implementation Plan, CASL-I-2013-0060-000 [65]. The FY17 work reported here continued the FY16 work reported in CASL-U-2016-1188-000 which was primarily focused on MPACT and performed the methods, and Validation and Verification (V&V) efforts necessary to demonstrate the transient capability in VERA-CS in order to facilitate the L1 RIA milestone in FY18.

This report described the activities performed in FY17 in the three general areas of User Support, Methods Improvements, and in V&V and Demonstration. In the area of User Support various user requested features were added to the code such as detailed reactivity edits and improvements to the VERA input. In the area of Methods Improvements, the features added included user controlled variable time stepping, a one-group CMFD Acceleration, Delayed Energy Deposition model, as well as improvements to the overall code robustness for the transient solution. In the Area of V&V, the full suite of C5G7 Transient benchmarks was completed and significant progress was made on the solution of SPERT with VERA-CS. In the area of practical demonstration, a full core AP1000 demonstration problem was performed with VERA-CS. The work performed in FY17 enhanced the capability of performing VERA-CS transients for practical large-scale light water reactor problems with an acceptable computational burden and provided an important step in the completion of the CASL Reactivity Insertion Accident (RIA) Challenge Problem.

5.2 Proposed FY 18 Activities

Several activities are proposed for FY18 to improve the transient capability in VERA-CS. These include:

1. Assessment of RIA capability with Tiamat This milestone consists of a few tasks related to Tiamat to help assess future needs related to getting BISON incorporated into the RIA analysis.

2. Transient Development in MPACT This milestone consists of a few tasks that address user requests/usability more than fundamental methods. They are:
    a. Transient Restart
    b. Transient Input/Output improvements

3. VERA-CS Testing and Support for RIA In this milestone the same problems will be analyzed that Studsvik performed for EPRI. This will provide a real problem set and analysis to use as test bed to try and uncover issues with the codes. This will help to ensure that L1 analyses will have minimal issues.

4. Improvement of CTF for RIA analysis

a. Implementation of output edits for RIA,

b. Implementation of intra-pin power/temperature
c. investigation of semi-implicit coupling strategy

5. Evaluation of Radial Transport/Depletion Mesh Requirements for RIA. Investigate consistent meshing for couple fuel performance (80 radial rings) with neutronics (e.g. implement polynomials)

6. VERA plus Bison for RIA Previous simulations with Tiamat have shown that the BISON runtime increases considerably during power changes. This milestone is intended to provide an estimate for how much the runtime of transients cases can be expected to increase with Tiamat versus VERA-CS

7. Benchmarking of CTF fuel model and integration into VERA-CS
   a. Benchmarking of CTF and FRAPTRAN for RIA conditions,
   b. Benchmarking of BISON and CTF for steady state depletion conditions,
   c. Application of MPACT burnup to CTF fuel models

8. Complete Benchmarking of VERA-CS with SPERT

9. Improvement of two-phase heat transfer models in CTF Validation and improvement of transient CHF model and transient boiling

References

MPACT Team, “MPACT Theory Manual, Version 1.0,” University of Michigan, Ann Arbor, MI, October, 2013.

A. Zhu, et al, “Transient Methods For Pin-Resolved Whole Core Transport Using The 2D-1D Methodology In MPACT”, Proc. M&C 2015, American Nuclear Society, Nashville, TN, USA, April 19-23, (2015)

A. Zhu, et al., “A Multi-level Quasi-Static Kinetics Method for Pin-Resolved Transport Transient Reactor Analysis”, *Nuclear Science and Engineering*, 2016, **182**(4).

A. Zhu, et al., “Stability Analysis of the Backward Euler Time Discretization for the Pin-Resolved Transport Transient Reactor Calculation,” *Annals of Nuclear Energy*, 2016, **87**(2):252-266.

A. Zhu, et al, “The Implementation and Analysis of the MOC and CMFD Adjoint Capabilities in the 2D-1D Code MPACT,” Proc. M&C 2015, American Nuclear Society, Nashville, TN, USA, April 19-23, (2015)

J. Durgone, SPERT III Reactor Facility: E-CORE Revision, AEC Research and Development Report IDO-17036, November 1965.

Aaron Graham, “Subplane Method in MPACT,” CASL PHI Ticket Number 3738, April 15, 2016.

G. Swindelhurst, “Challenge Problem Implementation Plan: Reactivity Initiated Accident,” CASL-I-2013-0060-000, rev 2, January, 2015

Deterministic Time-Dependent Neutron Transport Benchmark without Spatial Homogenization (C5G7-TD) Version 1.1, Victor F. Boyarinov and Peter A. Fomichenko National Research Centre “Kurchatov Institute” Kurchatov Sq. 1, Moscow, Russia NEA/NSC/DOC(2016) February 2016, OECD Nuclear Energy Agency

A. Toptan, R. Salko, M. Avramova, D. Kropaczek and K. Clarno, "Development and Assessment of CTFFuel," CASL-U-2017-1418-000, 2017.

A. Wysocki, A. Gerlach, B. Kochunas and R. Salko, "Initial Implementation of Transient VERA-CS," CASL-U-2017-1303-000, 2017.

Y. Sung, J. Yan, L. Cao, V. Kucukboyaci and E. Tatli, "Assessment of Multi-Scale Thermal-Hydraulic Codes and Models for DNB Challenge Problem Applications," CASL-U-2014-0032-000, 2014.

[NEA, 2005] “Benchmark on Deterministic Transport Calculations without Spatial Homogenization,” NEA/NSC/DOC(2005)16] ISBN 92-64-01069-6

V.F. Boyarinov, P.A. Fomichenko, J. Hou, K. Ivanov, A. Aures, W. Zwermann, K. Velkov, Deterministic Time-dependent Neutron Transport Benchmark without Spatial Homogenization (C5G7-TD), Version 1.6, NEA/NSC/DOC(2016) OECD Nuclear Energy Agency (2016)